Information-spreading and recurrence in finite-size quantum systems.

PhD Thesis

Sebastian Franz-Josef Schmid

Quantum Optics and Quantum Many-Body Physics
Department of Physics
University of Strathclyde, Glasgow

July 2025

Declaration of Authorship

This thesis is the result of the author's original research. It has been composed by the author and has not been previously submitted for examination which has led to the award of a degree.

Abstract

Finite size closed systems are guaranteed to recur eventually. According to Poincaré's recurrence theorem, recurrence is expected after a time scaling exponentially with the system volume. Low-amplitude recurrences are not covered by the theorem, but can be relevant for modern applications in quantum physics which depend on information to be delocalized in the system. The first part of this work is concerned with the investigation of such low-amplitude recurrences in quantum systems that can be set up in current day AMO systems, such as Rydberg arrays. Modifications to a toy Hamiltonian of hopping bosons are made and their impact on the scaling of the low-amplitude recurrence time with the system volume is investigated. Thereafter, the influence of interactions on this same scaling is analyzed in the system of an XXZ spin-$\frac{1}{2}$ chain. Both avenues show the possibility of generating superlinear scaling, which for low-amplitude recurrences is not inherently given and can be shown to not hold in the most simple setup. The origin of this superlinear scaling cannot be neatly tracked to either the spectral properties of the underlying Hamiltonian, nor to the dimensionality of the Hilbert space traced out by the initial-state evolution. It arises in situations associated with disorder in non-interacting cases, as well as in scrambling dynamics in the presence of interactions. Further investigating the origin of superlinear low-amplitude recurrence is the most promising continuation of this work. The second part of this work is concerned with the efficient delocalization of information in a quantum system. Following up an investigation in Clifford circuits by Kuriyattil et al. [1], this work contrasts the efficiency of dense and sparse long-range coupling models in delocalizing quantum information. Instead of a gate-based approach, this work considers quenches between translationally invariant quadratic fermionic Hamiltonians with dense or exponentially sparse long-range coupling. The tripartite mutual information after a short time evolution is investigated in order to check for the dynamical transition in decay exponents α observed in gate-based models of [1]. The differences to the gate-based models, as well as the models of intermediate sparsity between exponentially sparse and fully dense, which could also be used in gate-based experiments, are shown in this work as potential avenues for future investigation.

Man darf nie an die ganze Straße auf einmal denken, verstehst du? Man muß nur an den nächsten Schritt denken, an den nächsten Atemzug, an den nächsten Besenstrich. Und immer wieder nur an den nächsten.

Michael Ende, Momo

Acknowledgements

As history is written by winners, it is customary to have the acknowledgements of a thesis be a litany of jolly gratitudes towards people that have helped the author to arrive at the time where acknowledgements have a finished work to preceed. I do not consider myself a winner. At the same time, these years have not only provided me with encounters that were able to hold the torch for me when I stumbled, but I have also had the fortune to see myself as, if not a winner, incredibly fortunate and grateful for the people that had my back and shared with me the little joys and sorrows of life. Never have I struggled harder than in the years of my PhD. It has been proclaimed a marathon from the beginning. During the time in Glasgow I have come to understand that the true marathon is life, and now that I am writing these words I finally begin to understand not where to run, but how to do it. Whether this is reason enough to be happy about having done this PhD I do not know. It is a reason to not dwell on the past and to look forward.

I thank Andrew Daley and Peter Kirton, my supervisors, for letting me explore freely and without restrictions whatever I deemed interesting, reining me in whenever my search would lead me too far off the envisioned path. I have learned much about structure, focus and independence from this. I thank all the people from the QOQMS group at the University of Strathclyde for the good interactions and discussions. Notably, I thank Grant Henderson, Johannes Kombe and Callum Duncan. I thank Oded Zilberberg for his constant support and being a voice of reason bridging the gap between academia and the human condition. Similarly I thank Javier del Pino and Antonio Štrkalj for interactions that to them may look small, but that have given me peace in times of need.

I thank the vast arrangement of great people I have met and hope to meet yet again. There is, as always, much to talk, to play, to jest and to ponder. Thank you in particular to Simon Kothe, Ieva Čepaitė, Bruno Gavranovic, Ryan Connor and the crew from Glasgow Limited Magic. I want to thank Sridevi Kuriyattil for being a fantastic friend - I'm happy we shared the adventure in Oxford and have explored an alien world together that we could then disect. In the same vein I thank Tomas Kozlej. Never shy to jump head-on into any thought I may provide or to share his own. Both a source of excitement and calm, whichever the situation required - although the times he misjudged that are among the funniest we've had. My family and friends from back home have provided me with a foundation that I knew I could always rely on and come back to. They are all to thank, but I would like to mention Devesh Nandal, Nicolas Mächler, Denis Zemaj, Kim Stäubli, Sarah Steinegger, Serafin Herger and my siblings Anja, Debora and Benjamin. My special thanks go to my mother and my father. To my mother, Karin Schmid, for she of all people knows the feeling of giving your best, sometimes against all odds. To my father, Daniel Schmid, whose random questioning during my younger years and the debates about darkness research by Professor Doctor Abdul Nachtigaller had a great deal to do with my decision to go into physics.

Last, I thank the two people that more than all the others shaped my world in these years - Ewen Lawrence and Ella Schönborn.
Ewen, that circumstances aligned for us to move in together is one of the things I am most grateful for in these years. I cannot fathom how I would have gone through this PhD without you - without your help, your support, your weird english jokes, your enthusiasm and willingness to share with me a piece of your mind. It is the best of friends who finds within them the strength and compassion to not only stand up for their friends, but also to them.
Ella. Our journey together has shown me that running faster will not solve problems, nor will running to a different location. Instead, over many mistakes, through which you never stopped supporting me with compassion and love, I realised now that the only difference can be made by finding a better reason for running in the first place. Two for joy.

Contents

List of Figures

List of Tables

Dedicated to my grandfather

Habe nun, ach! Philosophie, Juristerei and Medizin, Und leider auch Theologie, durchaus studiert, mit heißem Bemühn. Da steh' ich nun, ich armer Tor, Und bin so klug als wie zuvor!

Johann Wolfgang von Goethe, Faust

1

Introduction

The transfer of information is, together with its storage, one of the core features that distinguish humans among the animal kingdom. Information transfer has undergone massive advances over the course of human civilization. Starting with oral traditions and drawings, going to scripture on tablets, then on letters and further to modern telecommunication methods. Removing the direct feedback from the audience was the advent of broadcasting communication: Perhaps started by tales spoken around a campfire, advancing to proclamations made by heralds and hammered to the doors of churches[1]; becoming even more delocalised by the radio, television and ultimately the internet. Farther reaching and faster communication have made the world much larger, until eventually its finite size has become apparent. From then on, with the neverending improvements in speed of communication, the world has reduced in scope again. Instead of infinite space there is only so far information can go, and eventually it might return. In which ways this information finds its way back to its origin depends, in this human analogy at least, on too many variables to list exhaustively. One might listen to a funny anecdote at a party and realize that it concerns ones own experience fifteen years earlier. One might hear the echo of ones own voice when screaming into a cliffside.

---

[1] That Martin Luther actually put up his 95 theses on church doors in Wittenberg in October 1517 is not historically confirmed.

This work is not aimed at the human element noted in the above analogy. In this work, we investigate the return of information, its recurrence, in finite size quantum systems that can be experimentally implemented in current day atomic, molecular and optical (AMO) laboratories. The finite size of these systems is treated not as a roadblock, but as a feature to understand the timescales on which information can stay away from its origin. This in turn informs on which timescales the system at hand is not showing its boundaries. In terms of the simple examples given above, we adjust the distance of the cliffside to the human and investigate the time it takes for the echo to be noticed.

Recurrence is defined as the restoration of a system to a state it occupied at a previous point in time. Partial recurrence can be defined when a distance measure between states exists and one can therefore speak of the state of a system coming close to a previously occupied state. The strict notion of recurrence was developed and first investigated by Poincaré [2], who drew from ideas by Liouville [3] in Hamiltonian systems. This result had the astonishing implication of reversibility on any scale, something already discussed in statistical physics by Boltzmann, Loschmidt, Nernst, Arrhenius and many others [4–8]. Here lies the apparent paradox one first encounters when learning about entropy. The fact that at some point in time, the pencil dropped to the floor might spontaneously spring back up into the waiting hand. The degrees of freedom necessary to describe such a process fully are so large that such a recurrence is only relevant in the theoretical realm. As such, the intuition we humans get from interacting with a world that typically does not feature such recurrences is not at odds with the tenents of classical physics. In statistical physics, this is formalized by the notion of entropy, differentiating between possible and likely processes. The statistical description by ensembles instead of individual trajectories also directly incorporates contractive dynamics, for which Liouville's theorem is not applicable and recurrence is not guaranteed.

Full recurrence implies the dynamics of the system state to be periodic. The simplest example for this is a motion resolved by a single frequency ω, such as that of a harmonic oscillator. For countably many frequencies participating in the dynamics of the system state this remains true, although with the caveat that for any distance ϵ to a previous state, the system is guaranteed to get closer to that state than ϵ. This is the quasi-ergodic theorem by Poincaré. An example of this quasi-ergodicity coming into play is the motion of a state described by two incommensurate frequencies, $\omega_{1,2}$. As the rational numbers lie dense in the real ones, we can find $q, p \in \mathbb{N}$ such that $|q\omega_1 - p\omega_2|$ is arbitrarily small. The recurrence investigated by Poincaré and later Rice, Kac and others [9–12] focused on the volume in phase space accessible to the initial state of the system, which it traverses via the dynamics governed by the Hamiltonian (or a different dynamical map).

In quantum physics, this volume is replaced by the effective dimension, which is the inverse of the inverse participation ratio [13–16]. Small scale quantum systems of current interest are focused on the distribution of initially local information to many qubits, entangling them in the process and enabling the scaling advantage of quantum systems for computing tasks [17, 18]. For these even partial recurrence can be relevant, as reaccessing the initial qubit in this time might effect the computational task more strongly. Due to the exponential scaling of Hilbert-space dimension with system size in quantum physics, even for small scale quantum systems the effective dimension can be very large, and with so many degrees of freedom numerical treatment can become impossible.

Both open quantum systems theory and eigenstate thermalization theory have been used to reduce the number of degrees of freedom in a similar way as thermodynamic variables for a simpler description of processes exactly described by statistical physics [19–22]. Open quantum systems naturally distinguish the quantum system from its environment, in which e.g. a measurement apparatus can be placed. The underlying assumptions necessary for the construction of open quantum system dynamics disable the investigation of recurrence, which also agrees with the idea of a measured particle to not reenter the quantum system. As such, the investigation of (partial) recurrence can also be framed in a way of determining timescales on which a finite size, exact quantum system can act as an environment for a different quantum system. Eigenstate thermalization poses a similar question, focusing solely on spectral properties of the system [22–25] and successfully developing statistical mechanics of closed quantum systems.

The approach taken in this work is slightly different. We consider systems that can be realized in contemporary atomic, molecular or optical (AMO) experimental systems [26**?** –32], with initial states that possess an initially local quantum of information. On short timescales, this information will propagate from its local original position into the rest of the system. On long timescales, a generic system will either have thermalized or decohered due to experimental imperfections, which can be understood as leakage out of the system. On intermediate timescales, the information will be delocalized in the system but fully confined within it. These are the timescales we investigate, and we specifically are interested in the first time the information relocalizes onto the original position.

Another question we investigate in this thesis regards different variants of long-range coupling. Simple geometries such as square or triangular lattices in varying dimensions have been the initial starting point for discrete space quantum systems. Quantum magnetism in these geometries has provided strong insights into static and dynamic quantities of spin systems and is relevant to this day [33–38]. Dense long-range coupling is, despite its difficulties, a natural setup, as it clearly mimics the unshielded interaction of continuous space systems such as gravity and Coulomb electromagnetism. In an experimental setup, the fast growth of the number of connections in dense long-range systems is problematic, as the time to apply all necessary computational gates competes with the decoherence time of the system. Sparse long-range coupling has recently been investigated in order to understand whether the properties of long-range coupling survive the sparsification [1, 39–41]. We consider these models for larger system sizes in quadratic fermionic models and investigate their properties further.

1.1 Thesis outline

For the sake of compartmentalization, the theory of this thesis is split into two chapters. Chapter 2 considers the theory of recurrence in quantum systems. We first repeat the notion of recurrence in greater detail and connect it to different quantities, most prominently the initial state fidelity. The initial state fidelity directly connects the quantum treatment of recurrence with the classical one [42–46]. In the transition from the single-particle case to interacting many-body quantum systems, we highlight the necessity for more refined measures such as the entanglement entropy and mutual information, both of which are also highly relevant in current day quantum computing considerations [47–49].

Chapter 3 focusses on the theory of correlation-propagation in the context of quadratic models. The exact diagonalization possible in quadratic models enables investigation of very large system sizes, for which sparse coupling patterns might approach a thermodynamic limit as well [39, 40, 50]. We further restrict to quadratic fermionic models and present efficient calculation techniques for quench dynamics in these models.

In chapter 4, we use the theory of chapter 2 to motivate and discuss the results we get in the single-particle regime for recurrences and absences. Moreover, without invoking the spectral tools of eigenstate thermalization research, we consider statistical properties of recurrences and absences in order to judge the typicality of our results. Chapter 5 follows this, but considers the many-body regime. In line with considerations in quantum computing setups, the relocalization and extraction of the information by means of experimental protocols is investigated as well [51, 52].

Chapter 6 uses the theory of chapter 3 and contrasts correlation spreading and tripartite mutual information dynamics in dense and sparse long-range coupling graphs. Several analytical results for static properties of these models are derived, similar to the general result of Vodola et al [53]. System size scaling is performed for all models, showing well-converged behaviour. Additionally, the sparse long-range coupling graphs are investigated further, specifically their properties that are connected to critical deviations in system size, something not done before.

No man ever steps in the same river twice, for it is not the same river and he is not the same man.

Heraclitus

2

Theory of recurrence in quantum systems

In this chapter, we will lay out the theoretical concepts necessary to understand recurrence in quantum systems. We instructively sketch the origin of these considerations from classical physics, dating back to Poincaré, Liouville and Loschmidt. The important takeaway from this is that recurrence is not something unique to quantum systems. The heuristical or statistical approach of many classical theories, concerned with meso- or macroscopic quantities instead of the full phase-space of all involved particles, obfuscates recurrence in the classical regime. With the goal of describing the full wave-function of a system, recurrence is a relevant phenomenon in mesoscopic closed quantum system considerations. The quantum description of recurrence starts in section 2.2, where we describe the typical distance measure to an initial configuration using the fidelity. Motivations for understanding recurrence in fidelity as a measurement witness of our quantum system are presented here. In section 2.3 we broaden this approach to a generic measure, which in turn broadens the recurrence analysis to different scientific fields, typically considered as recurrence quantification analysis (RQA) [54–59]. We show inequivalence between different quantities that are relevant for quantum information purposes, such as trace distance, entanglement entropy and mutual information. The entanglement entropy is further described in section 2.3.4. How to extract the information from a quantum system by means of special protocols without having to wait for actual recurrence is described in section 5.2.

2.1 Recurrence in classical systems

Any physical process in continuous time can be written as a dynamical system, wherein a set of differential equations maps phase space, consisting of all possible configurations of the system state, onto itself. If, given an initial configuration Ξ, there exist restrictions on the dynamical map such that the orbit of Ξ under the dynamical map is bound to a finite region in phase space, the system is guaranteed to approach the initial configuration to any degree of precision. This is Poincaré's Recurrence theorem [2].

In a full system description, where no part of the physical system interacts with an environment whose degrees of freedom are only perturbatively or approximately described, dynamics are time-reversal invariant, or conservative, and by Noether's theorem conserve the system energy [60]. Liouville's Theorem then states that the phase-space volume does not shrink under time evolution and an initial state will recur with arbitrary precision [3].

As this stands in contrast to real-world experience, we can understand that the timescales of large recurrence for sufficiently complex systems are far greater than observation times of humans. This can inversely be taken as the indication that a reduced and potentially dissipative description of the dynamics of a few degrees of freedom can faithfully produce short-time dynamics, where 'short' is defined by the astronomical full recurrence time and therefore encompasses typical experimental or human timescales. However, with recurrence being defined with respect to a distance to the initial configuration, we can consider partial recurrences. Depending on magnitude, these are experimentally accessible, for which reduced dynamical considerations may be ill-suited.

2.2 Fidelity-recurrence in quantum systems

Given a time-independent Hamiltonian $\mathscr{H}$ with a discrete spectrum λ_i, $i \in 0, \cdots, N-1$ and eigenvectors $|\psi_i\rangle$ forming a basis, we can expand any physical state in these eigenvectors

$$|\phi\rangle = \sum_{i=0}^{N-1} c_i |\psi_i\rangle. \tag{2.1}$$

Normalization dictates $\sum_{i=0}^{N-1} |c_i|^2 = 1$. The Hilbert space dimension of the physical setup is given by N, but this does not directly translate to the volume of the orbit traced out by an initial state $|\phi\rangle$ under time-evolution $U(t) = \exp(-i\mathscr{H}t)$, where we set $\hbar = 1$. Instead, the effective dimension D_{eff} of a state is given by

$$D_{\text{eff}}(|\phi\rangle) = \left(\sum_{i=0}^{N-1} |c_i|^4\right)^{-1} . \tag{2.2}$$

This quantity is sometimes denoted as the inverse participation ratio (IPR), especially when the coefficients c_i in (2.2) relate to a position basis instead of the energy eigenbasis [13–16]. The effective dimension tracks the spread of the state $|\phi\rangle$ over the energy eigenstates $|\psi_i\rangle$. It is invariant under time evolution, has the image $D_{\text{eff}} \subset [1, N]$, is minimized by energy eigenstates $|\psi_i\rangle$ and maximized by equal superpositions $|c_i| = \frac{1}{\sqrt{N}}$. The effective dimension allows comparison of different initial states by giving a relation of the dimension of the manifold they trace out under dynamics, instead of invoking the Hilbert-space dimension. Following the classical recurrence theorem, the estimate for the recurrence time of the full system scales as $T_R \propto \mathrm{e}^{D_{\text{eff}}}$. Consider the initial state (2.1), whose time-evolution is given by

$$|\phi(t)\rangle = U(t)|\phi\rangle = \sum_{k=0}^{N-1} c_k \mathrm{e}^{-i\lambda_k t} |\psi_k\rangle. \tag{2.3}$$

In order to set up the prerequisites for recurrence considerations, we require a notion of distance in Hilbert space. The typical measure for this is connected to the fidelity, which for pure states $|\phi_{1,2}\rangle$ is written as

$$F(|\phi_1\rangle, |\phi_2\rangle) = |\langle\phi_1|\phi_2\rangle|^2 . \tag{2.4}$$

The domain of F is the compact interval $[0, 1]$ and $F(|\phi\rangle, |\phi\rangle) = 1$. For pure states, the trace distance Q is directly related to the fidelity,

$$Q(|\phi_1\rangle, |\phi_2\rangle) = \sqrt{1 - F(|\phi_1\rangle, |\phi_2\rangle)}. \tag{2.5}$$

The trace distance serves as a distance in the space of density matrices and has a direct interpretation in terms of the distinguishability between quantum states [44–46]. Fixing one state in (2.4) as our initial state $|\phi\rangle$, the initial state fidelity, also called the *Loschmidt echo* or the *survival probability*, can be expressed

$$\begin{aligned} F(t) =& |\langle\phi|\phi(t)\rangle|^2 = \left|\sum_{k=0}^{N-1} |c_k|^2 \mathrm{e}^{-i\lambda_k t}\right|^2 = \sum_{k,s}^{N-1} |c_k|^2 |c_s|^2 \mathrm{e}^{-i(\lambda_k - \lambda_s)t} \\ =& \sum_k |c_k|^4 + 2\sum_{k<s} |c_k|^2 |c_s|^2 \cos\left((\lambda_s - \lambda_k)\, t\right) . \end{aligned} \tag{2.6}$$

With the finite set of energies λ_k generically being non-commensurate, the initial state fidelity (2.6) is an almost periodic function. More specifically, it is the Fourier-transform of the spectral overlaps c_k [61, 62]. This entails that for any $p > 0$ there exists a time T such that $1 - F(T) < p$.

2.2.1 State Recurrence

The initial state fidelity (trace distance) at time $t = 0$ is at its maximum (minimum). Under any non-trivial time-evolution, there exists a time $t_M > 0$ such that for any two $t_1 < t_2 < t_M$ we have $F(t_1) > F(t_2)$. For a short time, the initial state fidelity will decay monotonically in time, and similarly there will be a monotonic increase in the trace distance to the initial state [42]. Thereafter, the dynamics of the initial state fidelity are encoded in the full state-vector and hard to generalize. Expansions around small p for $F(t) \approx 1 - p$ enable investigation of the functional form of the fidelity around its maximum value 1 [42, 43]. From these expansions it is however not possible to infer the exact times at which the fidelity is close to its maximum. The question at the core of the research presented in this thesis is concerned with these times, more specifically, the first of these times. Take a pure initial state $|\phi\rangle$ subject to unitary time evolution under $U(t) = \exp\left(-i\mathscr{H}t\right)$. For any $p \in [0, 1)$ there exists a time $t_1 > 0$ and a number $\epsilon > 0$ such that $\forall t^* \in [0, t_1)$, $F(t^*) > p$ and $\forall \tilde{t} \in [t_1, t_1 + \epsilon]$, $F\left(\tilde{t}\right) \leq p$. In words, until t_1, the fidelity is bigger than p, and for a finite time ϵ after t_1, it is less than p. It is always possible to find such a t_1, because $F(0) = 1$ and $F(t)$ is continuous. If $F(t)$ never drops below p, then $t_1 = \infty$. The recurrence time T_R^p is then found by the maximization of ϵ,

$$T_R^p = t_1 + \max \epsilon. \tag{2.7}$$

Additionally, we can define the absence time T_A^p,

$$T_A^p = \max \epsilon. \tag{2.8}$$

In other words, the recurrence time (2.7) is determined by the first time the initial state fidelity (2.6) crosses the threshold p from below, whereas the absence time (2.8) is given by the length of time the initial state fidelity is less than p for the first contiguous time. At $t = T_R^p$, we say that the system experiences backflow/recurrence. Fluctuations and non-monotonic behaviour confined to magnitudes smaller than p are not resolved in this framework. The justification for this is heuristical, in the same way as a probabilistic cutoff made in experimental setups. In section 2.2.2, we show how the trace-distance is used as a non-Markovianity measure in an attempt to link open and closed quantum system theories. The core difference between this and our definition of the recurrence is the attention to non-monotonicity in the former. Nonetheless, we can use the interpretability of the trace-distance in terms of a probability to distinguish quantum states

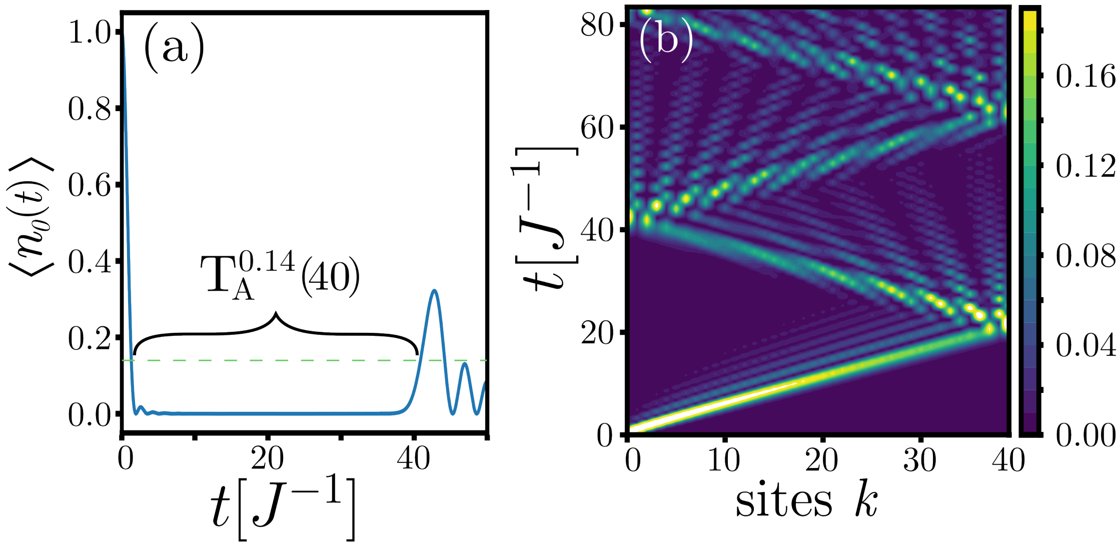

FIGURE 2.1: (a) The absence time $T_A^p(N)$ with reference to the threshold $p = 0.14$ (shown as a dashed horizontal line) indicates how long the excitation is absent from its original position in the probe at site 0, see eq. (2.8). The short time before the excitation departed from the probe at site 0 is t_1, the difference between the absence and the recurrence time. (b) Single-particle dynamics for a non-interacting chain of 40 sites with uniform coupling J and on-site energy $\omega_l = 0$. The system is site 0, the bath are the remaining sites $\{1, \cdots 39\}$. A single particle, initialised on the system-site 0, travels through the bath ballistically and returns to the system site in a time proportional to the bath size. We ask under which circumstances the timescale for the bath to retain information about the system instead grows exponentially with the bath size.

as an argument for why we are interested in the recurrence and absence time as defined in (2.7)& (2.8). With early time evolution monotonically increasing the trace-distance between the state $\rho(t)$ and $\rho(0)$, this is understood as unidirectional information transfer between a system and a bath, in much the same way as we would appreciate it from a measurement apparatus. Non-monotonicity implies information backflow [63] into the system, but as long as the majority of the information still resides outside of the system, the measurement is in some way successful. Thus we justify using a threshold p to cap the maximum backflow into the system, arriving at the recurrence time. In other words, no matter where you go, as long as you stay 200 kilometers away from home, you are considered abroad. The difference between the absence and the recurrence time is illustrated in Fig. ??. For our position localized initial states, the difference is hardly relevant, but the distinction is systematically important. Our interest is based on the question of the timescale on which we can consider $|\phi(t)\rangle$ sufficiently far away from the initial state, where 'sufficiently far away' is conditioned on the function W we choose to investigate. In other words, given at time $t = 0$ our (normalized) function $W \subset [0, 1]$ is maximal, $W(0) = 1$, if t_1 is the smallest time for which $W(t) < p$ is true, and t_2 is the smallest time for which $t_2 > t_1$ and $W(t) > p$, our recurrence time is defined as

$$T_R^p = t_2, \tag{2.9}$$

and our absence time is defined as

$$T_A^p = t_2 - t_1. \tag{2.10}$$

Not all arguments translate directly between the recurrence and the absence time. The former is more readily approachable, but the latter is the actual quantity of interest. We are interested in the scaling of T_A^p as a function of physical system size N, which in turn is connected to the effective dimension (2.2) of the initial state. The system size N may either be an actual volume in continuous space or a number of sites in discrete space. For p sufficiently large, this comes (for the recurrence T_R^p) back to the full recurrence time, which we expect to scale exponentially in D_{eff} due to the recurrence theorem [2, 64]. The initial state fidelity specifically can also be tackled perturbatively in this regime when $1 - p$ is small [42]. On the other hand, for p sufficiently small, local dynamics get sampled and the system size scaling vanishes completely. Is there a direct crossover between local sampling and full orbit sampling or does an intermediate region exist, where all degrees of freedom are sampled but structure beyond the effective dimension can be investigated?

2.2.2 Open quantum systems and reduced states

If the system is coupled to degrees of freedom which are perturbatively described, the situation changes. Given a full system that is partitioned into system S and environment E, the state of the system is obtained by tracing out the degrees of freedom of the environment

$$\rho_S = \operatorname{Tr}_E\left[\rho\right]. \tag{2.11}$$

Here ρ and ρ_S denote density matrices and the latter is called the *reduced density matrix*. Even if the dynamics of the full system+environment $S \bigotimes E$ is generated by a Hamiltonian

$$\mathscr{H} = \mathscr{H}_S \otimes \mathbb{1} + \mathbb{1} \otimes \mathscr{H}_E + \mathscr{H}_I, \tag{2.12}$$

the reduced dynamics on the subspace S are not unitary. The investigation of the reduced dynamics of S sparked the research avenue of open quantum systems [20]. Relevant in this context is the behaviour of the trace distance under a subset of dynamical maps found in open quantum systems, namely completely positive, trace-preserving (CPTP) maps. These maps give rise to Lindblad master-equations for the reduced density matrix ρ_S. Under the action of a CPTP map, the trace distance Q is contractive [65]. This means, that for a CPTP map Φ and two states ρ_1, ρ_2 in S, it is true that

$$Q(\Phi[\rho_1], \Phi[\rho_2]) \leq Q(\rho_1, \rho_2). \tag{2.13}$$

An open quantum system accurately modelled by such a master equation will monotonically decrease distinguishability between different starting states, contracting the orbits towards lower-dimensional submanifolds in Hilbert-space (steady-states for dimension= 0, limit cycles for dimension= 1). This property of the trace distance has been used to investigate closed quantum systems and ask to what extent a Lindblad master equation of these systems is appropriate [63]. Closed system unitary dynamics under $U(t)$ leave the distance between states invariant

$$\langle\phi|U^\dagger(t)U(t)|\psi\rangle = \langle\phi|\psi\rangle. \tag{2.14}$$

The contractivity of the CPTP dynamics towards steady states suggests that the initial state fidelity (2.6) in an open system saturates and never recurs. As such we interpret recurrence of the initial state fidelity as a breaking of the open system, or at least the Markovian open system paradigm.

2.2.3 Probability distributions for absence and recurrence times

Starting with an initial state $|\phi\rangle$ and finding the first absence (recurrence) time, one can go further and ask about any absence (recurrence) that appears until the time-evolution eventually returns the system to its initial state. This path has had many fruitful results in interdisciplinary research, typically under the name of recurrence quantification analysis (RQA) [54–59]. Investigating the average number of roots of a random time-series or random polynomials has been one of the first avenues for this [9, 12], and has recently been extended for quantum systems [64]. Here we outline a way of thinking about it without employing spectral considerations or ergodicity. Whether a system is ergodic or not, the time-evolution of an initial state traces out an orbit in Hilbert space

$$O_{|\phi\rangle} = \{|\phi(t)\rangle | t \in \mathbb{R}_+\}.$$

Consider $|\psi\rangle = |\phi(t_1)\rangle$ to be a state in this orbit. The initial state fidelity with respect to $|\psi\rangle$ can be written as

$$\langle\psi|\psi(t)\rangle = \langle\phi|U(-t_1)U(t+t_1)|\phi\rangle = \langle\phi|U(t)|\phi\rangle = \langle\phi|\phi(t)\rangle, \tag{2.15}$$

and is thus the same for any $|\psi\rangle \in O_{|\phi\rangle}$ – it is an orbit invariant. Sampling all the absence (recurrence) times T_R^p up to a final time T_{max}, we can obtain a probability distribution for all absence (recurrence) times and analyze their qualities. This probability distribution is another orbit invariant, just as is the effective dimension (2.2). All of this circumvents questions on integrability and ergodicity of the underlying Hamiltonian [22–25], although one would expect to see these qualities reflected in the absence (recurrence) time distribution. One thing ergodicity is expected to achieve is answer the question of typicality. Whether an orbit obtained from a small deformation of a different orbit, $O_{|\psi\rangle+\epsilon|\phi\rangle}$, possesses a similar absence time distribution, is not immediately clear, and considering scars found in many-body quantum systems suggests that typicality cannot be easily dismissed.

2.2.3.1 Average recurrence time

From the limiting distribution for absence (recurrence) times we can extract their cumulants as orbit invariants. The mean of these distributions might be thought of as a fitting estimator, but there exists a different formulation of an 'average' recurrence time that can be calculated from a measure theoretic background. If we define the time of the n-th recurrence up to the threshold p (where in these results $p \gg 0$) as t_n^p, the average recurrence time [9, 12, 64, 66] is defined as $T_R(p) = \lim_{n\to\infty} \frac{t_n^p}{n}$. In classical discrete-time systems, it is directly obtained by a result of Smoluchowski [64], requiring only the spectrum $\Omega = \{\omega_i | i \in \{0, \cdots, N-1\}, \omega_i \in \mathbb{R}\}$, and can be extended to continuous-time systems

$$T_R(p) \simeq \frac{\epsilon \exp\left[\log\left(2\pi/\epsilon\right) N\right]}{\sum_{i=1}^{N} \omega_i}.$$

Thus the claim on exponential scaling of the recurrence time in classical systems is established. In quantum systems, a similar derivation results in a doubly exponential scaling for $T_R(p)$ in non-integrable systems and a single exponential scaling in integrable systems with respect to the system volume V [64]

$$T_R(p) \propto \exp\left[e^{\alpha V}\right]. \tag{2.16}$$

As such, the long time limit behaves in the expected manner, and does so independently of microscopic details beyond spectral ones.

2.3 Equilibration and recurrence described via physical properties of the system

At early times, the decay speed of fidelity from an initial state follows a universal quadratic scaling, whose prefactor depends on the details of the Hamiltonian [42, 43, 67–69]. Beyond the universal decay, questions arise on how fast thermalization can be achieved, in contrast to stipulating it as something arising eventually. At very long times, many systems thermalise, and instead of investigating time-resolved qualities of the system, the typical state and fluctuations around it are investigated [22–25]. As the recurrence time is by definition beyond the monotonic early time regime, but aims at finding time-resolved macroscopic deviations away from the typical state, we are unable to use the tools of thermalization and small-time expansions. The simplest heuristic for the effects of intermediate time behaviour arises from physical setups in which we understand the Schrödinger equation as a wave equation. This pertains not only to noninteracting systems, but to any system that is sufficiently well described as a few interacting momentum excitations. As such, investigating e.g. the recurrence time scaling of noninteracting particles on a chain of length N, for example a hopping boson or spin excitation, we will find the ballistic result $T_R^p(N) \propto N$, true for any initial state that describes an initially localized excitation. This forms the basis of our intuition and many of the results presented in chapters 4 & 5 aim at deviating from it in an understandable way.

2.3.1 Single-particle hopping

Here we present a simple single-particle setup for which we can investigate recurrence in different measures. Consider a bosonic particle hopping on a chain of N sites, whose dynamics are generated by the Hamiltonian

$$\mathscr{H} = \sum_{i=0}^{N-1} \omega_i a_i^\dagger a_i + J \sum_{i=0}^{N-2} \left(a_i^\dagger a_{i+1} + \text{h.c.} \right). \tag{2.17}$$

In the single-particle regime, we consider our system to be given by site $i = 0$, which initially hosts a particle, whereas the remaining chain is empty. Here the on-site occupation number $\langle n_0 \rangle = \langle a_0^\dagger a_0 \rangle \in [0, 1]$ is an appropriate distance measure. We have the initial state with $\langle n_0(t = 0) \rangle = 1$, and $\langle n_0(t) \rangle = 0$ means the particle is not on the initial site. For this specific case however it turns out that $\langle n_0(t) \rangle$ and $F(t)$ are equivalent. Our initial state is given as $|\phi\rangle = a_0^\dagger |0\rangle$, where $|0\rangle$ is the state of an empty site defined by $a_0|0\rangle = 0$. With $U(t) = e^{-i\mathscr{H}t}$ we have $|\phi(t)\rangle = U(t)|\phi\rangle$, and the initial state fidelity is then given by

$$F(t) = |\langle 0|a_0 U(t) a_0^\dagger|0\rangle|^2 = \langle 0|a_0 U(t) a_0^\dagger|0\rangle\langle 0|a_0 U^\dagger(t) a_0^\dagger|0\rangle. \tag{2.18}$$

The time-evolution of the on-site occupation in the Schrödinger picture is given by

$$\begin{aligned}\langle n_0\rangle_t &= \langle\phi(t)|n_0|\phi(t)\rangle = \langle 0|a_0 U^\dagger(t) a_0^\dagger a_0 U(t) a_0^\dagger|0\rangle \\ &= \langle 0|a_0 U^\dagger(t) a_0^\dagger|0\rangle\langle 0|a_0 U(t) a_0^\dagger|0\rangle.\end{aligned} \tag{2.19}$$

The second equation expands $|\phi(t)\rangle$. The third equation uses the fact that the initial state has 1 particle and the time-evolution conserves particle-number. Therefore, writing the identity as $\sum_k |k\rangle\langle k|$, only $k = 0$ will generate a non-vanishing overlap and so we can insert the identity as $|0\rangle\langle 0|$. The last expressions in (2.18) and (2.19) are the same. A measure that produces a very different behaviour in terms of recurrence time is the entanglement entropy. The initial state of the single particle setup is the state $|1\rangle|000000\rangle$, where the sites are ordered in any way where the first index describes the initial site. If we consider e.g. a simple chain, the evolution will propel the excitation into the bulk of the chain, away from the initial site. After a short time, the state will be approximately described by $|0\rangle|\psi\rangle$, which again has the initial value of the entanglement entropy, 0. The reason for the entanglement entropy not working in this single-particle case is subject of the next section.

2.3.2 Recurrence of a general quantity

We return to the Hilbert space picture and slightly extend the definition previously formalised for the trace-distance, the initial state fidelity and the on-site occupation, see sections 2.2 and 2.3.1, to any number valued function. Given a number valued function W on the Hilbert-space of quantum states with compact domain that is extremal (maximal or minimal) at time $t = 0$, the absence time T_A^p, (2.7), determines how long the time-evolution keeps this function at values sufficiently far from the initial value. Whether this is a relevant quantity depends on the physical arguments used to choose the function W. One of our requirements is based off the experimental idea that initially, an excitation is localized in position. Thus, we are interested in recurrence within this initial position, and therefore we require our function to be local to the Hilbert space of this subsystem. Next, we want to investigate a quantity that is relevant for quantum setups. The trace-distance satisfies both of these requirements, given the fact that it directly corresponds to the distinguishability between quantum states and the probability of recreating said quantum state, even if only locally. The trace-distance as a metric also has a strong mathematical meaning. On the other hand, we could imagine a function W

that has a different motivation, such as the entanglement entropy of the subsystem with its complement (as the initial state is pure) or the value of a local observable such as the magnetization in a graph of spins. Lastly, we require the extremal value of W that is not taken at $t = 0$ to be meaningful in some way. For the trace-distance, maximal distance implies maximal distinguishability. For the entanglement entropy, maximality implies a highly quantum state of the subsystem that can be used to e.g. teleport information from the subsystem to somewhere else [52]. For the magnetization, this implies finding the spin in an eigenstate of the magnetization axis.

Whether a local observable is a useful quantity to analyse via recurrence has to be decided on a case-by-case basis. A useful guideline for this is found via thermalization. Despite an ill defined limit $t \to \infty$ for finite size closed quantum systems with unitary time-evolution, there has been substantial progress to extend thermalization considerations from open to closed quantum systems, using the effective dimension (2.2) as a crucial tool [22–25]. Closed system thermalization, assuming non-degenerate energy spacings in the spectrum, considers the typical state, i.e. the qualities of a state that the system can be expected to be close to at almost all times $t > 0$. Not only that, but fluctuation-strengths around this typical state (or observables thereof) are accessible as well. Closed system thermalization investigates time nonlocal behaviour around a typical state that depends on system size. In contrast, except when considering statistics, the absence (recurrence) time considers the time-local behaviour at intermediate times, comparing them to the expected behaviour of a bath of infinite size. With the definition of recurrence using the function W, our focus lies on deviations from the non-initial extremal value. Maximum distinguishability for the trace-distance, minimal particle occupation for the on-site occupation number, maximal von Neumann entropy for the entanglement. This difference is mostly relevant for finite system sizes. For the on-site occupation number, the typical value is the equipartition $\frac{1}{N}$. For the von Neumann entropy, given e.g. an XXZ chain of spin-$\frac{1}{2}$ particles, the typical value is the Page limit [70]. These all approach the extremal value for $N \to \infty$. In order to understand how well the thermodynamic limit can be mimicked by a finite size bath, the comparison is always made against the infinite bath-size value.

From the above we can also deduce why the entanglement entropy is a bad measure in the single-particle case of section 2.3.1. The Page limit for the entanglement entropy in the single particle case decays to zero for increasing system size. As such, the typical value of the entanglement entropy as our number valued function W is close to the extremal value of the initial state, instead of being close to the other extremal value. Similarly, the on-site occupation number would not be useful if every site of the chain described in (2.17) starts with one boson. This is explored in the next section.

2.3.3 Many-Body setups

The step from 1 to 2 particles on the chain described in section 2.3.1 via (2.17) indicates the inequivalence of the different measures. Partial recurrence in $\langle n_0 \rangle$ is very different from partial recurrence in trace-distance. With two particles on the chain, both starting at site 0, we have $\langle n_0 \rangle \in [0, 2]$. If in the course of dynamics the reduced density matrix on site 0, $\rho_0(t) = \mathrm{Tr}_{1,\cdots N-1}[\rho]$, corresponds to 1 particle, $\rho_0(t) = |1\rangle\langle 1|$, we get a 50% recurrence in $\langle n_0 \rangle$, whereas the trace-distance is maximal. This inequivalence is nicely indicated with two additional measures we could employ. One is the purity of the reduced density matrix ρ_0. Similar to the trace-distance, the purity is contractive for CPTP maps that are unital (the infinite temperature density matrix is a fixed point) [71, 72]. The other is the entanglement entropy between system and environment. The entanglement we investigate via the von Neumann entropy

$$S_{vN} = -\mathrm{Tr}_S \left[\rho_S \log\left(\rho_S\right)\right], \tag{2.20}$$

and the purity we write as

$$F_P = \mathrm{Tr}_S \left[\rho_S^2\right]. \tag{2.21}$$

Fidelity (2.6) and purity (2.21) resolve the proximity to an initial state to a different degree. Starting with an arbitrary pure state $|\phi\rangle$ and a pure product state $|\psi\rangle = |\psi_S\rangle|\psi_E\rangle$, the following inequality can be derived [43]

$$|\langle\psi|\phi\rangle|^4 \leq \mathrm{Tr}_S \left[\sigma_S \rho_S\right]^2 \leq \mathrm{Tr}_S \left[\rho_S^2\right] = F_P, \tag{2.22}$$

where $\rho_S = \mathrm{Tr}_E \left[|\phi\rangle\langle\phi|\right]$ and $\sigma_S = |\psi_S\rangle\langle\psi_S|$. For the purpose of our investigation, we can take $|\phi\rangle = U(t)|\psi\rangle$ and the parts in (2.22) can be reformulated in quantities of interest, the initial state fidelity and the purity,

$$F(t)^2 \leq \mathrm{Tr}_S \left[\sigma_S \rho_S(t)\right]^2 \leq F_P(t). \tag{2.23}$$

From (2.23) we see that the initial state fidelity is a more sensitive measure than the purity. For a state to have high fidelity, it is required to have high purity, but not vice-versa. As the purity is a measure of mixedness of a state, and in case of said state being a reduced state from a global pure state, also a measure of entanglement, we get a non-equivalence between fidelity and entanglement.

2.3.4 Entanglement

Entanglement is a quality that is exclusively associated with quantum systems. The possibility of entanglement is at the heart of the exponential scaling of Hilbert-space dimension R^N from local Hilbert-space dimension R, as opposed to classical phase-space scaling, which is linear, with the dimension being $6N$. Many measures for entanglement exist, all of them (for finite Hilbert space dimension) compact with extremal values agreeing to denote no entanglement ($= 0$) and maximal entanglement ($= max$). We repeat the definition of the von Neumann entropy, which itself is either seen as a quantum mechanical analogue to the Shannon entropy or a special case of the Rényi-entropy with parameter $q = 1$. For a density matrix ρ, it is given as

$$S_{vN} = \mathrm{Tr}\left[\rho\,\mathrm{log}\rho\right]. \tag{2.24}$$

Imagine a system described by a Hilbert-space H_S. By virtue of a cut, that by no means is required to be happening in real space, we partition this system into two, H_A and H_B, that make up the full space via a Kronecker product, $H_S = H_A \otimes H_B$. Consider a pure state $|\psi\rangle$ in H_S. Decomposing it into orthonormal basis-elements $|i\rangle$ on H_S, it is written as

$$|\psi\rangle = \sum_{i=0}^{N} c_i |i\rangle. \tag{2.25}$$

By means of a Schmidt decomposition we can follow the cut through H_S also in this formulation, arriving at

$$|\psi\rangle = \sum_{i=0}^{M-1} q_i |u_i\rangle_A |v_i\rangle_B, \tag{2.26}$$

where $|u_i\rangle_A$ and $|v_i\rangle_B$ denote the orthonormal basis elements of H_A and H_B, respectively. The reduced state on H_A is given by a partial trace of $\rho = |\psi\rangle\langle\psi|$,

$$\rho_A = \mathrm{Tr}_B\left[\rho\right] = \sum_{i=0}^{M-1} |q_i|^2 |u_i\rangle_A \langle u_i|_A, \tag{2.27}$$

and analogously for B. As the full state $|\psi\rangle$ is pure, its density matrix has rank 1 and its von Neumann entropy is $= 0$. This quality does not extend to the reduced density matrix ρ_A in (2.27). Its von Neumann entropy is given as

$$S_{vN}\left[\rho_A\right] = -\sum_{i=0}^{M-1} |q_i|^2 \mathrm{log}\left(|q_i|^2\right) = S_{vN}\left[\rho_B\right]. \tag{2.28}$$

The symmetry $S_{vN}\left[\rho_A\right] = S_{vN}\left[\rho_B\right]$ shows that entanglement is a property of a cut as much as of the states generated by said cut. ρ_A represents a pure state iff $q_i = \delta_{i,j}$ for one $j \in \{1, \cdots, M-1\}$.

2.3.5 Mutual Information

The von Neumann entropy is the unique quantum entropy for which the chain rule for conditional entropy holds. This consequentially enables the formulation of different information theoretic measures such as conditional information and mutual information. The mutual information in turn is given as

$$I(A,B) = S_{vN}\left(\rho_A\right) + S_{vN}\left(\rho_B\right) - S_{vN}\left(\rho\right). \tag{2.29}$$

Similar to entanglement, mutual information can also serve as a witness for quantum effects. It quantifies the amount of information one can get on A by investigating B. Using subadditivity of the entanglement entropy and the triangle inequality, one can show [73]

$$0 \leq I(A,B) \leq 2\mathrm{min}\left(S_{vN}(A),\, S_{vN}(B)\right), \tag{2.30}$$

which reduces to

$$I(A,B) = 2S_{vN}(A) \tag{2.31}$$

if the state ρ_{AB} is pure. If the mutual information tracks the amount of information about A that is contained in B, We can use maximally entangled pairs to monitor the recurrence of a specific piece of information back into the local region A even in a many-body regime.

2.3.6 Equivalence of mixedness measures

The special situation of the single-particle regime in section 2.3.1 can be formalized further, relating the purity and the von Neumann entropy.[1] Now given a 2×2 density matrix ρ, i.e. a positive semi-definite hermitian matrix with unit trace, we can diagonalize it by a unitary transformation and reveal that it is a one-parameter group

$$\rho = \begin{pmatrix} p & 0 \\ 0 & 1-p \end{pmatrix}. \tag{2.32}$$

---

[1] The von Neumann entropy itself is a special case of the Rényi entropy, denoting the unique entropy for which the chain rule for conditional entropy holds. This consequentially enables the formulation of different information theoretic measures such as the mutual information.

From this we get the purity and the von Neumann entropy as

$$\begin{aligned} F_P(\rho) &= \mathrm{Tr}\left[\rho^2\right] = 2p^2 - 2p + 1, \\ S_{vN}(\rho) &= -\mathrm{Tr}\left[\rho \log\left(\rho\right)\right] = p \log\left(p\right) + \left(1-p\right)\log\left(1-p\right). \end{aligned} \tag{2.33}$$

We can invert the relation for the purity and get an equation for the parameter p

$$p = \frac{1 \pm \sqrt{2F_P(\rho) - 1}}{2}, \tag{2.34}$$

which can be used in the formula for the von Neumann entropy to get a unique value. Therefore, for 2 × 2 density matrices, purity and von Neumann entropy are equivalent. This procedure fails when considering larger density matrices, and one can formulate a geometrical argument for this on the space of density matrices[45]. For a given purity, the subset of density matrices with said purity is not a subset for constant von Neumann entropy. At their extremal values the measures (and all other mixedness measures) coincide, but in between there is no mapping for this, except in the special case shown above, which also applies in the single-particle case presented in section 2.3.1. Going forward, we will employ the von Neumann entropy as our measure for mixedness/entanglement. The inequality (2.23) cannot be explicitly invoked, but the usefulness of formulating mutual information measures will be relevant for the extended study of our systems [43].

2.4 Summary

In this chapter, the necessary ingredients for understanding recurrence results are laid out. From the classical origin of recurrence we have introduced the quantum analogue using the initial state fidelity and the trace-distance. With motivation from current day quantum computing ideas, we have introduced physical motivations for different, more restrictive measures of recurrence that are based on physical motivations instead of strict mathematical analogy to the classical phase-space picture. For the interested reader that may try to expand this line of thinking, the section 2.3 is the most important one, as it presents the necessary conditions we identified for a quantity whose recurrence might be insightful. The theory of this chapter is used to get the results shown in two chapters. In chapter 4, we consider single-particle bosonic setups and its recurrences and absences. In chapter 5, results for a many-body model of a spin-$\frac{1}{2}$ chain subject to an XXZ Hamiltonian are shown. In addition to recurrence results, this chapter also highlights different methods of extracting the delocalized information from the system in the intermediate time by means of different experimental protocols.

Was einmal gedacht wurde, kann nicht mehr zurückgenommen werden.

Friedrich Dürrenmatt, Die Physiker

3

Theoretical methods

In this chapter we lay out the theory of quadratic models featuring long-range couplings, both sparse and dense. Long-range coupling is specifically difficult to handle for numerical methods such as tensor-network techniques, limiting scaling with system size. However, approaching the thermodynamic limit in long-range coupling models typically necessitates a bigger system. As a consequence, analyzing long-range coupling systems requires easing the numerical intensity of the model at hand. Part of the work in this thesis is directly motivated by a gate-based approach to long-range coupling of qubits using the Clifford group [1]. In this case, the Clifford group as a subgroup of the group of all quantum gates is the numerical simplification. In the case of this thesis, it is focusing on quadratic models whose diagonalization via a Bogoliubov-Valatin transformation is possible. This work aims at investigating whether the result of the gate-based approach, which showed a dynamical transition in the tripartite mutual information as a function of the coupling exponent, i.e. the decay strength of the long-range coupling over distance, persists in the continuous-time Hamiltonian model. In sections 3.2 and 3.3, we describe the dynamical quantities of interest in the comparison between coupling-styles. Section 3.4 focuses on the diagonalization techniques of our models, with section 3.5 specifying us further to fermionic gaussian states. The diagonalization and the restriction to a subspace of the whole Hilbert-space are the simplifications enabled through investigation of the quadratic models. In section 3.6 we introduce the different styles of long-range coupling and derive relations for the dispersion relation and the group-velocity and the density of states.

3.1 Background

Many striking and elegant mathematical results in physical systems rely on particular symmetries reducing the complexity of the system under investigation. Shared symmetries between systems give rise to universality in their properties close to criticality and enable the classification of similar behaviour in very different systems, such as magnets, superconductors, biological systems and cold-atom ensembles [50, 74, 75]. Tabularising the critical exponents of the scaling of the order parameters such as magnetization in magnets or flux tubes in superconductors enables comparison between these physical systems based only on these exponents. In quantum physics, research has for several decades focussed on systems with local, short-range interactions, either based on lattice geometries with nearest-neighbour interactions or field theories with ϕ^4 interactions. The reason for this is based on simplicity, as in parallel also conformal field theories in quantum field theory were intensively studied. Starting from Ising's investigation in 1D [33] and Onsager's extension to 2D [34], the investigations of these short-range systems has advanced in many directions. One of which being tensor-network based methods that continue to push numerical and even conceptual boundaries in physics, mathematics and computer science [76, 77].

Classical systems have historically considered non-local theories most notably newtonian gravity and electromagnetism with Coulomb interactions [78], and in recent years, advances have been made on long-range quantum systems [40, 79–83], and a review of the current state of the art is written by Defenu et al. [50]

With tunability and control of quantum systems increasing steadily, one of the basic qualities of the physical models investigated can be relaxed: Density of couplings. The gravitational force cannot be shielded, and except for very special cases in condensed matter physics the coupling between different points in space is monotonously decaying with distance. With high-fidelity control of quantum systems, Hamiltonian systems can have an underlying structure more intricate than a typical lattice [84, 85]. Additionally, the gate-based investigations dominant in quantum information theory research can forego the need for a lattice theory and instantiate any coupling graph. Sparse long-range coupling is substantially cheaper in computational resources, and current research is investigating whether these sparse models show substantially different features than either their dense counterparts or the short-range models [1, 39, 40, 86].

3.2 Lieb-Robinson bounds

In classical systems, the upper limit of information propagation is dictated by relativistic speed limits and Lorentz covariance. Physical effects are confined in a causal region, which is dubbed a “light-cone”. In quantum theories, even those disregarding special relativity, a similar concept is found, arising from the underlying dynamics of the Schrödinger equation without explicit insertion of a physical mechanism to uphold subliminal information travel. In quantum physics, the light-cone traces indicates a speed of information propagation called the Lieb-Robinson velocity. Given two operators A_i and B_j on different sites i, j of a lattice system, the correlations building up between the operators relate to the speed at which the dynamics manage to delocalize the operators, such that their supports start overlapping considerably. The simplest model for this takes the shape

$$||[A_i(t=0), B_j(t=T)]|| \leq C\, e^{-\mu\cdot(d(i,j)-vT)}. \tag{3.1}$$

Here, $C, \mu > 0$ are constants, v is the Lieb-Robinson propagation velocity and $d(\cdot,\cdot)$ is a distance function. From the exponent we see the exponential damping of correlations if the distance $d(i,j)$ cannot be bridged in time T with velocity v. The above equation is best fitting for locally interacting systems (with respect to the distance function $d(i,j)$) and imply a constant Lieb-Robinson velocity through time until the operators are spread among the whole available space. Dense and sparse long-range interacting models have different functional forms for the Lieb-Robinson velocity that can speed up for later times [87]. A simple example for non-constant propagation velocity is diffusion-like spread of correlations. A toy model for this is the heat-equation, whose fundamental solution is

$$f(x,t) = \frac{1}{\sqrt{4\pi a t}} \exp\left(-x^2/4at\right). \tag{3.2}$$

Here, $x \in \mathbb{R}$ denotes spatial position, $t > 0$ denotes time and $a > 0$ is a constant that denotes the initial width of the gaussian $f(x,0)$. If we consider a threshold $0 < p < 1$, we can perform the investigation as described above, asking when the functional value $f(x,t)$ exceeds p. This we can rewrite for position and get the velocity, resulting in

$$v(p,t) = \frac{\partial}{\partial t} x(p,t) = \frac{1}{2\sqrt{a}} \sqrt{-\log(p)} \frac{1}{2\sqrt{t}}. \tag{3.3}$$

In this case we see a non-constant propagation velocity, which in fact decreases for larger and larger times, which aligns with the general picture on diffusion.

For long-range coupling, propagation velocities can also dramatically depend on the initial state under investigation, ranging from linear propagation as in the local regime up to power-law regimes [88]. Lieb-Robinson light-cones, whether linear or not, confine any measure of information transfer, including the build-up of entanglement over long distances. A certain notion of entanglement, the tripartite mutual information (TMI) we will use to codify whether correlations are transported to different regions in our setups.

3.3 Tripartite Mutual Information

Here we expand on the notion of entanglement that was developed in chapter 2, section 2.3.4. Build-up of entanglement across a distance is confined by Lieb-Robinson bounds. As mentioned in section 2.3.4, the von Neumann entropy can also be used to develop more complex notions such as the mutual information $I(A, B)$, shown in eq. (2.29). The mutual information codifies how much information about a subregion A is obtained by measuring region B. Partitioning the system S into more than two subregions allows the extension of the mutual information. Split into four, A, B, C, D, the tripartite mutual information (TMI) I_3 is given by

$$\begin{aligned} I_3 &= I(A:B:C) = I(A,B) + I(A,C) - I(A,BC) \\ &= S_A + S_B + S_C - S_{AB} - S_{AC} - S_{BC} + S_{ABC} \end{aligned} \tag{3.4}$$

From understanding the mutual information, we can use the first line of (3.4) to understand its purpose. When $I_3 < 0$, the information acquired on A when investigating BC is larger than the combined information on A obtained by investigating B and C independently. This requires there to be excitations within the different subregions to generate entanglement between them, as this is the origin of non-separability of the quantum state. As such, generating non-trivial TMI requires at least three excitations that are dispersed within the subregions [89, 90]. Were this not the case and thus one of the subregions (for example A) were empty, no information about other subregions could be located in A. In quadratic models, Wick's theorem always allows breaking down higher order correlations into two-point functions, and as such one can always find a basis in which these correlations will be restricted to two particles, making the TMI trivial vanishing. Nonetheless, certain partitions of our degrees of freedom are special insofar as they correspond to partitions that are naturally singled out by measurement-devices, such as a laser that probes the internal state of a spin and is hence position local. We will orient ourselves around those partitions and investigate the TMI therein.

3.4 Quadratic models

Given a Hamiltonian of the form

$$\mathscr{H} = \sum_{i,j} a_{i,j} c_i^\dagger c_j + \left(b_{i,j} c_i c_j + \overline{b_{i,j}} c_i^\dagger c_j^\dagger \right), \tag{3.5}$$

where c_i ($c_i^\dagger$) are annihilation (creation) operators that either obey fermionic or bosonic statistics and. We write the commutator in q-deformation, which combines both canonical commutation (CCR) and canonical anti-commutation relations (CAR),

$$[o_1, o_2]_q = o_1 o_2 + (-1)^q \, o_2 o_1. \tag{3.6}$$

We express the fermionic ($q = 0$) and bosonic ($q = 1$) relations as

$$\begin{aligned} \left[c_i^\dagger, c_j \right]_q &= \delta_{i,j} \\ [c_i, c_j]_q &= 0. \end{aligned} \tag{3.7}$$

The numbers $a_{i,j}$ and $b_{i,j}$ can be arranged into the matrices $A = (a_{i,j})_{i,j\in\{0,\cdots,N-1\}}$, $B = (B_{i,j})_{i,j\in\{0,\cdots,N-1\}}$. In order for the Hamiltonian to be hermitian, the matrix A is hermitian, while B is anti-hermitian for fermions and hermitian for bosons. We rewrite the Hamiltonian as

$$\mathscr{H} = v^\dagger A v + v^T B v + v^\dagger \overline{B} \left(v^\dagger \right)^T, \tag{3.8}$$

where $v^T = (c_0, c_1, \cdots, c_{N-1})$ is the vector of operators[1]. Doubling the operator space and writing the vector $w^T = \left(c_0, \cdots, c_{N-1}, c_0^\dagger, \cdots, c_{N-1}^\dagger \right)$[2], any quadratic Hamiltonian can be written as a quadratic form

$$\mathscr{H} = \frac{1}{2} w^\dagger D w + O. \tag{3.9}$$

Here, $O \propto \mathbb{1}$ is an offset due to the (anti)commutation relations (3.7), whichever appropriate, but is typically irrelevant, as it merely corresponds to a global energy shift. The dynamical matrix D can be deduced from (3.8) as

$$D = \begin{pmatrix} \mathbb{1} & 0 \\ 0 & (-1)^q \, \mathbb{1} \end{pmatrix} \begin{pmatrix} A & \overline{B} \\ B & A \end{pmatrix} = \mathbb{I}_q \begin{pmatrix} A & \overline{B} \\ B & A \end{pmatrix}, \tag{3.10}$$

where $\mathbb{I}_q$ upholds the structure of the operators. Diagonalizing the Hamiltonian corresponds to diagonalizing the dynamical matrix in such a way that the commutation

---

[1] The dagger operator on a vector applies the transpose to the vector and the dagger on the individual elements

[2] also known as Nambu space

relations of the operators (3.7) are respected. The diagonalization procedure aims at obtaining the basis of non-interacting normal modes. The transformation used for this diagonalization should preserve the structure from (3.7). This amounts to understanding the normal modes in a system of fermions (bosons) to still behave like fermions (bosons). This transformation is known as the Bogoliubov-Valatin transformation. In the q-deformation language, the structure to be preserved is given by $\mathbb{I}_q$, which is the identity for Fermions and symplectic for Bosons. That is to say that the transformation matrix $\mathbb{T}$ connecting the Nambu vector w^T of original modes and the Nambu vector $\zeta^T = \left(a_0, \cdots, a_{N-1}, a_0^\dagger, \cdots, a_{N-1}^\dagger\right)$ of normal modes is required to obey

$$\mathbb{T}^{-1}\mathbb{I}_q\mathbb{T} = \mathbb{I}_q. \tag{3.11}$$

This guarantees that the normal modes in ζ obey the same structure (3.7) as the original modes in w. This is achieved by not diagonalizing D, but instead $\mathbb{I}_q D$. The result is then given by

$$\mathscr{H} = \frac{1}{2}\zeta^\dagger E\zeta = \frac{1}{2}\sum_i \epsilon_i a_i^\dagger a_i, \tag{3.12}$$

where ϵ_i are the elements of the diagonal matrix E and denote the eigenenergies of the normal modes a_i, which obey the same statistics as the c_i.

3.4.1 Translationally invariant fermionic systems with quadratic hamiltonians

Quadratic fermionic models with long-range interactions have been investigated in many different contexts, the most famous being the celebrated Sachdev-Ye-Kitaev (SYK) model [91–93]. They also often arise in the context of spin-models subject to a Jordan-Wigner transformation [94]. After a successful mapping between spins and (quadratic) fermions has been established (or when starting off from a quadratic fermionic model), the routines of this section can be employed, although some care has to be taken. First, the Jordan-Wigner transformation is typically multi-valued, giving rise to several fermionic Hamiltonians whose relevance to the underlying spin-model has to be carefully understood [94–96]. In this work we treat fermions on their own footing and complications arising of understanding the connection to spin-models are disregarded. This line of questioning started with Sachdev, Ye, Kitaev and Vidal and has received much attention in different contexts [41, 79, 81, 91–93]. Translational invariance enables splitting the Bogoliubov-Valatin transformation outlined above into two parts. The starting Hamiltonian is written as

$$\begin{aligned}\mathscr{H} &= \sum_{s,r}^{N} J_{|s-r|} c_s^\dagger c_r + \Delta_{|s-r|} c_s c_r + \overline{\Delta}_{|s-r|} c_s^\dagger c_r^\dagger \\ &= \frac{1}{2} w^\dagger \begin{pmatrix} J & \overline{\Delta} \\ \Delta & -J \end{pmatrix} w + O,\end{aligned} \tag{3.13}$$

identifying $J = A$ and $\Delta = B$ from earlier and using periodic boundary conditions. Translational invariance and fermionic statistics imply that J is a hermitian circulant matrix, and Δ is anti-hermitian circulant. Circulant matrices, irrespective of their entries, are diagonalized by discrete Fourier-transformation matrices,

$$F_N = (f_{s,r})_{s,r\in\{0,\cdots,N-1\}}\,, \text{ with } f_{s,r} = e^{-\frac{2\pi i}{N} s\cdot r}, \tag{3.14}$$

and so the blocks of the block matrix in (3.13) are independently diagonalized via

$$\begin{pmatrix} F_N & 0 \\ 0 & F_N \end{pmatrix} \begin{pmatrix} J & \overline{\Delta} \\ \Delta & -J \end{pmatrix} \begin{pmatrix} F_N^{-1} & 0 \\ 0 & F_N^{-1} \end{pmatrix} = \begin{pmatrix} D_J & \overline{D_\Delta} \\ D_\Delta & -D_J \end{pmatrix}. \tag{3.15}$$

Permutation of the basis via a permutation matrix P reveals that this matrix is now blockdiagonal with blocks of size 2 (given that N was even). Such a block we write as

$$B_k = \begin{pmatrix} \mathscr{J}_k & \overline{\mathscr{D}_k} \\ \mathscr{D}_k & \mathscr{J}_k \end{pmatrix}. \tag{3.16}$$

Both the Fourier-transformation and the permutation conserve the structure $\mathbb{I}_{q=0} = \mathbb{1}$, and the second part of the Bogoliubov-Valatin transformation is reduced to independently diagonalizing the 2 × 2 blocks.[3] The transformation achieving this is (in the fermionic case) given by

$$U_k = \begin{pmatrix} u_k & v_k \\ -\overline{v_k} & \overline{u_k} \end{pmatrix}, \tag{3.17}$$

and due to the fermionic structure $\mathbb{I}_{q=0}$ the entries can be parametrized as $u = \cos(\theta_k/2)$ and $v = i\sin(\theta_k/2)$. The angle θ_k is obtained from the relation

$$e^{i\theta_k} = \cos(\theta_k) + i\,\sin(\theta_k) = \frac{\mathscr{J}_k + \overline{\mathscr{D}_k}}{\sqrt{|\mathscr{J}_k|^2 + |\mathscr{D}_k|^2}}, \tag{3.18}$$

and the eigenenergies of the particle-like excitations are given as

$$\epsilon_k = \sqrt{|\mathscr{J}_k|^2 + |\mathscr{D}_k|^2}. \tag{3.19}$$

---

[3] This independence between the 2×2 blocks is the big gain obtained by investigating a translationally invariant model and by splitting the Bogoliubov transformation into two instructive parts.

The spectrum of the diagonalized matrix includes also the hole-like excitations with energies $-\epsilon_k$, and filling all those excitations provides the ground-state of the model.

3.4.2 Normal modes

In section 3.4.1 we investigated the translationally invariant fermionic Hamiltonian (3.13) and split the Bogoliubov-Valatin transformation Q that diagonalized the dynamical matrix into three parts. The Fourier-transformation F_N, the permutation P and the unitary transformation U made up of 2×2 blocks U_k on the diagonal,

$$Q = UP \begin{pmatrix} F_N & 0 \\ 0 & F_N \end{pmatrix}. \tag{3.20}$$

Thus we said we can rewrite the Hamiltonian (3.13) in the following way (dropping the constant offset O)

$$\begin{aligned} \mathscr{H} &= \frac{1}{2} w^\dagger Q^{-1} Q \begin{pmatrix} J & \overline{\Delta} \\ \Delta & -J \end{pmatrix} Q^{-1} Q w \\ &= \frac{1}{2} \left[w^\dagger Q^{-1} \right] \left[Q \begin{pmatrix} J & \overline{\Delta} \\ \Delta & -J \end{pmatrix} Q^{-1} \right] [Qw]. \\ &= \frac{1}{2} \left[w^\dagger Q^{-1} \right] \begin{pmatrix} E & 0 \\ 0 & -E \end{pmatrix} [Qw] \end{aligned} \tag{3.21}$$

It is potentially easier to understand section 3.4.1 from the perspective of transforming the fermionic modes c_s into their normal modes via Qw. The first step, the Fourier-transformation, can be written as

$$c_k = \frac{1}{N} \sum_{s=0}^{N-1} e^{-\frac{2\pi i}{N} k \cdot s} c_s. \tag{3.22}$$

The block-diagonal form of the Hamiltonian (3.13) after performing only the Fourier-transformation and the Permutation thereafter is

$$\mathscr{H} = \frac{1}{2} \sum_k \begin{pmatrix} c_k^\dagger & c_{N-k} \end{pmatrix} \begin{pmatrix} \mathscr{J}_k & \overline{\mathscr{D}_k} \\ \mathscr{D}_k & -\mathscr{J}_k \end{pmatrix} \begin{pmatrix} c_k \\ c_{N-k}^\dagger \end{pmatrix} . \tag{3.23}$$

The unitary transformation as the last step is

$$\begin{pmatrix} \alpha_k \\ \alpha_{N-k}^\dagger \end{pmatrix} = \begin{pmatrix} u_k & v_k \\ -\overline{v_k} & \overline{u_k} \end{pmatrix} \begin{pmatrix} c_k \\ c_{N-k}^\dagger \end{pmatrix}, \tag{3.24}$$

which is how the single-mode Bogoliubov-Valatin transformation is typically displayed.

3.5 Fermionic Gaussian states

As mentioned at the beginning of this chapter, the motivation for investigating quadratic models lies in the fact that they enable efficient and even analytical diagonalization. In order to further simplify the situation and give us a bigger numerical edge, we focus on fermionic gaussian states (FGS). These include all the eigenstates of a quadratic fermionic system and the space of FGS is closed under evolution by any quadratic Hamiltonian. This further means that quenches between different quadratic models will always remain in the space of FGS. As such, this restriction is similar to the restriction to the Clifford group in gate-based state-evolution. The description of fermionic gaussian states given here follows the exhaustive and comprehensive review given by Surace and Tagliacozzo [97]. A fermionic state that is fully described by its two-point correlations, $\langle c_r^\dagger c_s\rangle$, $\langle c_r c_s\rangle$ is called a fermionic gaussian state (FGS). Its density matrix can be written as

$$\rho = \frac{e^{-H}}{\mathscr{Z}}. \tag{3.25}$$

Here, H is not the generator of time-translations, but is called the parent Hamiltonian or the entanglement Hamiltonian [98–100]. The equivalent information in the density matrix is found in the correlation matrix Γ

$$\Gamma = \begin{pmatrix} \Gamma^{c^\dagger c} & \Gamma^{cc} \\ \Gamma^{c^\dagger c^\dagger} & \Gamma^{cc^\dagger} \end{pmatrix}. \tag{3.26}$$

Here, $\left(\Gamma^{c^\dagger c}\right)_{i,j} = \langle c_i^\dagger c_j\rangle$, etc. and from the CAR we get $\Gamma^{cc^\dagger} = \mathbb{1} - \Gamma^{c^\dagger c}$ and $\Gamma^{cc} = -\overline{\Gamma^{c^\dagger c^\dagger}}$. This is equivalent to saying there is a one-to-one correspondence between the parent Hamiltonian and the correlation matrix

$$\Gamma = \frac{1}{1+e^{2H}}. \tag{3.27}$$

Bogoliubov diagonalization of the parent Hamiltonian via a matrix Q will also diagonalize the correlation matrix Γ. If the FGS is the ground-state of the physical Hamiltonian, this diagonal picture will give the correlation matrix (in the diagonal basis) as

$$\Gamma_{GS} = \begin{pmatrix} 0 & 0 \\ 0 & \mathbb{1}_N \end{pmatrix}. \tag{3.28}$$

The ground state correlation matrix has only eigenvalues 0 or 1, with eigenvalues $= 1$ corresponding to hole-like excitations (see (3.19) and below). This means that the Fermi-sea is filled, i.e. all the fermionic excitations that lower the energy of the state are occupied, while none of the other ones are. Every ground state of a quadratic fermionic Hamiltonian has this structure and is a FGS.

3.5.1 Dynamics

The space of fermionic gaussian states is closed under the action of unitary operators arising from quadratic fermionic Hamiltonians. Additionally, every eigenstate of a quadratic fermionic Hamiltonian is an FGS [98, 99]. In this thesis we are interested in dynamics arising from quenches between different quadratic fermionic Hamiltonians, starting in a ground state. The full dynamics are thus captured in the correlation matrix Γ. The ground state $|0\rangle$ is determined in particle-like normal modes $a_{k^0}^\dagger$ (which all have positive eigenenergies) by $\alpha_{k^0}|0\rangle = 0$ for all momenta k^0. The pre- and post-quench Hamiltonians are fully defined by the Bogoliubov-angles θ_k^0 and θ_k, respectively. For ease of reading we define $\cos_k = \cos(\theta_k/2)$ and $\sin_k = \sin(\theta_k/2)$. The time-evolution on normal modes introduces nothing but a phase. Thereafter inverse-transforming them into the Fourier-modes yields

$$\begin{pmatrix} c_k(t) \\ c_{M-k}^\dagger(t) \end{pmatrix} = \begin{pmatrix} \cos_k & -i\sin_k \\ -i\sin_k & \cos_k \end{pmatrix} \begin{pmatrix} e^{-i\,\epsilon_k} & 0 \\ 0 & e^{i\,\epsilon_k} \end{pmatrix} \begin{pmatrix} \alpha_k \\ \alpha_{M-k}^\dagger \end{pmatrix}. \tag{3.29}$$

The pre-quench normal modes are defined similarly, adjusting the angles to θ_{k^0},

$$\begin{pmatrix} c_k \\ c_{M-k}^\dagger \end{pmatrix} = \begin{pmatrix} \cos_{k^0} & -i\sin_{k^0} \\ -i\sin_{k^0} & \cos_{k^0} \end{pmatrix} \begin{pmatrix} \alpha_{k^0} \\ \alpha_{M-k^0}^\dagger \end{pmatrix}. \tag{3.30}$$

The direct transformation between pre- and post-quench normal modes is then

$$\begin{pmatrix} \alpha_k \\ \alpha_{M-k}^\dagger \end{pmatrix} = \begin{pmatrix} \cos_{k^0-k} & -i\sin_{k^0-k} \\ -i\sin_{k^0-k} & \cos_{k^0-k} \end{pmatrix} \begin{pmatrix} \alpha_{k^0} \\ \alpha_{M-k^0}^\dagger \end{pmatrix}. \tag{3.31}$$

From this we can write the evolution of the Fourier-modes in quadratic form of the pre-quench normal modes,

$$\begin{pmatrix} c_k(t) \\ c_{M-k}^\dagger(t) \end{pmatrix} = \begin{pmatrix} \cos_k & -i\sin_k \\ -i\sin_k & \cos_k \end{pmatrix} \begin{pmatrix} e^{-i\,\epsilon_k} & 0 \\ 0 & e^{i\,\epsilon_k} \end{pmatrix} \begin{pmatrix} \cos_{k^0-k} & -i\sin_{k^0-k} \\ -i\sin_{k^0-k} & \cos_{k^0-k} \end{pmatrix} \begin{pmatrix} \alpha_{k^0} \\ \alpha_{M-k^0}^\dagger \end{pmatrix}. \tag{3.32}$$

From this line we can calculate the two-point correlation functions in real-space modes for ground-state quenches

$$\begin{aligned} \langle c_l^\dagger(t) c_j(t)\rangle = &\frac{1}{2N} \sum_{k=0}^{N-1} \exp\left(-i\frac{2\pi k}{N}(l-j)\right) \Bigg\{ 1 - \cos\theta_k \cos\delta\theta_k \\ &+ \sin\theta_k \sin\delta\theta_k \cos[2\epsilon_k t] \Bigg\}, \end{aligned} \tag{3.33}$$

$$\begin{aligned}\langle c_r^\dagger c_{r+d}^\dagger \rangle(t) = \frac{i}{2M} \sum_{k=0}^{M-1} e^{\frac{-2\pi i}{M}kd} \Bigg\{ & \sin\left(\theta_k\right) \cos\left(\theta_k^0 - \theta_k\right) \\ & + \sin\left(\theta_k^0 - \theta_k\right) \left(e^{2it\epsilon_k} \cos^2\left(\theta_k/2\right) - e^{-2it\epsilon_k} \sin^2\left(\theta_k/2\right)\right) \Bigg\},\end{aligned} \tag{3.34}$$

where $\delta\theta_k = \theta_{k^0} - \theta_k$ is the difference in pre- and post-quench Bogoliubov angles. The correlations we investigate in this work are density-density correlations,

$$\begin{aligned} g_2\left(r, r+d\right) &= \langle n_r n_{r+d} \rangle - \langle n_r \rangle \langle n_{r+d} \rangle \\ &= |\langle a_r^\dagger a_{r+d}^\dagger \rangle|^2 - |\langle a_r^\dagger a_{r+d} \rangle|^2. \end{aligned} \tag{3.35}$$

The second line in (3.35) comes about using Wicks theorem, since the model of investigation is quadratic. Density-density correlations are connected to the $C^{zz}_{r,r+d}$ correlation functions of the long-range Ising model by virtue of a Jordan-Wigner transformation [53]

$$C^{zz}_{r,r+d} = \langle \sigma_r^z \sigma_{r+d}^z \rangle - \langle \sigma_r^z \rangle \langle \sigma_{r+d}^z \rangle.$$

3.5.2 Correlation and density matrix

The correlation matrix of an FGS on N sites is a $2N \times 2N$ matrix in the space of fermionic operators, whereas the density matrix has dimensions $2^N \times 2^N$ in the space of fermionic states. If the correlation matrix is diagonal in the basis $\vec{\alpha}$, the density matrix is diagonal in the basis of Fock-states $\{|k\rangle\}_{k\in\{0,1\}^N}$ generated by the action of the operators in $\vec{\alpha}$ on the ground state $|0\rangle$. The reduced density matrix of a FGS obtained by tracing out a set of degrees of freedom is again a FGS. The same tracing out of degrees of freedom can be performed on the correlation matrix. The spectrum of the reduced correlation matrix leads to the spectrum of the reduced density matrix and from this we can calculate complex quantities such as the entanglement entropy and higher constructions of it, such as the mutual information [98, 99, 101].

3.6 Long-range coupling

The interaction range of physical models in quantum mechanical systems has initially been investigated with a hard cutoff, such as nearest neighbour lattice geometries in bosonic, fermionic or spin-models [33–35, 102, 103]. These simple setups provide an intuitive starting point, their physics have proven to be rich and have proven to be relevant approximations of many physical setups. Different approaches led into considering models on graphs such as central spin models in quantum cavity dynamics, like the Jaynes-Cummings or the Dicke model [104, 105]. Many classical theories have interactions that

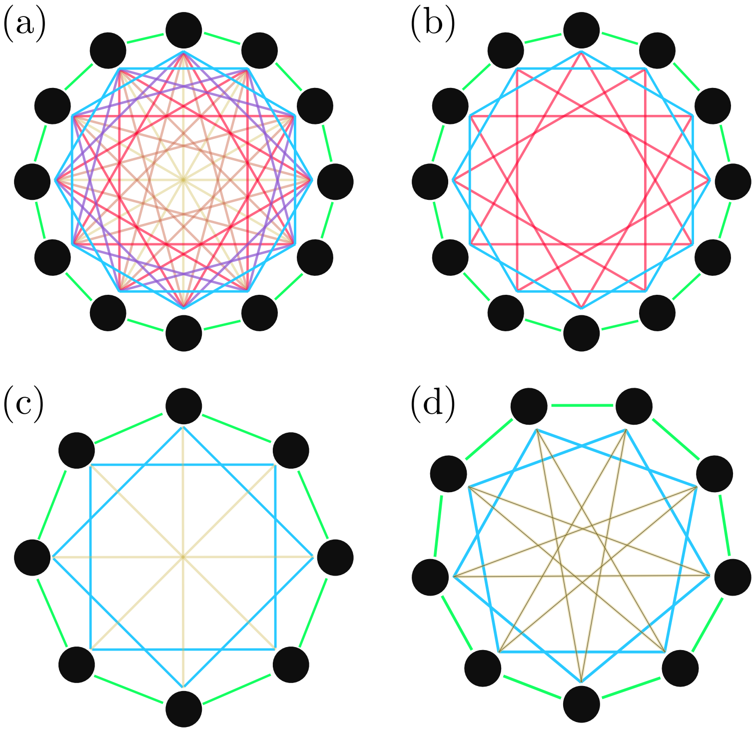

FIGURE 3.1: Different sketches for the two considered coupling-models. Different colours denote couplings at different distances. The strength of couplings at a fixed distance d is J_d. The models have the ring as the $\alpha \to \infty$ limit. (a) Dense long-range coupling, also called the dense algebraic model, where every site is connected to every other site. At $\alpha = 0$ this is the all-to-all model. (b) Sparse coupling between sites separated by powers of 2, also denoted as PWR2 coupling. The number of sites is not a power of 2 and therefore the furthest coupling is present twice. In this example the furthest coupling forms a 3-cycle or a triangle. (c) PWR2 coupling for a system size that is a power of 2. The furthest coupling is present only once and thus forms a line. (d) PWR2 coupling for a system size one less than a power of 2. The furthest coupling forms a hamiltonian cycle going through all sites of the system.

decay algebraically with distance such as gravity and electromagnetism. Employing such algebraic decay of the interaction strength $J_r \sim \frac{1}{r^\alpha}$ into quantum mechanical systems has led people to investigate the cross-over from the local to the non-local regime. In the local regime, the local energy density remains finite when the system is brought into the thermodynamic limit. For the non-local regime, the long-range contributions to the local energy density diverge as $\int r^{-\alpha} d^D r$ and renormalization is necessary to keep the theory finite [50, 78, 83]. This is known as the Kac prescription. As an example, consider a translation-invariant, quadratic fermionic Hamiltonian as investigated in 3.4.1. We set $\Delta = 0$ and write the exchange term as an algebraic decay over the site-indices,

$$J_{|s-r|}(\alpha) = \begin{cases} 0, & \text{if } s = r \\ \frac{J_1}{|s-r|^\alpha}, & \text{if } s \neq r. \end{cases} \tag{3.36}$$

This setup is shown in Fig. 3.1(a). Writing $d = |s - r|$, the local energy density is then given by

$$\sum_{d=1}^{N-1} J_d(\alpha) = J_1 \sum_{d=1}^{N-1} \frac{1}{d^\alpha} = J_1\, W_{N-1,\alpha}, \tag{3.37}$$

where $W_{N-1,\alpha}$ is known as the generalized harmonic number of order α. For $\alpha > 1$, the limit $N \to \infty$ exists and is equal to the Riemann Zeta-function,

$$\lim_{N\to\infty} W_{N-1,\alpha} = \zeta(\alpha) = \sum_{n=1}^{\infty} \frac{1}{n^\alpha}. \tag{3.38}$$

Comparing this to e.g. Newtonian gravity and electromagnetism, which both decay quadratically with distance, we see that our chain-like Fermion model (a lattice with dimension $D = 1$ with additional long-range terms) is working without problems for $\alpha > D = 1$. For $\alpha < D$, such as the all-to-all spin-model which is equivalent to $\alpha = 0$, require a proper normalization by the Kac prescription. This keeps the local energy density constant for changing system size N into the thermodynamic limit. The exponent separating the local and the non-local regime is $\alpha^* = D$. For consistency this prescription can also be employed at values of α where the local energy density does not diverge inherently. This normalized coupling function is then given as

$$\tilde{J}_d(\alpha) = \frac{J_1}{W_{N-1,\alpha}} \frac{1}{|s - r|^\alpha}. \tag{3.39}$$

The Kac prescription does not turn a non-local model into a local one, but enables consistent investigation at any decay-exponent. Notably, this also includes negative exponents $\alpha < 0$.

3.6.1 Sparse long-range coupling

With increased control over atomic configurations in Rydberg tweezer arrays and in gate-based quantum computation [26–32], the physical grounding for dense long-range coupling can be relaxed, and sparse coupling-graphs can be experimentally approached [106, 107]. With this, the theoretical investigation of these setups becomes more important. Sparse coupling graphs require a different set of resources. In the gate based approach of Kuriyattil et al. [1], the shuffling operations were faster than the interaction operations, and this reduction of resources might be possible to engineer in the Hamiltonian models as well. Whether properties from dense long-range coupling graphs carry over to sparse long-range coupling graphs is an area of active research, of which the results in this thesis are a part.

An example of a sparse coupling-graph is the coupling of any two sites whose chain-like distance is a power of a prime number p,

$$J_d(\alpha) = \begin{cases} \frac{1}{d^{\alpha}}, & \text{if } \log_p(d) \in \mathbb{N}, \\ 0, & \text{otherwise.} \end{cases} \tag{3.40}$$

This model is motivated by the possibility of connecting such a model to the mathematics of p-adic field theory [39, 40], and a sketch of the geometry is shown in Fig. 3.1(b)&(c). We again ask about the critical exponent α^* separating the local and non-local regimes. In the dense model, we identified this as $\alpha = D$. We write the distance as $d = p^r$, where $r \in \{0, \log_p(N) - 1\}$. This yields

$$\sum_{r=0}^{\log_p(N)-1} J_d(\alpha) = \sum_{r=0}^{\log_p(N)-1} \frac{1}{p^{r\cdot\alpha}} = \frac{1 - p^{-\left(\log_p(N)\right)\alpha}}{1 - p^{-\alpha}} = \frac{1 - N^{-\alpha}}{1 - p^{-\alpha}}, \tag{3.41}$$

where the second equation uses the formula for the geometric series. In the thermodynamic limit $N \to \infty$ (3.41) remains finite for $\alpha > 0$, so $\alpha^* = 0$. Another example uses additive distances instead of multiplicative ones. We define the n-th Fibonacci number as f_n, and with the starting values $f_0 = 0$ and $f_1 = 1$ the recursive relation is

$$f_{n+2} = f_{n+1} + f_n, \quad n \in \mathbb{N}. \tag{3.42}$$

Different additive relations are the Tribonacci numbers, which have been investigated in many-body localization research [16, 108]. With the set of Fibonacci numbers $\{f_n\}_{n\in\mathbb{N}}$, we define

$$J_d(\alpha) = \begin{cases} \frac{1}{d^{\alpha}}, & \text{if } d \in \{f_n\}_{n\in\mathbb{N}}, \\ 0, & \text{otherwise.} \end{cases} \tag{3.43}$$

Using the ratio test for the convergence of local energy density gives

$$\lim_{n\to\infty} \left| \frac{f_n}{f_{n+1}} \right|^{\alpha} = \phi^{-\alpha}, \tag{3.44}$$

where $\phi = \frac{1-\sqrt{5}}{2}$ is the golden ratio. From this we get $\alpha^* = 0$. Another way of seeing that both the sparse prime graph and the sparse Fibonacci graph have $\alpha^* = 0$ is to realise that both the powers of primes and the Fibonacci numbers grow exponentially. The algebraic attenuation via α is not strong enough to overcome this, and as such the convergence remains valid for $\alpha > 0$. We can contrast this both with the dense long-range coupling with simple algebraic decay, but also with sparse long-range coupling of a quadratic form

$$J_d\left(\alpha\right) = \begin{cases} \frac{1}{d^{\alpha}}, & \text{if } \sqrt{d} \in \mathbb{N}, \\ 0, & \text{otherwise.} \end{cases} \tag{3.45}$$

In the thermodynamic limit, we find the critical exponent α^* in the same way as in the dense long-range coupling, since the square can be absorbed into the exponent

$$\lim_{N\to\infty} \sum_{d=1}^{N-1} J_d\left(\alpha\right) = \sum_{d=1}^{\infty} \frac{1}{d^{2\alpha}} = \sum_{d=1}^{\infty} \frac{1}{d^{\beta}} = \zeta\left(\beta\right). \tag{3.46}$$

Here we wrote $\beta = 2\alpha$, and from the convergence of the ζ-function we find $\alpha^* = 0.5$.

3.6.2 Spectrum, group velocity and density of states

Following the derivation in section 3.4.1, the Fourier-transformation of the coupling and the pairing functions, $\mathscr{J}_k$ and $\mathscr{D}_k$, respectively, form the energy of the normal modes via (3.19). We set $\Delta = 0$, such that the coupling function $\mathscr{J}_k$ is equivalent to the dispersion relation ϵ_k. From this we then derive properties of the spectrum, the group velocity v_k^{gr} and the density of states (DOS) D_k

$$v_k^{gr} = \frac{N}{\pi}\frac{d\epsilon_k}{dk}, \tag{3.47}$$

$$D_k = \frac{N}{\pi}\left|\frac{d^2\epsilon_k}{dk^2}\right|^{-1}. \tag{3.48}$$

The coupling function takes the form

$$\mathscr{J}_k\left(\alpha\right) = \left\{2\sum_{d=1}^{N} J_d\left(\alpha\right)\cos\left(\frac{2\pi k}{N}d\right)\right\} - S_k, \tag{3.49}$$

where $S_k = J_{N/2}\cos\left(\frac{2\pi k}{N}\frac{N}{2}\right) = -J_{N/2}$ accounts for the fact that the furthest distance in the ring-geometry appears without partner when the number of sites is even, $N/2 \in \mathbb{N}$. This term does not dictate the overall functional behaviour of $\mathscr{J}_k\left(\alpha\right)$ and is omitted for the further derivations. We see from (3.49) that at $k = 0$ we obtain the L^1-norm of all the coupling terms via Plancherels theorem, which is equivalent to the value for the Kac prescription. As such, $\mathscr{J}_{k=0}\left(\alpha\right)$ diverges for $\alpha < \alpha^*$.

3.6.2.1 Dense algebraic coupling

Going one step back in the derivation of (3.49), using $\tilde{k} = \frac{2\pi k}{N}$ and taking the thermodynamic limit such that $\tilde{k} \in [0, 2\pi)$, we write for the dense algebraic coupling,

$$\begin{aligned} \mathscr{J}_{\tilde{k}}(\alpha) &= J \sum_{d \in \mathbb{Z} \backslash 0} \frac{e^{-i\tilde{k}d}}{|d^\alpha|} = J \left[\mathrm{Li}_\alpha \left(e^{i\tilde{k}} \right) + \mathrm{Li}_\alpha \left(e^{-i\tilde{k}} \right) \right] \\ &= 2J\mathrm{Re} \left[\mathrm{Li}_\alpha \left(e^{i\tilde{k}} \right) \right] . \end{aligned} \tag{3.50}$$

Here, $\mathrm{Li}_\alpha(z)$ is the polylogarithm of order α and argument z. It's important to note that in (3.50) the boundary-term $S_{N/2}$ is omitted, restricting the validity to $\alpha > 0$. From the rules for the polylogarithm we can understand the behaviour of the derivatives of $\mathscr{J}_k(\alpha)$,

$$\frac{\partial \mathscr{J}_k(\alpha)}{\partial k} \propto \frac{\partial \mathrm{Li}_\alpha \left(e^{ik} \right)}{\partial k} = i \, \mathrm{Li}_{\alpha-1} \left(e^{ik} \right) \propto \mathscr{J}_k(\alpha - 1) \, . \tag{3.51}$$

This relation and iterations on it show that if $\mathscr{J}_{k=0}(\alpha < \alpha^*)$ diverges, then its n-th partial differential diverges for $\alpha < \alpha^* + n$. This divergence is carried through to the dispersion relation ϵ_k and its derivatives, the group velocity and the density of states,

$$\begin{aligned} &\lim_{\alpha \to 2^+} v^{gr}_{k=0}(\alpha) \to \infty, \\ &\lim_{\alpha \to 3^+} D_{k=0}(\alpha) = 0. \end{aligned} \tag{3.52}$$

Divergence of the group velocity implies the possibility for infinitely fast information transport. However, the density of states is suppressed even stronger, such that $\lim_{k \to 0} v^{gr}_k D_k \to 0$ for $\alpha < 2$. As such, whilst there is some correlation buildup, it is minuscule and the majority of transport happens at lower speeds. Nonetheless, the divergence of the group velocity heralds the rarefaction of the lightcone, as will be presented later.

3.6.2.2 Sparse prime-power coupling

In analogy to the dense calculation, we investigate what happens for the sparse coupling graphs where sites are connected iff their ring-distance is a power of a prime, see (3.40). A theorem by Hardy [109] guarantees the following:

Theorem 3.1. *For every real number $b \geq a > 1$ the function*

$$W(t) = \sum_{l=0}^{\infty} a^{-l} e^{\left(i \, b^l t \right)} \tag{3.53}$$

is bounded and continuous on $\mathbb{R}$ with no points of differentiability

For $b = p$ a prime and $a = p^{\alpha}$, the theorem directly applies to the coupling function of the PWRp graphs (3.40). Therefore, even before the crossover $\alpha^{*} = 0$, the coupling function undergoes a dramatic change, becoming non-differentiable for $\alpha < \alpha^{*}_{\text{Hardy}} = 1$. For $\alpha \geq 1$, $\mathscr{J}_k(\alpha)$ is smooth, while for $\alpha < 1$, it is bounded, continuous, and nowhere differentiable. If the pairing function $\mathscr{D}_k$ is non-pathological (smooth), we see from the chain-rule that this non-differentiability of $\mathscr{J}_k$ carries over to the dispersion-relation ϵ_k. The derivatives of the coupling function (if well-defined) relate in the same way back as in the dense case

$$\frac{\partial^2 \mathscr{J}_k(\alpha)}{\partial k^2} \propto \frac{\partial \mathscr{J}_k(\alpha - 1)}{\partial k} \propto \mathscr{J}_k(\alpha - 2)\,. \tag{3.54}$$

Thus, for the PWRp graphs, the shifted crossovers between dispersion-relation, group velocity and density of states does not only apply to the local - non-local transition (given by $\alpha^{*} = 0$), but also to the smooth - non-differentiable transition (given by $\alpha^{*}_{\text{Hardy}} = 1$). Across this second transition, the dispersion-relation remains bounded and Lipschitz-continuous. Thus, the group velocity will not diverge at $\alpha^{*}_{\text{Hardy}}$, but merely ill-defined. We expect the light-cone picture to remain intact insofar as that correlations are suppressed outside the light-cone, although within the light-cone dynamics can be complicated.

3.6.2.3 Monna map

The structure of the PWRp model is such that for $\alpha < 0$, which favours long-range coupling over short-range coupling, we can employ a transformation to return the structure to the local case. The special case of $p = 2$ is called the Monna map. Expression of the site-numbers in base 2 indicates directly which component sites are connected, as their Hamming distance is exactly 1 - a single bit is flipped. Large euclidean distances are encoded in later bits, and so to transform large distances to small ones one can flip the order of bits. Consider a number w expressed in base 2,

$$w = \sum_{s=0}^{Q} c_s 2^s, \tag{3.55}$$

where $c_s \in \{0, 1\}$ are the states of the bits and $Q = \lfloor \log_2(w) \rfloor$ is the length required to represent w. The Monna map $\mathscr{M}$ acts as

$$\mathscr{M}(w) = \sum_{s=0}^{Q} c_{Q-s} 2^s. \tag{3.56}$$

A further visual example is given by table 3.1, as well as in Fig. 3.2.

Base 10	Base 2	$\mathscr{M}$
5	101	101
12	1100	0011
20	10100	00101

TABLE 3.1: Illustration of the action of the Monna map

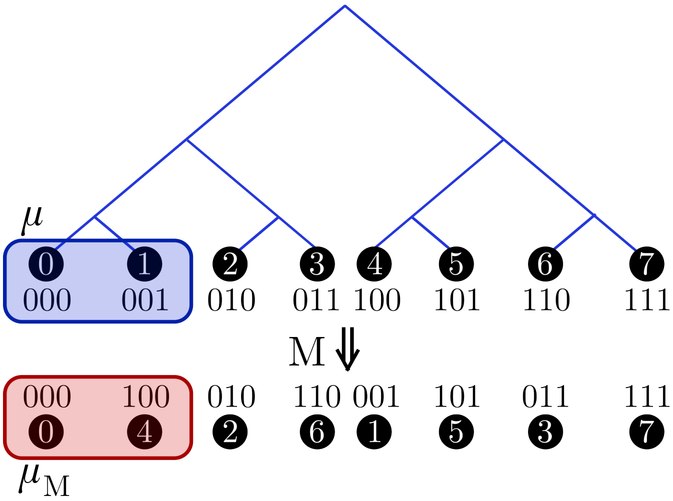

FIGURE 3.2: Action of the Monna map from the construction of binary numbers via the binary tree. The Monna map flips the reading order of the bits, which is mathematically described by (3.56). For later use, we also show different partitions of a set of numbers. For the euclidean geometry, the partition μ (blue box) takes a contiguous set of numbers. In the ultrametric geometry, the partition μ_M (red box) takes again a contiguous set of numbers, where contiguity is however described in the ultrametric space. Extensions to bigger partition sizes generalize naturally from the plot.

3.6.2.4 Phase-transitions

With the squeezing function being chain-like (see (6.2)) and dispersion relation (3.19) we can directly investigate points at which the energy gap between the ground-state and the first excited state vanishes. Both constituents of the sum in (3.19) are strictly positive, so for $\epsilon_k = 0$, we independently require $\mathscr{J}_k = 0$ and $\mathscr{D}_k = 0$. The general description of this is made in [53] and can at least functionally be written down explicitly for the quadratic, translationally invariant fermionic models. For the purpose of this thesis, we specify the squeezing function to be derived from a nearest-neighbour squeezing interaction, resulting in (6.2). Fixing the squeezing function, criticality by closing the spectral gap is possible at $\tilde{k} \in \{0, N/2\}$, given N is even. Since $J_{|s-r|} \geq 0$ for all arguments and $\mathscr{J}_{k=0} = \sum_d J_d$, the only remaining wave-number is $\tilde{k} = N/2$

$$\mathscr{J}_{N/2} = 2\left\{\sum_{d=1}^{N/2} J_d \cos \pi d\right\} - S_{N/2}. \tag{3.57}$$

The closing of the gap depending on the value (3.57) is discussed in chapter 6.

3.7 Summary

In this chapter, we explained how the specific models we investigate, quench-dynamics in translationally invariant quadratic fermionic models, simplify the analytical and numerical treatment from the full problem of just propagating the full system-wavefunction. In sections 3.2 and 3.3 we described the quantities we aim to investigate in our models, the Lieb-Robinson velocity via correlation spreading and the tripartite mutual information (TMI). Section 3.4 expanded on the general treatment of fermionic and bosonic quadratic models, explaining the full diagonalization techniques based on the Bogoliubov-Valatin transformation. We focused on fermionic models in section 3.5, where a particular subgroup of quantum states, the fermionic gaussian states (FGS) are explained. Section 3.6 investigated the peculiarities of the long-range coupling that is inherent in the models we consider. Not only is the difference between dense and sparse models illuminated, but more specifics in the sparsity-patterns of sparse models are highlighted. The theory developed in this chapter is used in chapter 6 to investigate the numerical and analytical results for the translationally invariant quadratic fermionic models.

Coming back to where you started is not the same as never leaving.

Terry Pratchett, A Hat full of Sky

4

Recurrence dynamics in single particle systems

In this chapter we will use the theory on recurrence developed in chapter 2 to analyse recurrence and absence time scaling in single-particle setups. The setups we investigate are prototypical for experiments in atomic, molecular and optical (AMO) physics [29–32, 110] and also quantum computing tasks. A single excitation local in position interacts with a graph of sites, with the dynamics being unitary. Wherever only one of either recurrence or absence time is shown, the scaling of the other one is the same and hence omitted. The scaling by spatial size N of the setup requires a canonical way of increasing the system size. This is typically done by naming the graph and should be understood trivially. The same goes for the initial state on the graph, which in the single particle state extends trivially to larger sizes. A single excitation is localized on one site, the rest of the sites are empty. The results are broadly split into three parts, in line with three major (not independent) ways of modifying the simple Hamiltonian shown in (4.1). For each of these parts results are shown that illustrate the impact of modulating this hyperparameter. After the first recurrence time has been addressed, we show results for the statistics of the recurrence and absence times following the orbit of the same initial state. This makes it possible to clearly see the ballistic behaviour in some configurations, while it is completely absent in others.

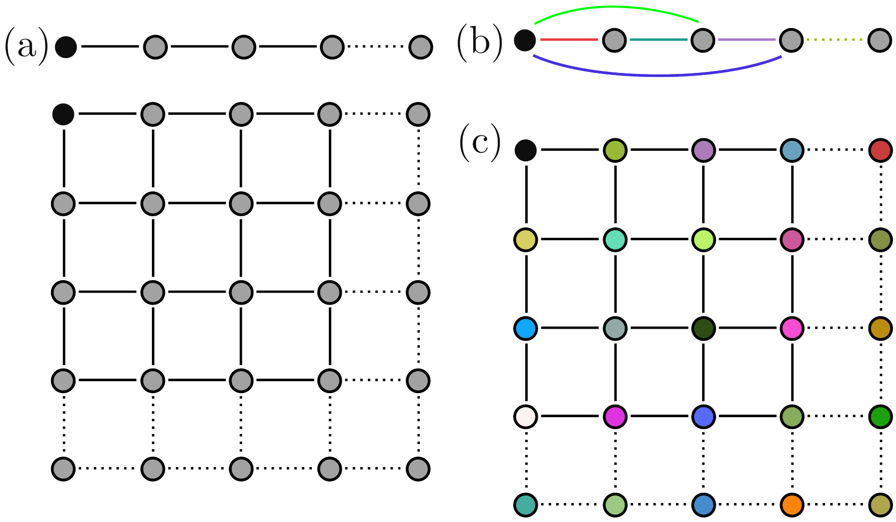

FIGURE 4.1: Sketch of the three different hyperparameters we address in the results of this chapter. The site in black is the initial position of the excitation, the **probe** on the full graph G. The remaining sites constitute the **bath**. Dashed edges signal the 'canonical' extensions of the graph by adding more sites. (a) Different graph geometries, the most obvious being lattices of arbitrary dimensions. (b) Modulating the coupling strength between sites is signalled by different colours of the edges. This technically also falls under bath-geometry shown in (a), but here we specifically consider modulations in different coupling, whereas the coupling-strengths in (a) are equal. (c) Modulating the on-site energies, shown by different colours in the sites.

4.1 Setup

Different variations on non-interacting, single particle model we consider are sketched in Fig. 4.1. They are all sharing the feature of an excitation on a single site (which we label as site 0), which is part of a simple connected graph G with a set of labelled sites $i \in V(G)$ and edges $(i,k) \in E(G)$ connecting sites $i,k \in V(G)$. The graph excluding site 0 forms our finite effective **bath**. Site 0 we call the **probe**. The tight-binding Hamiltonian of this setup is written as

$$\mathscr{H} = \sum_{i\in V(G)} \omega_i a_i^\dagger a_i + \sum_{(i,k)\in E(G)} J_{i,k} \left(a_i^\dagger a_k + \text{h.c.} \right), \tag{4.1}$$

where $a_i^\dagger$ (a_i) are the creation (annihilation) operators of a particle on the ith site, ω_i is the strength of the on-site term of the ith site, and $J_{i,k}$ is the tunnelling strength between sites i and k. The different hyperparameters sketched in Fig. 4.1 refer to modulations of different parts in the Hamiltonian (4.1). Modulating the geometry refers to changing the set of edges $E(G)$ while keeping the weights of all edges equal. Modulating the couplings changes the set of edges $E(G)$ but also their weights $J_{i,k}$, resulting in a weighted graph G. Modulating the on-site energies changes the ω_i. In this chapter we investigate the single-particle sector of the particle-number conserving Hamiltonian (4.1), which in the computational basis can be decomposed as

$$H_1 = \Omega + \mathscr{J}. \tag{4.2}$$

Here, $\Omega = \mathrm{diag}\,(\omega_0, \omega_1, ..., \omega_N)$ is the diagonal matrix with the on-site energies $\omega_i \in \mathbb{R}$ of sites in $V(G)$ and $(\mathscr{J})_{i,k} = J_{i,k}$ is the hermitian matrix holding the weights of edges (i,k) in $E(G)$. The **probe** site is $i = 0$, energy is considered in units of $J_{0,1}$ and time in units of $J_{0,1}^{-1}$. Throughout, we set $\hbar = 1$. For bath-scalings that change the local energy density $\sum_{(0,k)\in E(G)} J_{0,k}$, we do *not* employ a Kac normalization fixing this local energy density to a constant. Without Kac normalization the comparison of recurrence times for different sizes of graphs is more straightforward, as the smaller of the two graphs is a subgraph of the larger one.As $\mathscr{H}$ is time-independent, the time-evolution operator is given by a simple exponential $U(t) = \exp\left(-i\mathscr{H}t\right)$, calculated, unless specified otherwise, using numerical exact diagonalization. This means that the eigenvectors and eigenvalues of H_1 are calculated numerically, and with these the matrix-exponential in *scipy* is used. The initial state of the **probe** holds one particle, while the **bath** is empty, $\sum_{j\in V(G)\setminus 0}\langle a_j^\dagger a_j\rangle = 0$. This relation fully specifies the bath initial-state for any bath size. All considerations in this chapter are equivalent to a continuous time quantum random walk (CTQW) of one particle on a weighted graph [111–113]. There are two conventions in the literature of CTQW. The first is using a direct correspondence to continuous time *classical* random walks (CTCW). There, the diagonal elements of H_1, the elements of Ω, are fixed by the N conditions $\omega_k = -\sum_{s\neq k} J_{s,k}$. This way, the matrix H_1 is fully determined by $\mathscr{J}$ and is proportional to the Laplacian of the weighted, symmetric graph G. IN CTCW, the Laplacian serves as the transition-rate matrix and the conditions on the diagonal elements ensure conservation of probability. In quantum mechanics however, conservation of probability is inherent in the normalization of the wavefunction, and the conditions on the diagonal elements are not necessary. Therefore, the energy-detuning of a site can be changed independently of the coupling strengths to other sites. This is the second convention in the literature of CTQW. Since it is compatible with the freedom found in experimental setups, it is the one used in this thesis. For the single particle case, the Hilbert-space of the problem scales linearly with the size N of the graph $G(N)$. This in turn upper bounds the effective dimension (2.2) of initial states to linear scaling.

4.2 Recurrence for different graph geometries

In this section we present the results for a small collection of different graph geometries that display a wide range of different qualities. As mentioned in the previous section, different graph geometries amounts to different sets of edges $E(G)$, where each edge has the same weight $J = J_{0,1}$.

4.2.1 The chain

The simplest setup is a chain. Its single-particle Hamiltonian (4.2) is a tridiagonal symmetric Toeplitz matrix with ω on its diagonal and J on its first off-diagonals. This matrix can be explicitly diagonalized, but we will not use analytical solutions for obtaining our results. For the results in Fig. 4.2, we used $\omega = 0$. In (a) we show the scaling of the first absence time with bath size, $T_A^p(N) \propto N$ and in (b) an example of the dynamics of the particle through a bath with $N = 100$. The linear scaling of $T_A^p(N)$ fails once the reflected waves profile is not coherent enough to trigger the threshold p. Hilbert-space dimension, effective dimension of the initial state and graph radius all scale linearly with N, making this setup our starting point. Modifications to the bath will distinguish these three quantities and provide some insight into the relevant features for maximizing absence time scaling with bath-size.

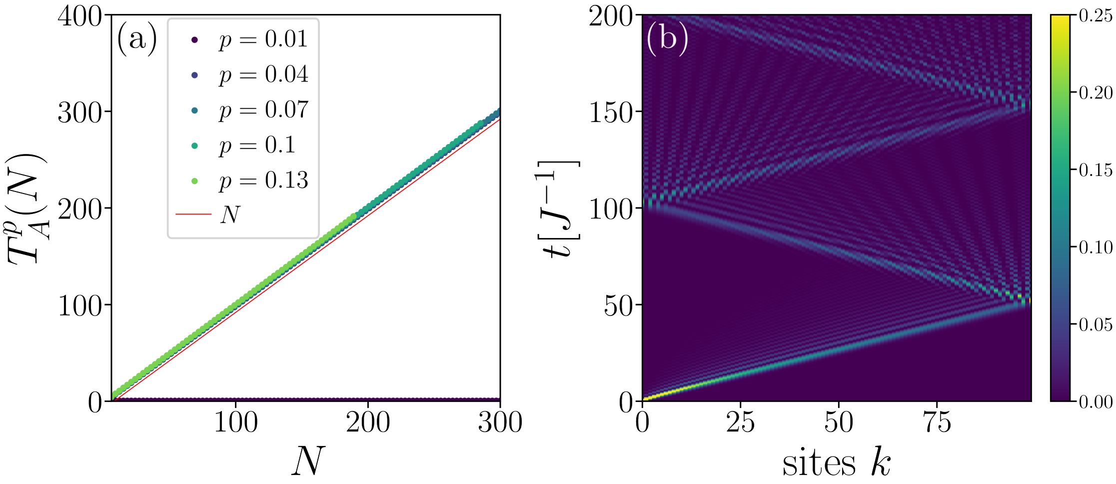

FIGURE 4.2: Absence time scaling and instructive dynamics through the chain. (a) The absence time scales linearly with bath size N, which is also the Hilbert space dimension, the effective dimension and the graph radius. As such, the chain is our prototypical setup from which we investigate deviations. The absence time for the threshold $p = 0.01$ is constant and indicates that too low a threshold samples only local reflections. (b) The dynamics of the single particle on the chain is fully ballistic. The absence time is related to the group-velocity, as the initial state is spread over all momentum modes. The particle explores the whole chain and returns in linear time $\propto N$.

4.2.2 Lattices

The intuition of the chain extends to the square lattice. Most of the analysis for the chain repeats for higher-dimensional square lattices, which are given as iterative Kronecker products of the chain. Our system site is one corner of the lattice, the bath consists of all other sites. Fig. 4.3(a) shows the absence time scaling $T_A^p(N) \propto \sqrt{N}$, which is explained by Fig. 4.3(b). There, the dynamics of the particle in terms of distance to the system-site are shown. The $M \times M$ square lattice has a radius of $2\,(M-1)$. For each $k \in \{0, 1, \cdots, 2\,(M-1)\}$, we write as N_k the collection of sites that are a distance k away from the system-site. The probability for the particle to be a distance k away from the system-site is then given as

$$P_k = \sum_{j \in N_k} \langle n_j \rangle.$$

The dynamics of $P_k(t)$ in Fig. 4.3(b) show that the exploration of the lattice is still mostly ballistic, otherwise the wavefront would not collectively move through the equidistant collections N_k. As the radius of the square lattice scales as a square root $R(G(N)) \propto \sqrt{N}$, this ballistic flow through N_k makes the first absence time scale in the same way, $T_A^p(N) \propto \sqrt{N}$.

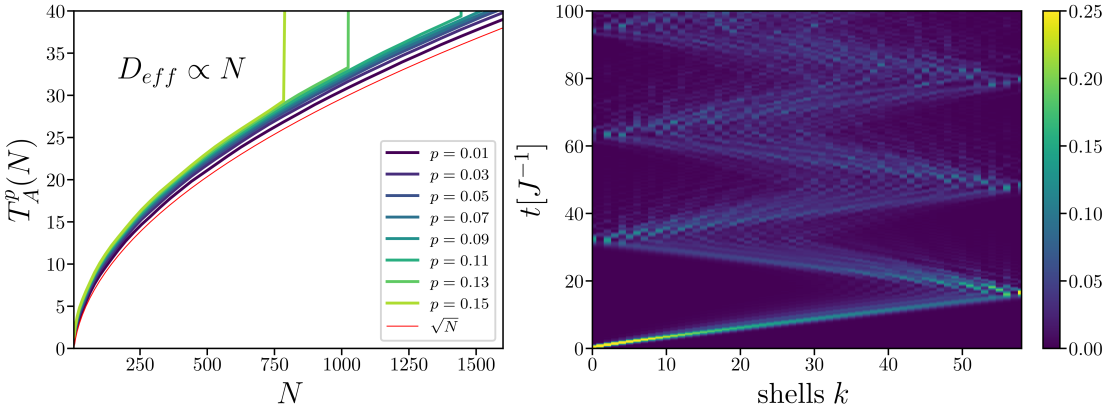

FIGURE 4.3: Absence time scaling and shell dynamics through the square lattice. (a) The absence time scales linearly with edge-length $\sqrt{N}$, which is also the graph radius. This behaviour extends to all higher dimensional lattices constructed from Kronecker products of the chain. At the $p = 0.13$ line, we see a steep increase. This is due to the returning wave-package (after the ballistic traversal through the lattice) not being high enough to trigger the threshold anymore. The absence time increases dramatically and is not tracked anymore. (b) The dynamics of the single particle on the lattice is here shown in terms of shells, i.e. collections of sites of constant distance to the system-site. In terms of shells, the exploration of the system is ballistic, which corroborates the scaling $T_A^p(N) = \sqrt{N}$ of (a).

4.2.3 Tree-like graphs

With our system having a typical size of 1 site, a natural thought is to attach subsequent bath degrees of freedom directly to the system. In the simplest case, these degrees of freedom, subsequently called **satellites**, are independent and without loops, leading us

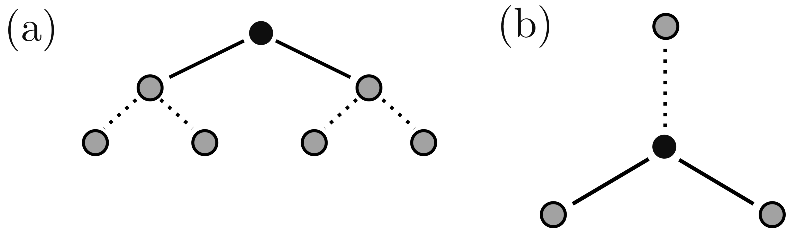

FIGURE 4.4: Sketches of two different types of tree-like graphs. As in Fig. 4.1, the site on which the particle is initially localized is shaded in black. In these examples, it is always the central site. (a) This graph corresponds to the n-ary tree. For $n = 2$ it is the binary tree, for $n = 3$ it is known as the Bethe lattice. Extending this graph is done by increasing the tree-depth, shown by the dashed edges. (b) This graph is the prototypical star graph. Here it is not relevant that the satellites, i.e. the different disjoint subgraphs attached to the central site, are trivial one-site graphs. They could also be composed of finite depth n-ary trees as in (a). Relevant is that they are mutually disjoint and that the extension is made via attaching more satellites, instead of extending the satellites, which falls under (a).

to tree-like graphs, shown in Fig. 4.4. The simplest of these is the star graph in Fig. 4.4, whose single-particle Hamiltonian is given by an arrowhead matrix.

$$H_1 = \begin{pmatrix} d_0 & J_{0,1} & J_{0,2} & \cdots & J_{0,N-1} \\ J_{0,1} & d_1 & 0 & \cdots & 0 \\ J_{0,2} & 0 & d_2 & 0 & \cdots \\ \vdots & \vdots & \cdot & \cdot & 0 \\ J_{0,N-1} & 0 & \cdots & 0 & d_N \end{pmatrix} \tag{4.3}$$

We will here consider $d_j = d_0 = c$. Using a global rotation we can set $c = 0$ and use the Cauchy interlacing theorem, which shows that the spectrum of (4.3) has an $N-2$ times degenerate eigenvalue of 0. Only the first row and column of H_1 are nontrivial and given by $r_0 = (0, J_{0,1}, J_{0,2}, ..., J_{0,N-1})$. The two different eigenvalues are given by $\lambda_{1,2} = \pm\sqrt{\sum_{k>0} J_{0,k}^2}$. The initial state fidelity (2.6) has, for any initial state, at most two frequencies. Additionally, when adding more sites to the bath, the frequencies get larger and thus the timescale of recurrence goes down. The star graph with $\omega_i = \omega_0$ and $J_{0,k} = J_{0,1}$ has non-trivial eigenvalues $\lambda_{1,2} \propto \sqrt{N} J_{0,1}$ and thus features the scaling of the first absence time with the inverse square-root of the bath size,

$$T_A^p(N) \propto \frac{1}{\sqrt{N}} \tag{4.4}$$

Nonuniform coupling strengths or on-site energies do not save this situation. The effective dimension scaling improves, but absence times are still of order 1 as the particle flows from the central site to satellites and back. Larger trees, where the satellites are graphs instead of single sites, changes the situation. The ballistic heuristic suggests a scaling according to the scaling of the smallest graph radius among satellites. This raises the question why not to remove this bottleneck (the fastest recurring satellite), but once this is done, another satellite is the smallest. In the single-particle dynamics, the satellite dynamics are trivial and disconnected as soon as the system site is not occupied. As such, only the dynamics of a single satellite need be considered, which are the dynamics of a graph that itself is smaller than N. If there should be any chance for these dynamics to destructively interfere with those of another satellite, there would need to be some sort of phase-difference, which due to the tree-like structure, disallowing non-trivial in the graph, is impossible. In technical terms, we look at one satellite. If the scaling of the first absence time were superlinear in satellite-size for this satellite, the remaining satellites are obsolete and one could instead construct the larger version of the graph of the satellite, as the superlinearity implies $T_A^p(N_1) + T_A^p(N_2) < T_A^p(N_1 + N_2)$. Put differently, the absence time is dominated by the shortest absence time of any of the satellites (as they do not interact with one another). If this shortest absence time scales superlinearly, the other satellites are unnecessary and there is no need to consider them at all, but instead just the one satellite. Tree-like graphs highlight the peculiarities in the single-particle considerations. For a many-body setup, we would expect nontrivial interactions between satellites mediates via the central site that may lead to persistent entanglement on longer timescales. However, since in the single-particle case the different satellites cannot interact and their dynamics are fully independent, superlinear scaling is not possible.

4.2.4 General trends in recurrence time scaling for modulated graph geometries

From the underlying ballistics associated with the Schrödinger equation and the initial state being position-localized on site 0, an educated guess for the first absence time scaling with bath-size is linear in graph-radius $R(G; 0)$

$$T_A^p(N) \propto R(G(N); 0). \tag{4.5}$$

The graph-radius from site 0 is here defined as the largest of the minimal path-lengths between site 0 and sites of the bath. In absence of non-trivial structure in on-site energies and tunnelling strengths, the deviations from (4.5) can be traced directly to bath-extensions that change the degree (and with it the local energy density) of the probe-site. The illustrative example for this is the family of star graphs touched upon in section 4.2.3 and shown in Fig. 4.4. From (4.5) we also spot that, contrary to intuition, high-dimensional lattices are worse with increasing dimension d, as the radius scales as $R(G(N)) \propto N^{-d}$, which is also seen in section 4.2.2.

4.3 Tunnelings

With the ballistic behaviour of the setups in section 4.2 apparent, modulation of tunnelings serves to slow transport within the bath down. We do not consider modulations that create couplings that grow arbitrarily large with system size, and thus the spectral radius of the single-particle Hamiltonian grows slowly. Local variations in tunnelings lead to enhanced backflow of the particle. Whether our setup creates a non-trivial scaling for the absence time depends crucially on this. Modulation of couplings will also entail couplings of long-range behaviour. These setups will change the local energy density of the system. Kac normalization is not employed such as to keep the proper marginalization of larger into smaller baths intact. This however puts a limit to the long-range couplings, as the local energy density should not diverge in the thermodynamic limit $N \to \infty$. This is typically referred to as the local regime, where the influence of the long-range coupling does not change the effective dimension of the setup.

4.3.1 Decaying coupling functions - Speedwagon

Slowing down an excitation traveling through the bath suggests iteratively reducing the coupling strength between site-collections N_k of increasing distance to the system-site. From section 4.2, the chain has proven to be the most promising geometry. We are hence interested in a coupling function J with $J_{k,k+1} > J_{k+1,k+2}$, where $k \in \{0, 1, \cdots, N-2\}$. Thinking about this as a wagon rolling uphill, we refer to this as the **Speedwagon** setup. For a given coupling function J, our estimate of the first absence time is given by twice the traversal time, which itself is estimated by the sum of pairwise interaction times $t_{k,k+1} = J^{-1}_{k,k+1}$.

$$T_{traversal}(N) \propto \frac{1}{2}\sum_{k=1}^{N-1} t_{k,k+1} = \frac{1}{2}\sum_{k=1}^{N-1} J^{-1}_{k,k+1} \tag{4.6}$$

For polynomial decay, $J_{k,k+1} \propto k^{-\alpha}$, the estimate (4.6) is polynomial, $T_{traversal}(N) \propto N^{\alpha+1}$. We find however that this is never realised. For any $\alpha > 0$, backflow leads to localization and the absence time does not scale at all with bath size. Using instead a geometrical (or exponential) decay in J makes the estimate itself exponential, and it turns out that there is some success associated with this strategy. Following the results in Fig. 4.5, the coupling function is given as

$$J_{k,k+1} = 1/q^k = 1/1.01^k, \tag{4.7}$$

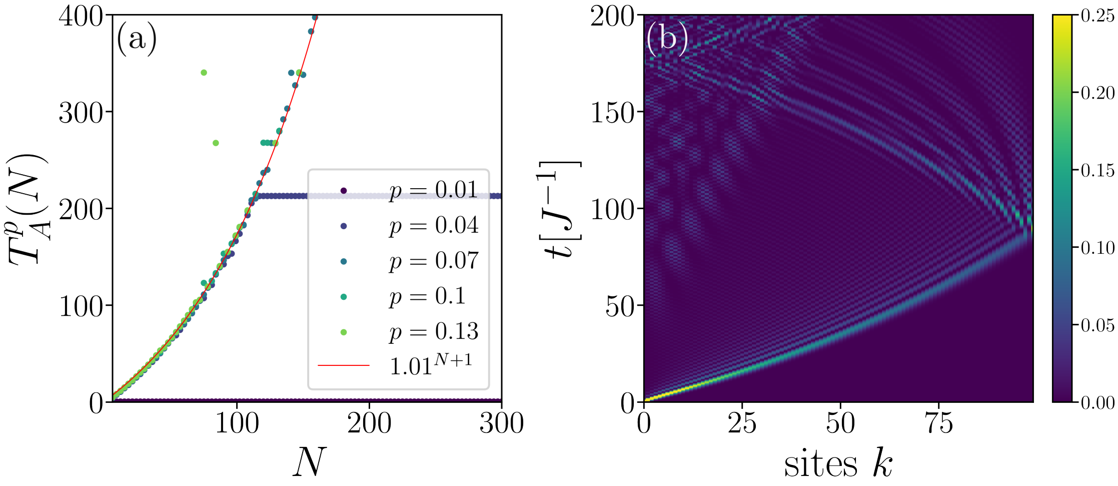

FIGURE 4.5: In the Speedwagon setup, the iteratively weaker and weaker coupling to more remote bath sites leads to an exponential scaling for the absence time in chain size. (a) This scaling does not persist, neither in the absence time nor in the effective dimension. Partial reflections in the bulk of the bath conspire to trigger a chosen threshold and subsequently added bath sites have no effect - the scaling stops. (b) The nonlinear traversal through the chain is evident. Comparing this to 4.2(b), the presence of stronger partial reflections is evident, as the system site features slight population even before the return of the wave-packet.

and the estimate of the absence time following from this is shown in red in Fig. 4.5(a)

$$T_A^p(N) \propto \sum_{k=1}^{N-1} J_{k,k+1}^{-1} = \sum_{k=1}^{N-1} 1.01^k = \frac{1.01^{N+1} - 1}{0.01}. \tag{4.8}$$

From the geometric series used in the scaling (4.8) the chain limit $\lim_{q\to 1} T_A^p(N) \propto N$ is recovered. The closer q is to 1 from above, the longer the exponential scaling (4.8) persists, but the more meaningless it becomes. This is reflected in the scaling of the effective dimension (Fig.4.5(a) inset). For any $q > 1$, there is a superlinearly scaling region, followed by a plateau, which indicates that the absence time cannot scale indefinitely. This plateau occurs later and later for q closer to 1, but the superlinear region is less extreme in turn.

4.3.2 Long-range coupling

In non-interacting models, the ballistic propagation of the excitation is central to our efforts. Even when succeeding in slowing the excitation down as shown with the Speedwagon configuration in 4.5, the coherent nature of the wave-packet is still prevalent, viz 4.5(b). Departure from coherent propagation can be engineered using long-range coupling models. We consider the coupling function on a complete graph of N sites, given as $J_{j,k} = |j-k|^{-\alpha}$ [38, 50, 83]. As such, arranging the sites by increasing index reveals that this is a chain with additional long-range couplings that decay with exponent

α with distance in the chain geometry. In this section, unless specified otherwise, the long-range coupling model always refers to the example of quadratic decay, $\alpha = 2$. This case is local, as the local energy density stays finite in the thermodynamics limit, since the couplings decay sufficiently fast. In contrast, for no decay, the local energy density diverges $\propto N$. The dimension of this setup is $(N-1)$, as the sites can be embedded in $(N-1)$ dimensional space as the standard $(N-1)$-simplex [114]. The local regime is typically considered of similar interest as the case without long-range coupling, however, for the case of studying the absence time scaling, we find a drastic difference to the chain in section 4.2.1. The scaling of the first absence time is quadratic in system size. Moreover, as we can see in Fig. 4.6(a), this scaling persists for arbitrary N, as does the scaling of the effective dimension of the initial state, $D_{\text{eff}} \propto N$. The dynamics are no longer ballistic or soliton-like - the excitation gets spread over the whole bath. In contrast to other studied baths, the fidelity decay of the long-range coupling model is monotonous beyond timescales of the order $J_{0,1}^{-1}$. There are no local reflections when the excitation explores the bath, which enables an investigation of the threshold p for values scaling with bath size. A natural choice for this is $p = p(N) = \frac{1}{N}$, such that a recurrence is considered for the fidelity being stronger than the equipartition value. This connects to the classical case, where the limiting distribution is exactly the equipartition. For this case, the long-range coupling features an absence time scaling linearly with bath-size,

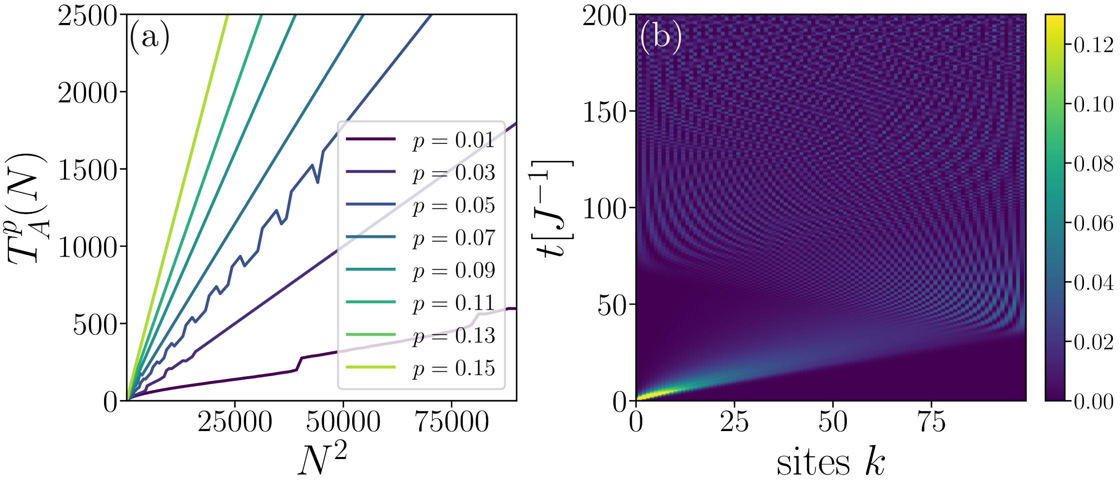

FIGURE 4.6: The algebraic long-range coupling introduces the system site to all the bath sites, albeit at a strength decaying quadratically with distance in chain geometry. For such a strong decay, the local energy density remains finite for all bath sizes. (a) The scaling of the absence time is quadratic in bath size. This scaling persists for all system sizes, as does the linear (maximal) scaling with bath size of the effective dimension of the initial state. (b) At short times, the light-cone dynamics are dominant, but the excitation soon becomes delocalized, covering the whole bath.

$$T_A^{\frac{1}{N}} \propto N. \tag{4.9}$$

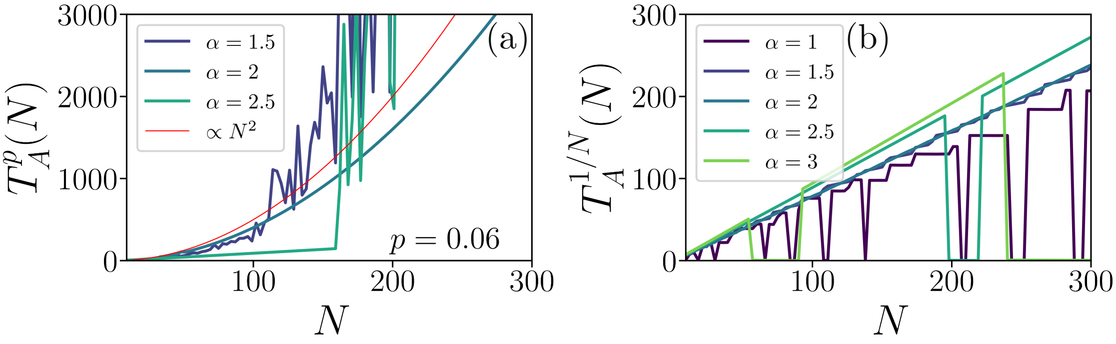

FIGURE 4.7: Using different exponents for the long-range coupling model worsens the scaling overall. (a) For $\alpha > 2$, the scaling becomes linear, while for $\alpha = \frac{3}{2}$, there is a small regime where it scales as $T_A^p(N) \propto N^{\frac{3}{2}}$, after which no consistent scaling is present. (b) The equipartition scaling is more resilient, although it breaks again when departing too far from $\alpha = 2$, plateauing in both extremes.

This is a stark qualitative difference to all other setups considered. The spectrum of the long-range coupling model with $\alpha = 2$ is quadratic, and thus models a free theory in continuous space. This case also bridges the gap between the first absence time diagnostic and the non-Markovianity measures such as the trace-distance, as described in section 2.2.2.

4.3.2.1 Different exponents

Varying the exponent α does not merely change the scaling of the recurrence time, as shown in Fig. 4.7. Even though the effective dimension of the initial state scales linearly for other α values, the first absence time scaling becomes erratic. Going further towards the local regime, $\alpha > 2$, the scaling becomes linear. It retains some nonlinear character for $2 > \alpha > 1$, which breaks down at moderate bath sizes > 100. The equipartition scaling remains linear around $\alpha = 2$, however not as clear as for the exact quadratic case. The absence time does not plateau as in the Speedwagon configuration, but the erratic behaviour makes the scaling of $T_A^p(N)$ difficult to interpret and potentially an unfitting candidate for investigating the delocalization properties of the model.

4.3.3 Continuous space ring

The quadratic spectrum of the algebraic long-range coupling model bridges the gap to space-continuous models. In general, these would necessitate the introduction of quantum field theory results or first quantization formulation, e.g. using the Gross-Pitaevskii equation. We will however not delve deep into this regime and use a single example of a particle on a ring of circumference L. The time-independent Schrödinger equation reads

$$-\frac{\hbar^2}{2m}\vec{\nabla}^2\psi = E\psi, \tag{4.10}$$

where $\hbar$ is the reduced Planck constant, m is the mass of the particle, $\vec{\nabla} = \vec{e_x}\partial x + \vec{e_y}\partial y + \vec{e_z}\partial z$ is the Nabla operator and E is the eigenenergy. With the particle confined to S^1, the differential operator is rewritten in polar coordinates and the system can be solved for its spectrum and eigenfunctions. The spectrum is quadratic,

$$E_n = \frac{2\pi^2 n^2 \hbar^2}{mL^2}, \tag{4.11}$$

with doubly-degenerate eigenfunctions

$$\psi_n(x) = \frac{1}{\sqrt{L}}\exp\left(\pm in2\pi\frac{x}{L}\right). \tag{4.12}$$

As initial state, we start with the raised cosine distribution

$$f(x;\mu,s) = \frac{1}{2s}\left(1+\cos\left(\frac{x-\mu}{s}\pi\right)\right). \tag{4.13}$$

Defined like this on the interval $[\mu - s, \mu + s]$ and zero elsewhere. This functional form makes the support of the initial wave-function independent of bath size (ring circumference L) in analogy to the discrete-space setup. We choose $\mu = 0$ and $s = 1$,

$$f(x;0,1) = \frac{1}{2}\left(1+\cos\left(\pi x\right)\right). \tag{4.14}$$

The square root of this is the initial wavefunction

$$\phi(x,t=0) = \sqrt{f(x;0,1)}. \tag{4.15}$$

The decomposition into eigenstates is given by

$$\phi(x,t=0) = \sum_{n=0}^{\infty}\frac{4L\sqrt{L}}{\pi\left(L^2-16n^2\right)}\cos\left(2\pi n\frac{1}{L}\right)\psi_n(x). \tag{4.16}$$

With this, we can now investigate the overlap of the initial state with the time-evolved initial state,

$$\begin{aligned}\int_{-\frac{L}{2}}^{\frac{L}{2}}\overline{\phi(x;t=0)}\phi(x;t)dx &= \frac{16L^3}{\pi^2}\sum_{n=0}^{\infty}\frac{\cos^2\left(2\pi n\frac{1}{L}\right)}{\left(L^2-16n^2\right)^2}\exp\left(-it\frac{2\pi^2n^2\hbar^2}{mL^2}\right)\\ &= \frac{16}{L\pi^2}\sum_{n=0}^{\infty}\frac{\cos^2\left(2\pi n\frac{1}{L}\right)}{\left(1-16\frac{n^2}{L^2}\right)^2}\exp\left(-it\frac{2\pi^2n^2\hbar^2}{mL^2}\right).\end{aligned} \tag{4.17}$$

From the spectrum we can immediately read off the macroscopic time $T_A^1(L) = T$ at which time-evolution unravels, $U(T) = U(0) = \mathbb{1}$

$$T = \frac{L^2 m}{\pi \hbar^2}.$$

This total time scales quadratically with ring circumference L. This is reflected in the scaling of the absence time, which is itself quadratic in L. Even though the prototypical example of the chain was used to motivate linear scaling of the recurrence time, the continuous counterpart of the chain features quadratic scaling, which is in line with the result for the quadratically decaying coupling. This is not fully surprising, as the second quantized tight-binding Hamiltonian of the discrete space chain does not reflect the higher-order interactions beyond s-wave scattering. For constant energy-density on shells of radius R from a point source in three dimensions, we expect interactions decaying quadratically with distance, which is exactly modelled in the long-range coupling setup of section 4.3.2. That the spectrum for the long-range coupling setup with $\alpha = 2$ is also quadratic underpins this even further.

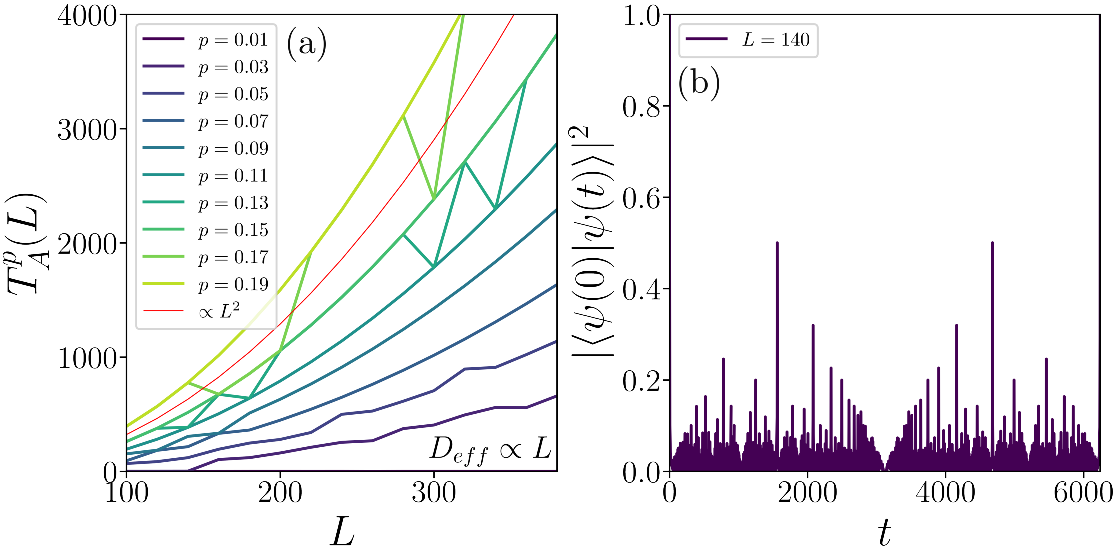

FIGURE 4.8: For the continuous space ring, the total period of the system scales quadratically with the ring circumference L. This is reflected in the absence time scaling (a), which scales quadratically throughout. In (b), the initial state fidelity is shown for times up to the total period. The inversion of dynamics at the halfway point is clearly visible.

4.3.4 General trends for the absence time scaling for modulated tunnelling-strengths

In a simple hopping model, tunnellings dictate the timescale over which traversal between sites happens. Locally slowing bath-dynamics down, such that extensions have iteratively slower transport, has the potential to keep the particle away from the system (the site $i = 0$ it originated from) for a longer time. The main problem encountered in this setting are partial reflections of the particle, which for larger and larger baths conspire to activate the threshold and halt the bath-scaling of the recurrence time completely, as is seen in the Speedwagon configuration 4.3.1. For long-range coupling models, there is a sweetspot found at quadratic decay, for which a clean quadratic scaling of $T_A^p(N)$ is observed. This is also found in the continuous space ring setup. Deviating from quadratic decay in the discrete space model yields a smooth crossover to the chain, together with the eventual departure of the linear scaling at system sizes too large, for which the returning wave-packet is not coherent enough to be detected. The long-range coupling case is special also because it allows a system size dependent activation threshold $p = \frac{1}{N}$, which mirrors the actual average value of the equipartition. For the other models, local reflections will interfere with this choice and eventually the dynamics across only the first site is sampled. This behaviour however does not remain stable for different exponents.

4.4 Absence-time distributions

This section revisits all the models for which data has been shown in the previous section. Here we will consider not the scaling of the first absence time, but instead try to understand the structure of absences arising within the orbit associated with the initial state, as explained in 2.2.3. For each set of data presented within a figure, the maximal evolution time is constant for the different system sizes, large enough to have gotten considerable statistics, such as to give meaning to both the mean absence time $\langle T_A^p(N)\rangle$ and the average recurrence time $\mathscr{T}_R^p(N)$. The number of absences and recurrences is given by $\hat{r} \gg 1$.

$$\langle T_A^p(N)\rangle = \frac{1}{\hat{r}} \sum_{w=1}^{\hat{r}} \left(T_A^p(N)\right)_w , \tag{4.18}$$

$$\mathscr{T}_R^p(N) = \frac{\left[T_R^p(N)\right]_{\hat{r}}}{\hat{r}} . \tag{4.19}$$

For the chain and the lattice, the first absence time and integer multiples thereof are prominent as accumulations point of the absence time samples gathered and shown sorted by size in Figs.4.9&4.10(b). The absence times in the two cases appear identical.

The thresholds for the lattice are (only in subfigure 4.10(b), thus the dashing) chosen as the square of the typical thresholds,

$$\tilde{p} = p^2. \tag{4.20}$$

Doing this transforms the lattice data to look exactly like the chain data. The transformation (4.20) is not coincidental. The lattice with edge-length M has the squared number of bath sites compared to the chain of length M. The equipartition occupation on the bath, which is the a priori agnostic choice for a long-time state, is M^{-2} for the square and M^{-1} for the chain. Since the square lattice is obtained by the graph Kronecker product of two chains and no interactions are present, the dynamics should share general features if fluctuation sizes are rescaled. This rescaling is then exactly the transformation (4.20). For small thresholds the first absence time is substantially larger than the mean absence time. This is in general dependent on system size, which one can see in Figs.4.9-4.12(a). The first absence time for $p = 0.1$ is shown in red, together with the mean absence time for different thresholds $0.01 \leq p \leq 0.15$. There is a crossover in system size, such that for $N < N_{crit}(p)$ we have $T_A^p(N) > \langle T_A^p(N) \rangle_A$ and for $N > N_{crit}$ the opposite relation is true. The mean absence time scales exponentially for all the models considered whose initial state effective dimension scales indefinitely. The Speedwagon setup, whilst providing exponential scaling at intermediate system sizes, plateaus and takes a more local form. The exponential scaling of the mean absence time is contextualized best by considering the average recurrence time $\mathscr{T}_R^p(N)$. Following [64], it is possible to derive an exponential scaling of the average recurrence time, $\mathscr{T}_R^p(N) \propto \exp(pD_{\text{eff}})$ using spectral properties of the Hamiltonians (which in the single particle non-disordered case are integrable). Except for the Speedwagon configuration, the scaling of the effective dimension is maximal, $D_{\text{eff}} \propto N$. In Fig. 4.9(d) the scaling collapse does suggest the functional form

$$\mathscr{T}_R^p(N) = Q(p)\, e^{pD_{\text{eff}}}, \tag{4.21}$$

where $Q(p)$ is independent of system size N. A similar scaling collapse is achieved in the lattice, see Fig. 4.10(d). Here however the distinction between the effective dimension and the graph radius becomes relevant. Even though the effective dimension scales maximally, the average recurrence time scales with the graph radius $R\,(G(N)) \propto \sqrt{N}$,

$$\mathscr{T}_R^p(N) = Q(p)\, e^{pR(G(N))}, \tag{4.22}$$

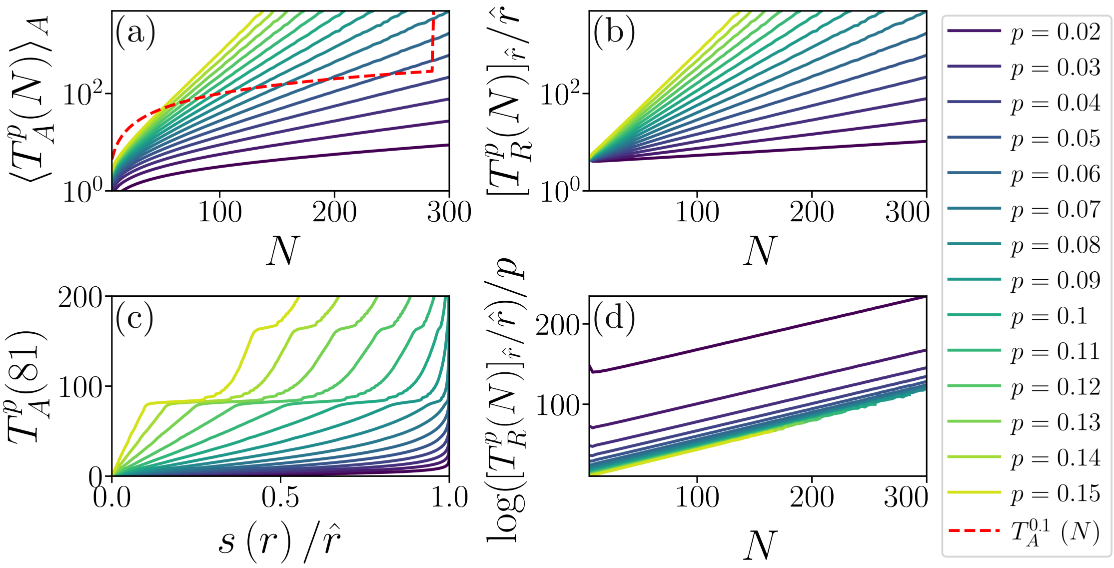

FIGURE 4.9: Statistics of the chain-bath for sizes $6 \leq N \leq 300$. (a) Average absence time scaling with bath size, $\langle T_A^p(N)\rangle$, on a logarithmic scale. The red dashed line shows the first absence time scaling for $p = 0.1$. For smaller bath sizes, the scaling of the average absence time is linear in N, changing to an exponential scaling for sufficiently big N. (b) Sample of absence times obtained up to the maximum time for the bath size 81, ordered by magnitude. Not all thresholds feature the same number of absence times, so the indices are normalized $\rho \in [0, 1]$. Even though the first absence time is linear in system size and thus $t \approx 81$ for all thresholds, for small p, most other absences are a lot smaller. As thresholds get larger, there is a clear plateau at the first absence time, and a second plateau forms at double this value. (c) Average recurrence time, using the last recurrence time found for the time evolution. The number of recurrences is large, $\hat{r} \gg 1$. The scaling is exactly exponential. (d) Scaling the data in (c) with the thresholds p leads to a scaling collapse, suggesting the functional form (4.21). This exactly retrieves the scaling found in [64].

Even though the Speedwagon configuration does not feature persistent scaling in either the mean absence nor the average recurrence time, Fig. 4.11 shows that the plateau-height scales exponentially with the threshold p,

$$\mathscr{T}_R^p(N) \propto \exp(p) \tag{4.23}$$

Given that Figs.4.9-4.12(c) support this exponential scaling, the mean absence time following a similarly universal scaling is not surprising.

4.5 Disordered on-site energies

The previous sections considered deterministic setups that modify both the graph geometry and the tunneling coefficients. Varying on-site energies has, in the deterministic case, not been met with success in finding superlinear scaling in the first absence time, so instead this section highlights results found for on-site energies randomly drawn from a

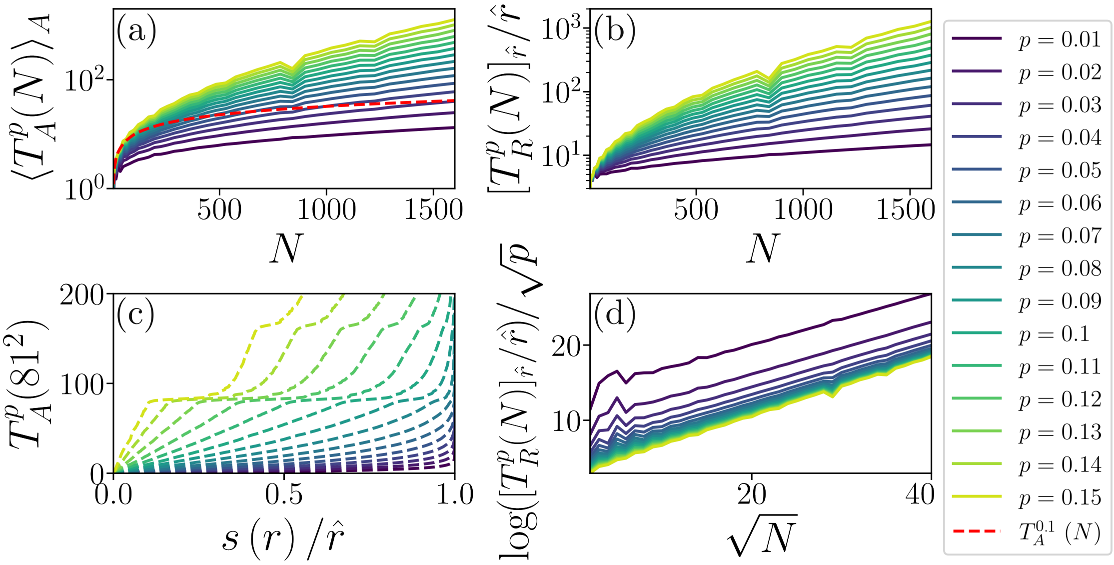

FIGURE 4.10: Statistics of the square lattice bath for sizes $2^2 \leq N \leq 40^2$. (a) Average absence time scaling with bath size, $\langle T_A^p(N) \rangle$, on a logarithmic scale. The red dashed line shows the first absence time scaling for $p = 0.1$. For smaller bath sizes, the scaling of the average absence time is linear in N, changing to an exponential scaling for sufficiently big N. (b) Sample of absence times obtained up to the maximum time for the bath size 81^2, ordered by magnitude. Instead of the typical thresholds, the thresholds here are chosen as $\tilde{p} = p^2$, indicated by the dashing. The absence times exactly follow the form found in the chain of length 81, see Fig. 4.9(b). The adjustment of the thresholds (4.20) reflects the change in bath size from the chain to the lattice. A plateau is visible at the first absence time, although for small thresholds the majority of absence times is lower. More plateaus at integer multiples emerge. (c) Average recurrence time, using the last recurrence time found for the time evolution. The number of recurrences is large, $\hat{r} \gg 1$. (d) Scaling the data in (c) with the thresholds p leads to a scaling collapse, suggesting the functional form (4.22). In contrast to the results from [64], the scaling is dictated by the graph radius $R(G(N)) \propto \sqrt{N}$ instead of the effective dimension $D_{\text{eff}} \propto N$.

probability distribution P, which is taken to be a gaussian with mean 1 and variance σ_ω. The on-site energies are independently, identically distributed (i.i.d.). We consider two cases that, in the deterministic setups, we were able to relate directly to one another. The chain and the square lattice. It is well known that the disorder will localize the eigenfunctions of the single-particle Hamiltonian in real space. This in turn limits the scaling of the effective dimension of our initial state, which measures the support of the initial state in energy eigenstates. From the earlier results, we understand that scaling effective dimension is a prerequisite for scaling absence time, so we expect the scaling of the absence time to depend on σ_ω, potentially in a nontrivial way. For $\lim_{\sigma_\omega \to 0}$ we retrieve the deterministic result, and should do so smoothly. For $\lim_{\sigma_\omega \to \infty}$ the position basis approaches the energy eigenbasis and there is no nontrivial time-evolution. The absence time does not scale at all. The results in this section highlight whether intermediate disorder strengths non-trivially interpolate between these limiting cases. In contrast to the deterministic models, disorder requires a statistical analysis of the first

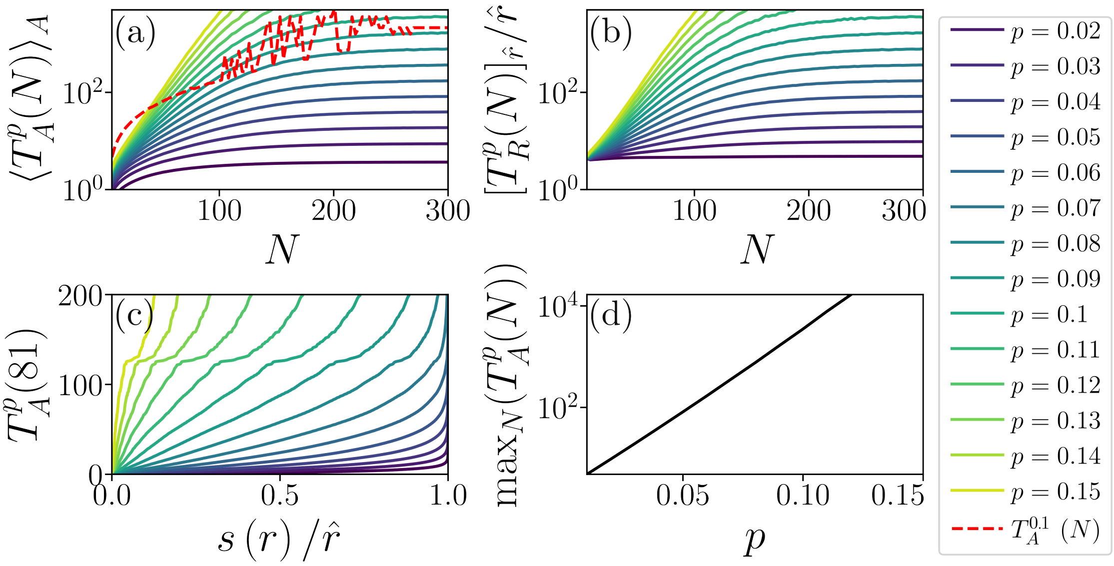

FIGURE 4.11: Statistics of the speedwagon-bath for sizes $6 \leq N \leq 300$. (a) Average absence time scaling with bath size, $\langle T_A^p(N)\rangle$, on a logarithmic scale. The red dashed line shows the first absence time scaling for $p = 0.1$. There is a clear transition from an exponential into a stagnant regime, in accordance with both the effective dimension and the first absence time. (b) Sample of absence times obtained up to the maximum time for the bath size 81, ordered by magnitude. For many thresholds the first absence time is far above the median, and a clear plateau is visible at the first absence time and double its value. (c) Average recurrence time, using the last recurrence time found for the time evolution. The number of recurrences is large, $\hat{r} \gg 1$. The behaviour is similar to the mean absence time, with a crossover from exponential to a plateau. (d) Scaling of the plateau of average recurrence times as a function of the thresholds. It is exponential, (4.23).

absence time. We write the mean first absence time here similar to the mean absence time in the deterministic models,

$$\langle T_A^p(N)\rangle_\Omega = \frac{1}{|\Omega|}\sum_{i=1}^{|\Omega|}\left[T_A^p(N)\right]_i, \tag{4.24}$$

where the subscript i refers to the i-th disorder instantiation of the Hamiltonian. Acquiring statistics of all the absences, as done above for the deterministic models, would require two averages - one over the samples and one over the different absences. We will not investigate this, but instead rely on the possibility of the disorder itself to do both of these tasks in one.

4.5.1 The chain

On the disordered chain all the aforementioned regimes, the ballistic, the localized and the intermediate one, are present, albeit not for a single threshold p. In Fig. 4.13(a), with $\sigma_\omega = 0.1$, the low thresholds $p = 0.01$ are fully local and do not scale at all

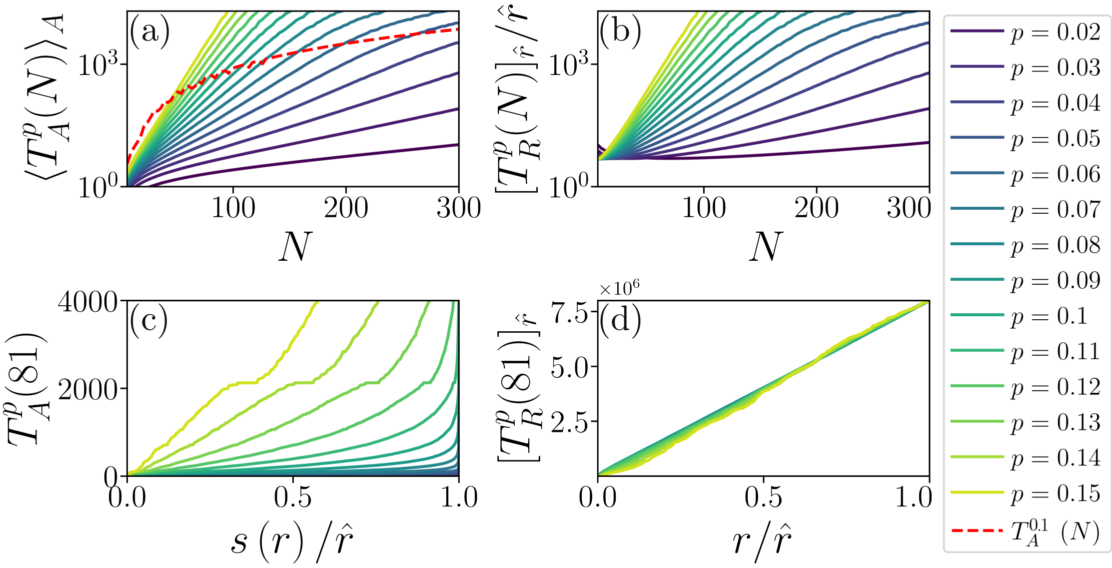

FIGURE 4.12: Statistics of the long-range coupling bath for sizes $6 \leq N \leq 300$. (a) Average absence time scaling with bath size, $\langle T_A^p(N)\rangle$, on a logarithmic scale. The red dashed line shows the first absence time scaling for $p = 0.1$. Small bath sizes feature quadratic scaling (just as the first absence time), which then goes over to exponential scaling. (b) Sample of absence times obtained up to the maximum time for the bath size 81, ordered by magnitude. The plateaus for integer multiples of the first absence time are visible, but most absence times are much smaller than this. (c) Average recurrence time, using the last recurrence time found for the time evolution. The number of recurrences is large, $\hat r \gg 1$. The intermediate exponential scaling diminishes to a quadratic one. (d) Recurrence times as they occur during the time evolution. Early times feature a lot more recurrences. This reflects that good statistics for large thresholds at larger bath sizes require longer time-evolution.

with bath size. Slightly larger p shows a reduced ballistic scaling on all bath sizes. Increasing p further shows the ballistic result up to intermediate bath sizes. Beyond this, the excitation does not only explore the full spatial range of the disordered chain, but does so very nontrivially. The mean first absence time scales exponentially with bath size. All the above is corroborated by Fig. 4.13(b), where the first absence times of the 1000 different disorder instantiations for the chain of size $N = 150$ are shown in ascending order. At $T \approx 150$, the ballistic value, a strong plateau is shown for many thresholds p. The lowest two thresholds rarely or never show absence times of this order. This is similar in the absence times analyzed in the deterministic models, but since the mean first absence time does not scale with bath size either, we conclude that w.r.t. these thresholds the dynamics are localized. Larger thresholds have increasingly smaller plateaus at the ballistic absence time, exceeding it in the majority. For Fig. 4.13(c)&(d), the same considerations are shown for $\sigma_\omega = 0.05$. Naturally, the deterministic region is a lot larger, but even here the smallest threshold is localized, and larger thresholds show exponential onset eventually. This exponential onset is a lot steeper. From the disordered case we can deduce that, with respect to the language of the absence time, localization is a quality connected to the pair (D_{eff}, p) of an initial state $|\phi\rangle$. Depending

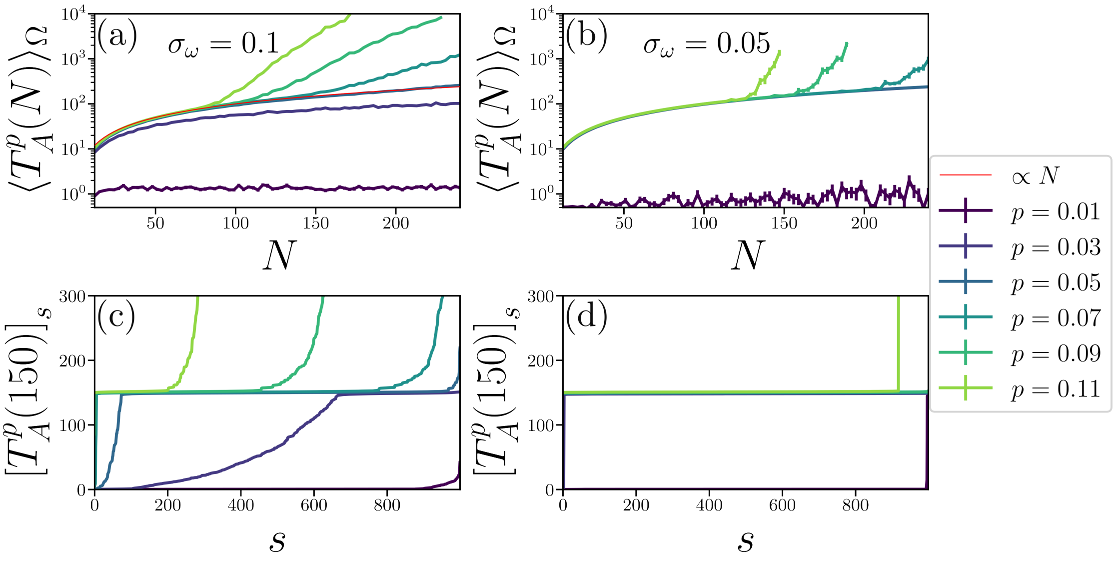

FIGURE 4.13: Absence times for chains with i.i.d. on-site energies with mean 1 and variance σ_ω. For all sizes 1000 disorder instantiations were taken and the first absence time computed. Their disorder average (4.24), is shown in (a) and (c). (a) $\sigma_\omega = 0.1$. Three regimes are visible. For very small p, the mean first absence time is smaller than in the deterministic case, signaling that the excitation does not explore the full system. For other p and at smaller system sizes, the scaling agrees with the deterministic one. For larger system sizes, some thresholds surpass the deterministic scaling and become exponential, $\propto \exp(Np)$. (b) $\sigma_\omega = 0.05$. The same three regimes are visible, although the exponential regime is not yet fully featured at the system sizes investigated. (c) $\sigma_\omega = 0.1$, $N = 150$. For small p, the absence-times are all local, as they lie below the ballistic regime. For intermediate p a large ballistic plateau is visible, that shrinks upon increasing p. (d) $\sigma_\omega = 0.05$, $N = 150$. For all except the smallest p we see strong clustering at the ballistic value. The disorder is not strong enough to overcome the ballistic features at the length-scale $\propto N = 150$.

on threshold p, we'd consider a state $|\phi\rangle$ localized or not, expanding the conventional picture of localization which is dominated by the effective dimension D_{eff}.

4.5.2 The square

For the square, we see exponential scaling in the mean first absence time from Fig. 4.14(a)&(c). In Fig. 4.14(a), the onset of the ballistic $\propto \sqrt{N}$ scaling is still visible for smaller squares, indicating that the exponential scaling does not immediately take over for arbitrarily small, nonzero σ_ω. In Fig. 4.14(c), this small onset is further suppressed and resembles scaling of the mean absence time of the deterministic lattice in Fig. 4.10. Opposed to the disordered chain, the ballistic regime is less threshold-dependent. The exponential scaling is also present for the median first absence time (not shown). Drawing parallels to the results for the deterministic lattice in 4.10 reveals a lot of conceptual overlap. The mean absence time in the deterministic model corresponds to the mean first absence time in the disordered model, at least in a functional form. For sufficiently strong

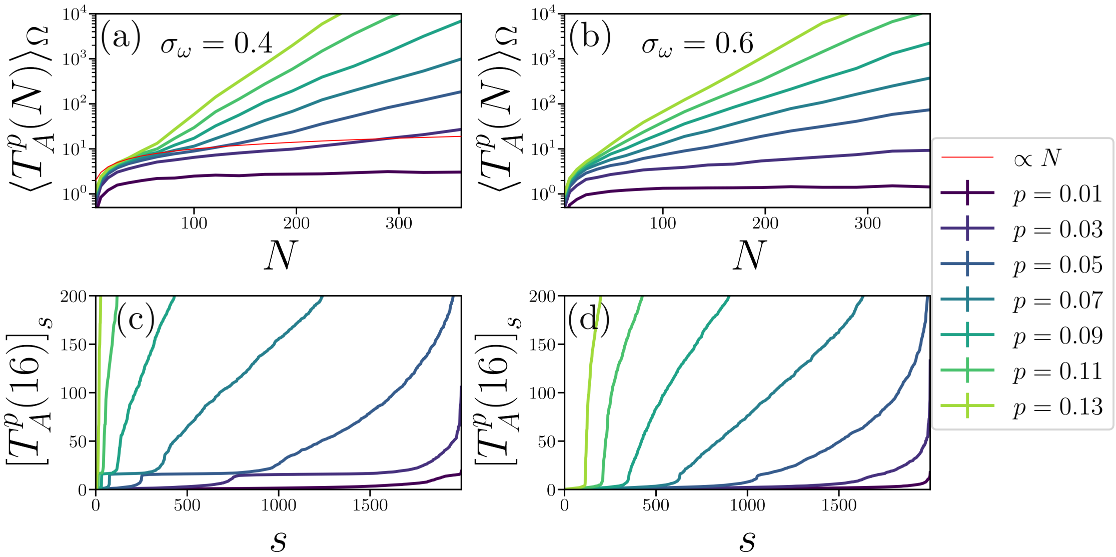

FIGURE 4.14: Absence times for square lattices with i.i.d. on-site energies with mean 1 and variance σ_ω. For lattices between sizes 2×2 and 20×20, 2000 disorder instantiations were taken and the first absence time computed. (a) Mean first absence time (4.24) for $\sigma_\omega = 0.4$. The scaling starts as $\sqrt{N}$, similar to the deterministic lattice, but takes an exponential form $\propto \exp(Np)$. (b) $\sigma_\omega = 0.4$, $N = 16^2$. Despite the average (and the median) first absence time scaling exponentially, there is a clustering of first absence times around the ballistic result. (c) $\sigma_\omega = 0.6$. The initial subexponential regime is smaller, while the exponential regime scales slightly less strong. (d) $\sigma_\omega = 0.6$, $N = 16^2$. No clustering is visible at all. The ballistic features of the model have vanished even on the level of the first absence time.

disorder, the spatial structure of the lattice loses its dominance in determining the initial behaviour of the absence time, and instead the spectral form of the disorder takes over, bridging the gap between $\langle T_A^p(N)\rangle_\Omega$ and $\langle T_A^p(N)\rangle_A$. This is further corroborated when we arrange the first absence times of the disordered model in the same ascending order as the absence times of the deterministic model, seen in Fig. 4.14(b)&(d). For the disordered model, the different first absence times stand in relation to one another only through the impact of the disorder and the underlying spatial structure. The absence times shown in Fig. 4.14(b)&(d) do not belong to the same orbit, but are the first absence times of different disorder instantiations on a lattice of fixed size 16×16. The structure is understood from the zero disorder limit, $\sigma_\omega = 0$. In such a case, the different instantiations are the same and we get a bunch of horizontal lines at a height $\propto \sqrt{N}$. For sufficiently weak disorder, this clustering absence time is still observed, see Fig. 4.14(b), but eventually vanishes for increasing disorder strength. The difference to the deterministic model is clear from the missing clustering absence times at multiples of the lattice radius, $\sqrt{N}$. This indicates that the disorder is strong enough to (on average) override the ballistic dynamics into diffusive ones on length-scales smaller than $4\sqrt{N}$. As such, we expect to recover the second plateau both for smaller σ_ω and smaller N. From this in turn it is clear that, when we are only concerned with the first

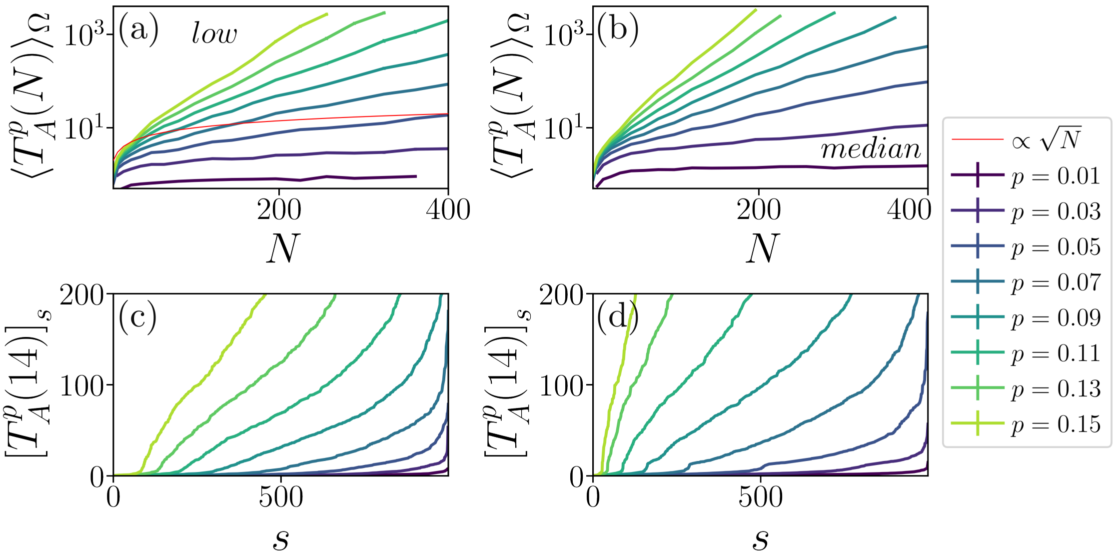

FIGURE 4.15: Absence times for square lattices with i.i.d. on-site energies with mean 1 and variance $\sigma_\omega = 0.6$. In contrast to Fig. 4.14, where the particle starts out always in the same corner, the particle is placed always on the site with the lowest (a)&(c) or the median (b)&(d) on-site energy. For lattices between sizes 2×2 and 12×12, 500 disorder instantiations were taken, for 13×13 up to 20×20, 1000 disorder instantations were taken. The disorder average of their first absence times, (4.24), is shown in (a) and (b). For both cases (a) and (b), the scaling at sufficiently large sizes is exponential, although placing the particle systematically on the site with the lowest ω_i suppresses the scaling. The ordered first absence times for the different disorder instantiations show no stark qualitative difference between (c) (lowest) and (d) (median).

absence time, the necessary disorder for superlinear (and as these results suggest even exponential) scaling decays as N grows. When implementing this care should be taken to have physical arguments for why this does not clash with the notion of extensibility of the bath, as for every change in system size the whole bath, even the smaller subgraph denoting the bath of a smaller size, is changed. This is similar to the variable thresholds used in the long-range coupling models in section 4.3.2. Even there it might be argued that the whole bath experiences a change due to additional long-range couplings being introduced. The difference there is that, due to not using the Kac normalization, the smaller bath is still present as a subgraph in the total bath.

4.5.3 Spectral sampling

In the deterministic models considered for different graphs and tunnelling-strengths, the initial state chosen as a localized particle on one (fixed) site (site 0, the **system**) has a trivial extension to larger system sizes. In probabilistic models, the choice of initial site emerges as its own hyperparameter, both regarding system size scaling and even regarding the disorder averaging (**??**) for a fixed system size. When sampling the different disorder instantiations for the data shown in Fig. 4.14, the initial particle is always placed onto the site in one corner of the square. Depending on whether the random on-site energy on this site is high or low, this state has support on different parts of the spectrum. Averaging over all the disorder instantiations in this way averages over the spectrum of the random Hamiltonians (which, despite being different for each instantiation, have universal properties as random matrices). In order to investigate whether this averaging procedure is the cause of the self-averaging behaviour of the mean first absence time as shown in Fig. 4.14, we redo the setup, but this time place the initial particle on a site with a specific quality. In one case, the particle is always put on the site with the lowest on-site energy. In the other case, the particle is put on the site with the median on-site energy. The results for these setups are shown in Fig. 4.15. For both cases we recover exponential scaling of the mean first absence time, although it is a lot weaker when the particle is on the site with the lowest energy. The ordered first absence times show a similar behaviour, but as in Fig. 4.14(d), there is no pronounced plateau at the lattice radius. From this we conclude that the scaling itself is independent of the accidental spectral sampling of the particle sitting at different points in the spectrum, but rather from the overall spectral sampling by the different disorder instantiations. Finite size effects in random matrices manifest predominantly at the edges of the spectrum, so the weakening of the scaling at the bottom of the spectrum is expected. That the exponential scaling itself persists is however interesting.

4.6 Conclusion

The single-particle case is an instructive way to understand the mechanisms at play when faced with the question of relocalization of information in a quantum system. The different witnesses for relocalization are in some ways interchangeable and the problem can be tackled head-on. Via the studied setups we have shown that local geometry, spatial extent and partial reflections are the dominant contributors to different scalings of the first absence time. Furthermore, we confirmed that the persistent scaling of the effective dimension is a necessary criterion for persistent scaling of the first absence time, as shown by the Speedwagon construction. It comes as a surprise however, that it is not a sufficient criterion, which in turn can be seen in the algebraic construction, even in a local setup. Changing over to the absence or recurrence time statistics, results obtained in the literature via spectral considerations have been shown to hold in our setups and unify their behaviour, resulting in a persistent exponential scaling with the threshold p and the effective dimension D_{eff}. The maximal persistent nonlinear scaling was found in the algebraic long-range model, where a quadratic scaling with system size was observed. Parallels to the continuous space free theory highlighted the difference to the discrete space setup, which originally served as our baseline for suspecting linear scaling in bath size. Introducing disorder into certain setups revealed that the spectral results, obtained in the clean systems only for the full absence/recurrence time statistics, appear already in the first absence time by virtue of self-averaging. It seems promising to conclude that the spectral nature of the mean first absence time in disordered systems washes out the geometry dependent behaviour of the first absence time, bridging the gap immediately to the results found via thermalization arguments. We have ruled out one mechanism of self-averaging by forcing the particle (and with it the wavefunction) into different parts of the spectrum.

4.7 Outlook

Two restrictions were set for the single-particle setup that, if lifted, could provide the basis for ongoing investigations. The first of which was the requirement that the extension of the baths works in such a way that small baths are marginals of bigger baths. This way, one could genuinely think of extending a bath in a way of appending more sites without changing the local structure of the already present bath. This disabled Kac normalization and for example restricted the long-range coupling model from going into regimes where the unnormalized local energy density diverges in the thermodynamic limit. This is easily fixed, although the fundamental motivation of bath size scaling is compromised. Statistics at fixed bath sizes are still available, but as has been shown, they can already be inferred via spectral considerations without attention to the microscopic details of the Hamiltonian at hand. The second restriction concerns the time-independence of the Hamiltonian. A non-periodic drive trivializes the problem, as the system can, after injecting the excitation into the bath, be decoupled and recurrence suppressed forever. For periodic drives, the problem extends in complexity and this is a viable route for further investigations. This might be interesting to combine with experimental setups that motivate such a procedure, possibly something connected with gate-based quantum computing techniques. As a potential first step, it might prove useful to investigate further the disordered case that was lightly touched upon for two geometries. It would be interesting to see whether the calculation of both averages, one over the different disorder instantiations, one over the later occurring absences within the same orbit, lead to the same result. Acquiring the statistics for the disordered square is time consuming due to the exponential scaling of the first absence time, which is the main difficulty in this analysis. The results found already indicate that the spectral behaviour is retrieved directly.

Die Neugier ist die mächtigste Antriebskraft im Universum, weil sie die beiden größten Bremskräfte im Universum überwinden kann: die Vernunft und die Angst.

Walter Moers, Die Stadt der Träumenden Bücher

5

Recurrence dynamics in many-body quantum systems

In this chapter we will expand what has been investigated in the single-particle chapter 4 to the many-body setup. This comes with numerical and theoretical opportunities. On the numerical side the Hilbert-space scaling is superlinear in the system size. Whilst this seems beneficial on the level the scaling of the effective dimension, the computational resources prohibit us from investigating large system sizes. Regarding the theory, in the many-body system there are many more quantities whose recurrence can be investigated. Not all of those will show relevant scaling in the recurrence and absence time. We will focus on the mutual information and its recurrence. The mutual information is a relevant resource for quantum computation, as the sharing and manipulation of information between qubits is the basis of any computing algorithm. In conjunction, this delocalized information can straightforwardly be relocalized by means of a specific measurement protocol. This way, even if recurrence happens to be exponentially far away, the information can be retrieved by means of a protocol. The scrambled information is delocalized, but not lost.

5.1 Setup

The many-body case changes the bath setup from that of the non-interacting/single-particle case in two important ways. First, we can break the quasiparticle picture by including strong interactions without involved schemes for altering the tunnelling or on-site terms. Second, the Hilbert space dimension of a many-body system scales superlinearly with the system size. From the single-particle results in chapter 4, we know that superlinear scaling of the effective dimension D_{eff} is not a sufficient criterion for superlinear absence time scaling, but it is necessary. The many-body system we consider is the spin-$\frac{1}{2}$ XXZ model. The Hamiltonian of this model is written as

$$H_{XXZ} = J \sum_{i=1}^{N-1} \left(X_i X_{i+1} + Y_i Y_{i+1} + \Delta Z_i Z_{i+1} \right), \tag{5.1}$$

where X, Y, and Z are the Pauli matrices, the interaction strength is given by Δ and J is taken to be the unit of energy. This Hamiltonian conserves magnetization in the Z direction, which mirrors the particle number conservation of the single-particle setup. Spatial magnetization dynamics are enabled via the hopping term J, whilst magnetization dependent dephasing is related to Δ. For $\Delta = 0$, no dephasing is present and the system consists of non-interacting spins which in certain geometries can be mapped to spinless Fermions using a Jordan-Wigner transformation. For $J = 0$, the model does not feature magnetization transport and only dephasing occurs. As an additional benefit, the Hamiltonian is diagonal in the computational basis for $J = 0$, even though the closed form solution for the eigenenergies is difficult to gauge. The integrability of the many-body model is not of central importance. This might come surprising, especially considering results by [64] and general thermalization work. A simple adjustment to the spin-$\frac{1}{2}$ XXZ chain can be made in order to induce non-integrability, defined by the level spacing statistics of the model displaying Wigner-Dyson statistics. Introducing a local Z_k term on a single site k that is not on the boundary creates Wigner-Dyson statistics [37]. This local impurity does not change the scaling of the first absence time, which is strongly tied to space-resolved dynamics, as opposed to spectral considerations.

As explained in section 2.3.4, using the entanglement entropy between system and bath, which in itself measures separability of the system from the bath, does not reflect what we are out to investigate. Along an orbit of the time-evolution, there may be different states $|\psi_\sigma\rangle$ that almost decompose into pure states on system and bath, although the information injected via the system has not relocalized in it at all. To make this unambiguous, we entangle our system with a reference spin, labelled R throughout this chapter, and use the entanglement of system-reference as our measure of having relocalized the initial information. The initial state between the probe and the reference is a

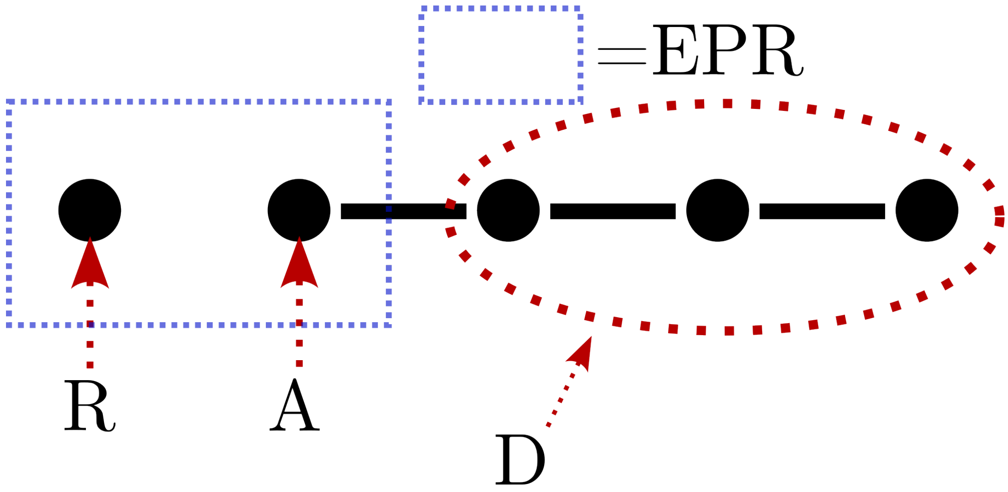

FIGURE 5.1: Sketch of the many-body setup. The probe spin A is initialized in an Bell (or EPR) pair with a reference spin R, which otherwise is not involved in the dynamics. The bath D is connected to the probe spin and the dynamics are governed by the XXZ Hamiltonian (5.1).

Bell state,

$$|\psi_{RA}^{init}\rangle = \frac{1}{\sqrt{2}}\left(|0\rangle|0\rangle + |1\rangle|1\rangle\right). \tag{5.2}$$

Unless specified otherwise, the state (5.2) is always the initial state of the subsystem of reference and probe. The reference R is not connected to the rest of the setup and therefore does not undergo time-evolution. This setup is sketched in Fig. 5.1. The mutual information between the reference R and the probe A determines the amount of localization of the initial information on the probe. The reference can also be used to track the location of the information in the many-body bath by virtue of the mutual information $I(R; d)$, where d is a collection of sites in the bath, see 2.3.4. As opposed to the single-particle regime, the bath in the many-body setup does not have an innate unique configuration. Pointing back to our efforts to make the bath size scaling faithful, the initial states of the baths should be chosen in a way that makes their extension to or marginalization from larger baths well-defined. For baths in non-stationary initial states with constant magnetization density, we consider the Néel state, given by alternating spin-orientations in the z-direction, e,g. $|0101010\rangle$, since it does not inherently separate the bath into different spatial domains. On a computational level this is beneficial since it locks the dynamics into a sector of constant magnetization, reducing the Hilbert space scaling to a slower growing exponential. One can also initialize the bath into a stationary state, i.e. an energy eigenstate, typically the ground state. The latter is equivalent to a local quench in the coupling between A and sites in D, with the energy band in which the initial state lies being of a width of order J_{01}. Starting in the Néel state amounts to a global quench (if the Néel state is not an eigenstate) and the initial state is spread over a much bigger band of energies. In terms of the effective dimension, superlinear scaling with the system size N is not expected for the local quenches, in contrast to the global quenches. In chapter 4 we have seen that also a linear effective dimension can result in superlinear absence time scaling, but the potential benefit of the many-body regime has to be found elsewhere in this case. The early-time behaviour of the initial information on A through the bath after a local quench is seen in Fig. 5.2. Here the initial state on the bath is the lowest energy eigenstate in the 2-particle sector of the Hamiltonian (5.1). For weak interaction, $\Delta = 0.1$ in Fig. 5.2(a), the information strongly relocalizes back onto A in a time $\propto N$ and integer multiples thereof, a clear indication of ballistic, weakly dispersive propagation. For strong interaction, $\Delta = 1$ in Fig. 5.2(c), this behaviour is strongly suppressed, suggesting that even the local quench might produce superlinear scaling in the absence time. Looking at the probability distribution function of the recurrences of $I(R;A)$, we find that for increasing system size it becomes log-normal distributed, as is seen in Fig. 5.2(b)&(d). This behaviour emerges for weak and strong interactions, and is also seen for global quenches from the bath in the Néel state.

As seen in Fig. 5.3, the ballistic propagation is still visible at weak interactions, getting smeared out for increasing interaction strength. This is quantified in Fig. 5.4, where the absence time scales linearly for weak interactions. Strong interactions on the other hand are not as simply explained as hoped. The absence time quickly grows very large for increasing bath size. The scaling is superlinear, but at the same time not clearly dictated by a functional form. The raggedness makes interpretability difficult, with larger bath sizes not featuring absence times that lie within the regions expected from extrapolating the results from smaller sizes. We can confidently say that absence times are very large very quickly. However, the scaling is unclear. This might mean that recurrence in the sense defined by us might not be a useful quantity. Maybe the mutual information is not suitable to such an investigation. Maybe the absence time is not a useful concept.

5.2 Extraction of information

The benefit of the closed system quantum treatment is the fact that whilst the information can become delocalized, it will never vanish. With the aim of pushing the recurrence scaling as far as possible, a quantity should be chosen that does not undergo macroscopic recurrence in the local regime but still retains some meaningful interpretability on a physical level. Before recurrence is found, we expect the local information to be distributed amongst the participating degrees of freedom. This distribution is the main investigation of research into quantum information scrambling. While thermalization describes how a local region loses its information, scrambling extends this to describe where this information is lost to in the system [38, 73, 115, 116]. As such, scrambling is strongly

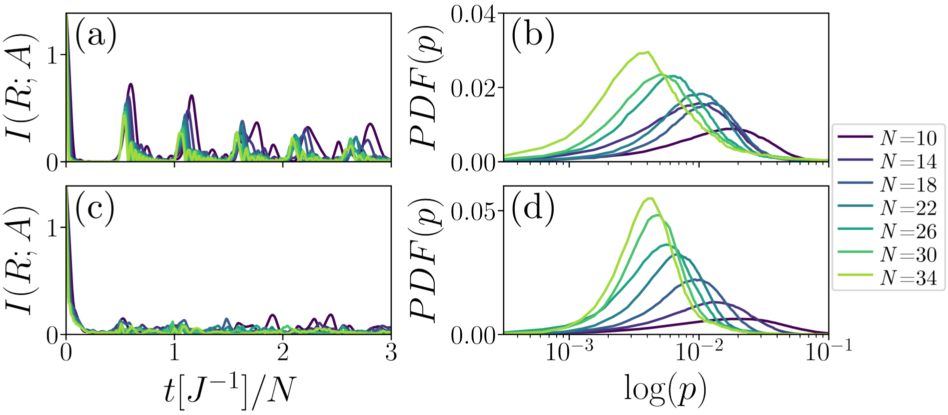

FIGURE 5.2: Instructive behaviour of the mutual information $I(R;A)$ under dynamics and an investigation on the number of recurrences in $I(R;A)$ over a long time as a function of threshold p. The initial state of the bath is the lowest energy eigenstate of the 2-particle sector of the bath Hamiltonian and the dynamics are calculated via exact diagonalization in the appropriate magnetization sectors. Reference and probe are set up in the Bell pair as in (5.2). Mutual information dynamics for different system sizes with $\Delta = 0.1$ (a) and $\Delta = 1$ (c) show that the strong ballistics from the non-interacting regime survive for weak interaction and get more and more suppressed for strong interaction. For both weak (b) and strong (d) interactions, for increasing system sizes the probability distribution functions of recurrences of $I(R;A)$ converges to the log-normal distribution w.r.t. thresholds p.

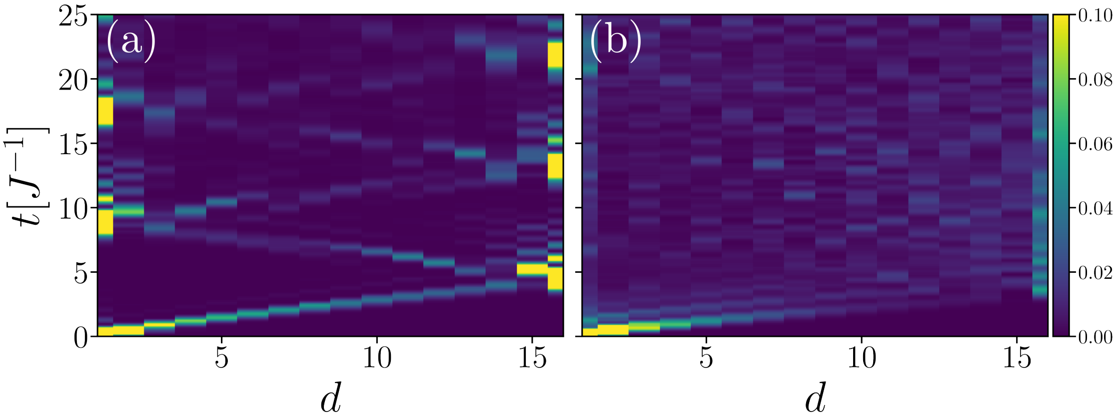

FIGURE 5.3: Dynamics of the mutual information $I(R;d)$ between the reference site R and individual bath-sites d. The initial state of the bath is the Néel state, whereas probe and reference are in a Bell pair as (5.2). The dynamics are calculated via exact diagonalization in the appropriate magnetization sectors. (a) Weak interactions $\Delta = 0.1$ show the non-dispersive propagation clearly, with bunching at the edges of the chain. This bunching is still present in the strongly interacting bath $\Delta = 1$ (b), even though the interactions successfully spread the information in the whole bath.

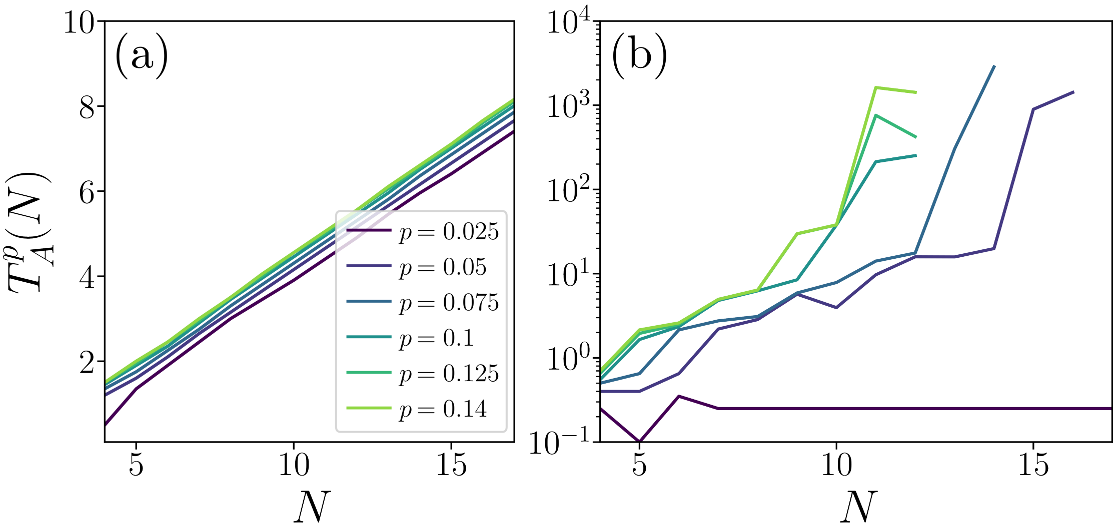

FIGURE 5.4: Absence time scaling with system size for different thresholds p in the XXZ model. The initial state of the system is $|\Psi\rangle = |\psi_{RA}^{init}\rangle\,|\text{Neel}\rangle$, where $|\psi_{RA}^{init}\rangle$ is given in (5.2). Dynamics are calculated via exact diagonalization in the appropriate magnetization sectors. (a) $\Delta = 0.1$. For weak interaction we recover the single-particle ballistic behaviour in $T_A^p(N)$. The effective dimension of the initial state scales linearly with the bath size. (b) $\Delta = 1$. Strong interaction changes the absence time scaling. For low p the local recurrences are stronger than in the weakly interacting model. For higher p this changes drastically and the absence time shows exponential scaling in bath size. This scaling is very ragged, and for higher system sizes data-points were not able to be obtained and did not occur on scales as expected from extrapolation of the previous data.

connected with the observation of light-cones via which delocalization is measured. For recurrence the light-cones are of no relevance, instead we consider the behaviour of the relocalization to the local degrees of freedom, which by nature are confined within the light-cones. Distribution of information as investigated by scrambling is highly relevant in the context of quantum information theory. Imagining the general case of several local readouts within a quantum system that want to share information, scrambling dynamics can generate overlap between these disjoint readouts, enabling sophisticated protocols that relocalize the information at any of them [51, 52, 117].

5.2.1 Teleportation protocol

Here we adapt the mechanisms of the information-readout described in [52] and expanded upon in the instructional review of Xu and Swingle [73] to our model. Consider a system of N qubits, the first of which we denote as the probe A, and the remaining $N-1$ as the bath D. The probe is the location of the initial information held by Alice, which by means of some evolution $U(t)$ is delocalized among the probe and the bath. As such,

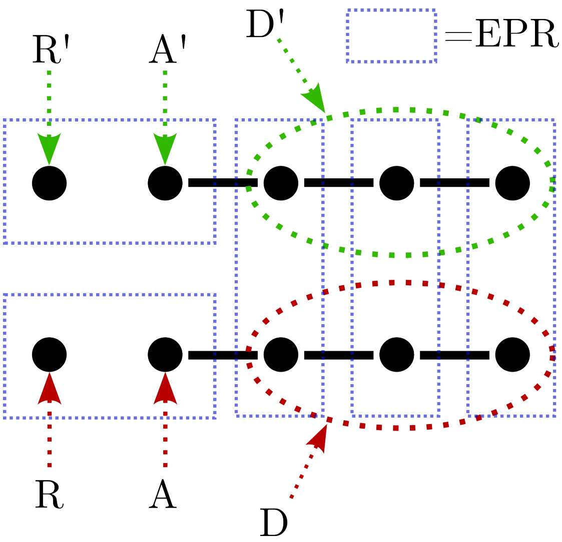

FIGURE 5.5: The extended setup in the many-body case for enabling information teleportation. The unprimed sites R, A and D constitute the original system (red). R is the reference qubit that is prepared in an EPR-pair with the probe A, whereas D is the bath. Each site in the bath D is prepared in an EPR-pair with its partner site in another bath, D'. The primed reference R' and probe A' are also in an EPR-pair. Apart from initially prepared entanglement, physical connectivity is marked by solid black lines. Thus, both R and R' are unaffected by time-evolution, and the evolution on $A \cup D$ is separable from the evolution on $A' \cup D'$. This setup is called teleportation because despite this lack of information transfer due to dynamics it enables transfer of information between $R \cup A$ to $R \cup R'$.

the initial state is a product state between A and D

$$\rho = \rho_A \otimes \rho_D. \tag{5.3}$$

One approach might be to track the entanglement between A and D, but this essentially only tracks the separability of the state without assessing whether the original information returned to A. The setup is expanded by introducing a reference qubit R, that is not part of any non-trivial time-evolution, but is initially set up into a maximally entangled state with A. For qubits, we chose one of the EPR-pairs as the initial state on $R \cup A$

$$|\psi_{RA}\rangle = \frac{1}{\sqrt{2}} \left(|0\rangle|0\rangle + |1\rangle|1\rangle \right). \tag{5.4}$$

The mutual information $I(R, A)$ can resolve whether the information initialized on A is still there. Starting the system at $t = 0$ in the state

$$|\Psi\rangle = |\psi_{RA}\rangle \, |\phi\rangle, \tag{5.5}$$

where $|\psi_{RA}\rangle$ is an EPR-pair as in (5.4), we obtain $I(R, A) = 2\log(2)$. During time-evolution, we can track the information throughout regions Q in the system by calculating $I(R, Q)$. This leads back into being able to observe light-cones of information propagation. In any case, the mutual information $I(R, A)$ becomes the quantity of interest in our many-body setup. The information initially held by Alice we would like to transfer to Bob, without giving Bob access to the whole of the N sites, as the protocol for recovery could then simply be the unravelling of the evolution by $U^\dagger$ and measuring at A itself. How to achieve this is shown in Fig. 5.5. Instead, a copy of the setup is produced. An additional $N+1$ qubits, the first two of which are the reference R', the site on which we want to localize the information for Bob, A', and the remaining $N-1$, called D' (referred to as memory in [73]). Each qubit in D is prepared in an EPR-pair with its copy in D'. The initial state on the bath D is thus the infinite temperature state, purified by including the primed bath D'. The initial state of both baths together is written as

$$\psi_{DD'} = \bigotimes_{k<N} |EPR\rangle_{kk'}. \tag{5.6}$$

Reference and probe qubits, R and A, are prepared as (5.4), just as the primed qubits. The primed setup is to be understood similar to ancillary qubits used for enabling protocols in quantum information theory. The original and the primed setup dynamics are fully independent. Due to monogamy, this setup leaves no room for additional entanglement. At the same time, the dynamics will entangle system RA with bath D and similar for the primed qubits. The protocol now has the following steps, assuming the Hamiltonian is real (see Fig. 5.5b)):

1. Evolve the original setup under $U(t) = \exp(-iHt)$ and the primed setup under $U^\dagger(t)$.
2. After time t, project the reduced state on DD' back onto the initial state on DD'.
3. Measure the mutual information between RR'.

The first part of the protocol is time-evolution in the initial setup. The primed (or decoding) setup is evolving 'backwards in time', which for real Hamiltonians is equivalent to changing signs of all energies. Projecting the DD' state at time t back to its initial state (5.6) breaks all entanglement to R, A, R' and A'. A mutual information measurement now reveals that the system and its copy, RA and $R'A'$, are entangled. Following the protocol as described will entangle R and R', and also A and A'. Instead of the last step being a mutual information measurement, one can also project RR' (or AA') into an EPR pair. The success probability of going through the whole protocol and ending up with an EPR pair between RR' is lower bounded by the squared dimension of the Hilbert-space of site A, $P_{\text{success}} \geq \frac{1}{d_A^2}$ [52]. In this form, the teleportation protocol makes use of scrambling dynamics, allowing us to transfer the state to the new copied system via the "bath" atoms. In this sense, while mutual information shows us how the information is distributed, the teleportation protocol also provides us a mechanism to extract the information from the bath degrees of freedom. This brings us full circle, from starting out with systems we wish to fully distribute the information as long as possible among the bath degrees of freedom, just as we would expect an open system to behave. At the same time, the unitarity of the dynamics allows undoing this distribution and relocalizes the information.

5.2.2 “Weighing” the bath by measuring magnetization

Teleportation is not the only way of deciding on the initial information input localized on the probe A. For the many-body model we investigate a XXZ spin-$\frac{1}{2}$ model in chapter 5. The procedure to extract the initial information in A is presented here in view of this model. The total magnetization $\langle S^z \rangle = \sum_{i\in G(N)} \langle S^z_i \rangle$ of an XXZ model is conserved. With an initial product structure between bath and probe, where both are written in eigenstates of S^z, we can split $\langle S^z \rangle = \langle S^z_A \rangle + \langle S^z_D \rangle$, and via repeated projective measurements on the bath D we can deduce the initial magnetization on A. This idea works for any quantity conserved in this way by the total dynamics. The probe site A can host at most a single quantum of magnetization. Since the full magnetization is conserved, the magnetization of the bath can fluctuate by ±1. Measuring the collective magnetization of the bath projects it into one of three subspaces with different magnetizations, $M_D \in \{M^0_D, M^0_D - 1, M^0_D + 1\}$, where M_D denotes the magnetization of the bath after the projection and M^0_D the initial magnetization of the bath. Each of these results is associated with its own probability. If we set up the initial state of the reference and probe as

$$|\psi_{RA}\rangle = \frac{1}{\sqrt{a^2 + b^2}} \left(a|11\rangle + b|00\rangle \right), \tag{5.7}$$

we can repeat projective measurements until a conclusive measurement, $M_D = M^0_D \pm 1$, is made. The probabilities for these turns out as

$$\begin{aligned} \lim_{n\to\infty} &= P^n_1 = \frac{a^2}{a^2 + b^2}, \\ \lim_{n\to\infty} &= P^n_0 = \frac{b^2}{a^2 + b^2}. \end{aligned} \tag{5.8}$$

This result shows that, exploiting a conserved quantum number (the magnetization) enables experimental setups in which the initial amplitudes of the system can be evaluated via the bath, irrespective of the nature of dynamics occurring in the bath, as long as they conserve the quantum number. For finite repetitions n, the growth of $P^n_{0,1}$ is highly dependent on the internal dynamics and convergence towards (5.8) is not symmetric, i.e. $P^n_0/P^n_1 \neq$ const. If the bath is in a state $|\psi^0_D\rangle$ with definite magnetization M^0_D, the

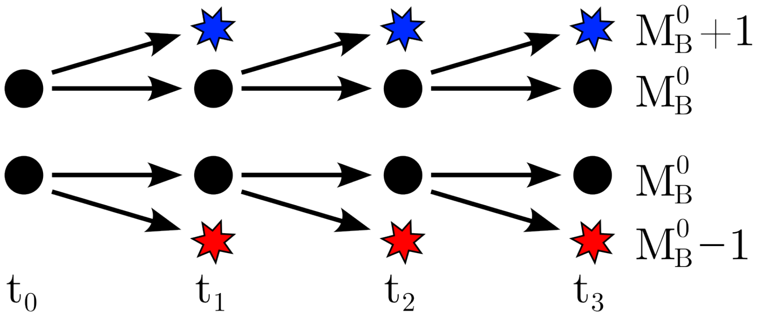

FIGURE 5.6: Weighing the chain at different times t_i with $i \in \mathbb{N}$. The limiting probabilities after infinite time and as many measurements as necessary to get a conclusive result are given by (5.8). For a finite number q of measurements, the probabilities for the different outcomes can be found by truncating the sketch after t_q and sum the probabilities of all the different terminal measurements. All the red (blue) stars for $t \leq t_q$ denote P_0^q (P_1^q), and the two black dots at t_q denotes $1 - P_0^q - P_1^q$, the probability of the measurement being not yet conclusive.

dynamics of the full state $|\Psi\rangle = |\psi_{RA}\rangle\, |\psi_D^0\rangle$ separate,

$$|\Psi(t)\rangle = \frac{1}{\sqrt{a^2+b^2}} \left(|1\rangle|\psi_{\text{up}}(t)\rangle + |0\rangle|\psi_{\text{down}}(t)\rangle\right). \tag{5.9}$$

The projection of $\text{Tr}_A\left(|\psi_{\text{up}}(t)\rangle\right)$ into the different magnetization sectors can only result in $\{M_D^0, M_D^0+1\}$, whereas the projection for $\text{Tr}_A\left(|\psi_{\text{down}}(t)\rangle\right)$ can only produce $\{M_D^0, M_D^0 - 1\}$. That the conclusive results originate from disjoint dynamics illustrates the simple shape of the result in (5.8). Fig. 5.6 illustrates a sketch of the previously said. The top and bottom row are the disjoint dynamics, which at different times t_i with $i \in \mathbb{N}$ are subject to the projective measurement. Conclusive results are found when the projection leads to $M_D^0 \pm 1$ (the red and blue stars). Inconclusive results continue the monitoring at later times.

5.3 Weighing the chain

Here we show and discuss the numerical results following up the ideas laid out in section 5.2. Fig. 5.6 shows the possible avenues the projective measurement on the bath can achieve. With the initial state on RA being a Bell-pair like (5.2), there are two disjoint dynamics of the form (5.9). The projective measurement can either be indecisive and return the original magnetization M_D^0 of the bath or it is conclusive and returns $M_D^0 \pm 1$, at which point subsequent measurements will either be inconclusive or return the same conclusive result. The statistics on repeatedly setting up the same initial state and performing this measurement sequence samples the probabilities for the different outcomes and we can calculate the cumulative distribution function (CDF) for the measurement

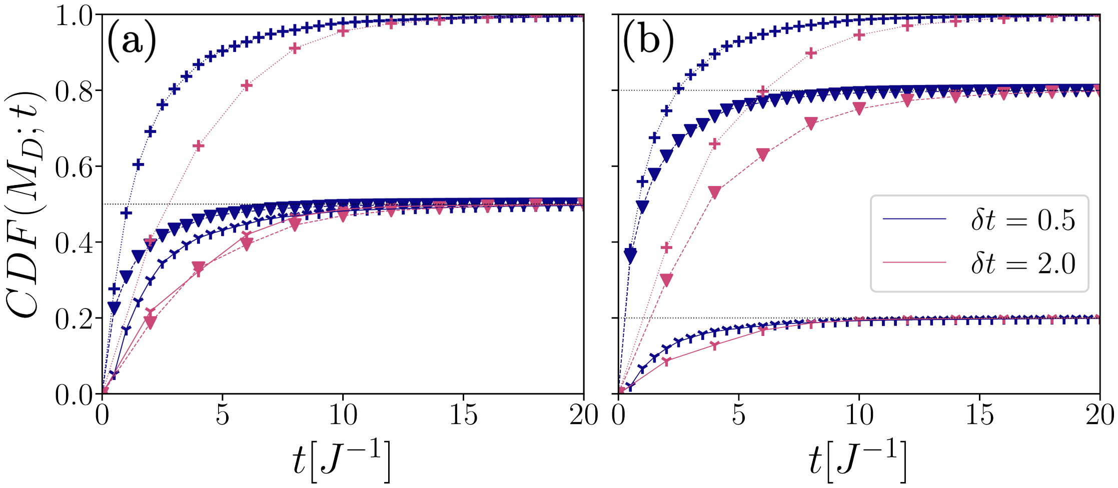

FIGURE 5.7: Weighing the bath in order to infer the initial state of the probe. Over a series of projective measurements at times separated by δt, the cumulative probability function (CDF) for each measurement outcome can be deduced. The bath initial state is the Néel state $|0101010101\rangle$, reference and probe are in a Bell state (5.2) and the interaction is strong $\Delta = 1$. Dynamics are calculated via exact diagonalization. Different relaxations to the limiting values are explained by different dynamics in the two sectors as explained in the text. (a) For $a = b$, the limiting values (5.8) are equal, 0.5. The CDFs for $\{M_D^0 - 1, M_D^0 + 1\}$ at measurement times are given by the caltrops and triangles, respectively, and the data between the measurement times are connected by lines. $1 - CDF(M_D^0 + 1) - CDF(M_D^0 - 1)$ is given by the plusses. The different colours correspond to different evolution-times δt. (b) Evolution towards the limiting values for $a \neq b$.

outcomes after q measurements. The result is shown in Fig. 5.7. The different relaxation speeds for the two conclusive measurements is due to the different dynamics of the sectors. This is easily seen when we look at the Néel state for the initial state in the bath D, $|\psi_D\rangle = |010101\cdots\rangle$. With the initial Bell-pair on RA we get the full initial state as

$$|\Psi\rangle = \frac{1}{\sqrt{a^2 + b^2}} \left(|00\rangle \, |010101\cdots\rangle + |11\rangle \, |010101\cdots\rangle \right). \tag{5.10}$$

The dynamics of the bath-magnetization in the first part in (5.10) are slowed down because the magnetization on A is blocked from entering the bath immediately by the magnetization on the first bath-site. The limiting values of the CDF are given by (5.8) and shown as dashed horizontal lines in Fig. 5.7. This blocking is also visible at early times in 5.8, where $P_0^{n=1}(t_1)$ rises delayed in comparison to $P_1^{n=1}(t_1)$. Despite the initial bath state being the Néel state $|0101010101\rangle$, the ballistic behaviour of the dynamics is visible through the projective measurements for $\Delta = 0$. Depending on the free evolution time before the first projective measurement, the probabilities $P_{0,1}^{n=1}$ experience strong peaks at times proportional to the chain length, see 5.8(a). For strong interaction $\Delta = 1$, this sensitivity to the free evolution time between measurements is smoothened out, see 5.8(b).

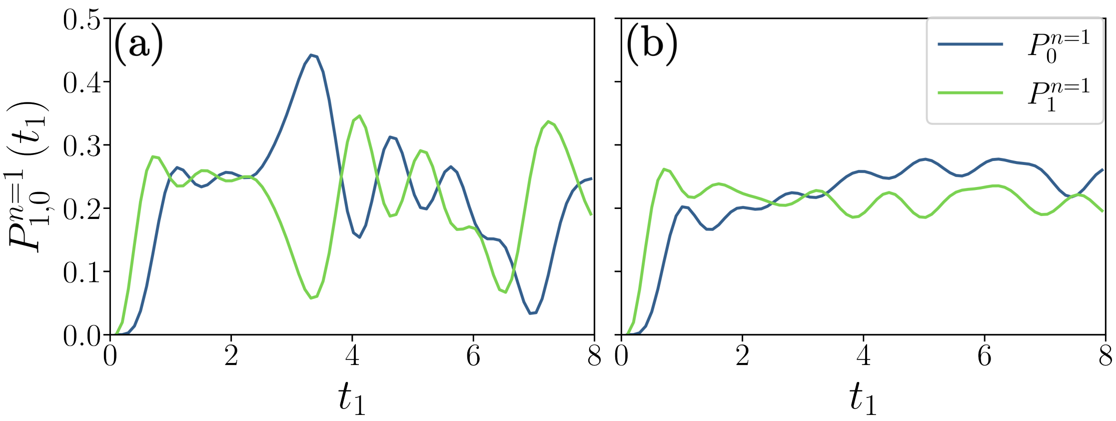

FIGURE 5.8: The ballistic dynamics on the bath can be highlighted by tuning the time δt in-between measurements. The first measurement occurs at $t_1 = \delta t$. The initial state and interaction strength are the same as in Fig. 5.7. Dynamics are calculated via exact diagonalization. (a) For $\Delta = 0$, the ballistics of the bath-dynamics are visible by the fluctuations in the projection probabilities at the first measurement. Clear peaks (dips) in probability are visible at select t_1. (b) $\Delta = 1$. The peaks (dips) visible in (a) are absent and the early stages of the projective measurement sequence are less dependent on the free evolution time between measurements.

5.4 Teleportation

The teleportation protocol outlined in section 5.2 and sketched in Fig. 5.5 is used to follow up the dynamics with which we successfully delocalize the information from A into the bath D, see Fig. 5.4. The mutual information $I(R; d)$ allows us to keep track of the information within the bath as seen in Fig. 5.4, where the interaction strength again disperses the wave-packet.

5.5 Conclusion

Local interactions in the many-body system can indeed produce scaling in the absence time that is superlinear. This works even though the XXZ chain is not chaotic and transport itself is ballistic. For system sizes in which the numerical exact diagonalization is feasible, the timescales of the first recurrence is so large that it is virtually inattainable and lies far beyond the coherence time of current experimentally available setups. This is not to say that for these sizes the finite size effects of the bath only come into effect at these times, but rather that these finite size effects only conspire to a significant amount of information relocalization at these times. This strong scaling has only been observed for global quenches, where the bath initial state is not an eigenstate of the bath. That this is connected to the linear scaling of the effective dimension in this case is contradicted by the superlinear absence time scaling in the single-particle regime.

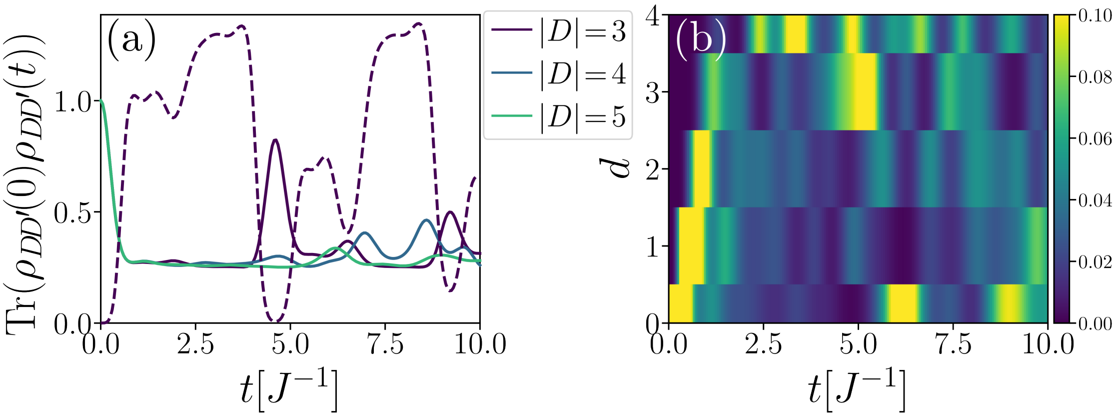

FIGURE 5.9: Dynamics in the setup for the teleportation protocol for strong interaction $\Delta = 1$. The bath initial state on DD' is given by (5.6). Reduced on D, this gives the infinite temperature state $\rho_D = \frac{1}{2^D}\mathbf{1}$. (a) Fidelity of the state on DD', $\rho_{DD'}(t)$, with its initial state (5.6), calculated as $\mathrm{Tr}\left(\rho_{DD'}(t)\, \rho_{DD'}(0)\right)$. For different bath-sizes this fidelity is typically at its minimum value $\frac{1}{4}$, the dimension of the Hilbert-space of RA. The mutual information $I(R; R')$ directly depends on this fidelity and is maximal if the fidelity is minimal, i.e. if the baths have maximally strayed from their initial state. For $|D| = 3$, $I(R; R')$ is shown by a dashed line. (b) The dynamics of the mutual information $I(R; d)$ for $d \in \{1, 2, 3, 4, 5\}$. On this bath-size, the interaction does not spread the information effectively on the ballistic timescale. Larger dimensions are difficult to investigate due to the presence of the copy of the system.

5.6 Outlook

In order to sharpen the heuristics we were able to present in both the single-particle and the many-body regime, it should prove useful to investigate local quenches in many-body systems. Since the scaling of the effective dimension is not equivalent to the scaling of the absence time scaling, this avenue enables more complicated setups with a softer but still nonlinear Hilbert-space dimension scaling with system size. For initial states such as the Néel state, the proper scaling of the absence time cannot be deduced by exact numerical methods, which are necessary if the absence time scales superlinearly. The chaotic setup of the disordered single-particle case can be extended to the many-body system in a deterministic fashion. For the XXZ chain, this is as simple as introducing a single on-site σ_z operator on a single site that is not at the boundary [118]. This is especially interesting, as the spectral impact of this seems promising, whilst the spatial impact might introduce partial reflections and undo the scaling completely. Local quenches also introduce the possibility for considering statistics such as in the single-particle case.

Solange uns eine absolute Wahrheit nicht zugänglich ist, müssen wir uns damit begnügen, daß die relativen Wahrheiten einander korrigieren.

Viktor Frankl

6

Information spreading with long-range coupling models

Information spreading in quantum systems is confined to causal regions. As opposed to classical physics, where this structure emerges from Lorentz-covariance in special relativity, this causal structure can be derived without relativity and gives rise to Lieb-Robinson bounds [119]. These bounds are related to the specifics of the quantum system at hand as well as the precise dynamics this system undergoes [87, 120–122]. The search for ever-increasing Lieb-Robinson velocities has eventually merged it with the question of information scrambling in quantum systems [40, 48, 52, 86, 123, 124]. Long-range interactions have provided a great platform for investing information scrambling. In order to harness the benefits of scrambling experimentally and computationally, the structure of long-range systems would optimally be simple. The many interactions of long-range interacting systems make this difficult, but there are alternatives to dense coupling that have been explored in recent years [1, 40, 86, 123].

In this chapter we use the theory outlined and developed in chapter 3 to investigate quench-dynamics between translationally invariant quadratic Fermion models. The models being quadratic enables the diagonalization via a Bogoliubov-Valatin transformation, as shown in section 3.4. Translational invariance makes this transformation factorize into a Fourier-transformation and a block-wise unitary transformation (for fermions). Quench-dynamics restrict the dynamics to the subspace of fermionic gaussian states (FGS). These three simplifications conspire to give us a great analytical handle over the physics of this model, which translates to computational gain in simulations. In section 6.1 we formulate the Hamiltonian with which the different setups, dense and sparse long-range coupling models, are described. In section 6.2, we establish the ring model which is the local $\alpha \to \infty$ limit of the long-range models we consider. From this ring geometry quenches in the pair (α, Δ) are performed into the different geometries. Section 6.3 investigates the dense algebraic model, starting in section 6.3.1 with static properties such as the spectrum and the ground-state correlations for different special cases. These include impacts of variations in system size, whose relevance especially in the long-range regime $\alpha < \alpha^*$ becomes apparent. The rest of the section is concerned with quenches from the ring geometry into the dense algebraic model. Correlation spreading over the system and half-system entropy dynamics are considered. Thereafter the scaling of the tripartite mutual information I_3 with α after a short time is investigated in the spirit of Kuriyattil et al [1]. Section 6.4 mirrors the preceeding section, investigating the sparse long-range Power p (PWRp) models.

6.1 Setup

Our models conceptually start from the ring-geometry introduced in section 3.4.1 & 6.2, equipped with nearest-neighbour pairing $c_s^\dagger c_{s+1}^\dagger$ proportional to Δ and long-range hopping $c_s^\dagger c_r$ proportional to $J_{|s-r|}$. The Hamiltonian has the same structure as the one in (3.13), and is repeated here,

$$\begin{aligned}\mathscr{H} &= \sum_{s,r} J_{|s-r|} c_s^\dagger c_r + \Delta_{|s-r|} c_s c_r + \overline{\Delta}_{|s-r|} c_s^\dagger c_r^\dagger \\ &= \frac{1}{2} w^\dagger \begin{pmatrix} J & \overline{\Delta} \\ \Delta & -J \end{pmatrix} w + O\end{aligned} \quad . \tag{6.1}$$

We specifically confine the pairing to local interactions, $\Delta_{|s-r|} = \Delta\, \delta_{|s-r|,1}$[1], whereas the hopping $J_{|s-r|}$ is unspecified in range [81]. The local pairing Δ allows us to investigate quench dynamics between different hopping geometries by variation of Δ. In contrast to this Vodola et al. investigates the same algebraic decay for hopping and pairing terms, treating them on an equal footing [53]. The local form of pairing specifies the k-space pairing function $\mathscr{D}_k$, first seen in section 3.4.1, as

$$\mathscr{D}_k = 2\Delta \sin\left(\frac{2\pi}{N} k\right) . \tag{6.2}$$

---

[1] Here δ denotes the Kronecker delta.

As shown in section 3.6, the Kac prescription, fixing the local energy density given by the sum of all hopping-magnitudes to a constant, is required at low enough α, depending specifically on the models at hand. For consistency's sake, the Kac prescription is used throughout for all results shown (except when specified otherwise). As such, the ratio $\frac{\Delta}{J}$, hinting at the dominance of either hopping or pairing terms in the Hamiltonian, is understood as

$$\frac{\Delta}{\sum_{d=1}^{N/2} J_d\left(\alpha\right)} = \Delta. \tag{6.3}$$

This is done to keep the notion of local competition intact, as the pairing is in competition with all the hopping terms originating from a site. With the Kac prescription fixing the magnitude of the sum of hoppings to 1, Δ itself denotes regime the system is in. For the models under investigation, we will explicitly derive the criteria for the spectral gap closing for different algebraic decay exponents and show the density-density correlations for different regimes. Subsequently, we will quench into these systems from the ring-geometry using the pairing term Δ. Since in the limit $\alpha \to \infty$, the translationally invariant models introduced in 3.4.1 reduce to the ring, the quench $\Delta_0 \to \Delta$ can be understood as from the ground-state of the model with $(\Delta_0, \alpha_0 = \infty)$ to $\to (\Delta, \alpha)$.

6.2 The Ring

When considering time-evolutions of the more involved models already introduced in section 3.4.1, we consider quenches from the ring to those models. As such, we first describe the ring. The ring is defined by $J_{s-r} = J\,\delta_{|s-r|,1}$ in the Hamiltonian (6.1). The diagonalization is straightforward from the theory-section, yielding the dispersion relation

$$\epsilon_k^{\text{chain}} = 2\sqrt{\cos^2\left(\frac{2\pi k}{N}\right) + \Delta^2 \sin^2\left(\frac{2\pi k}{N}\right)}. \tag{6.4}$$

From this, the model is identified as gapped except for $\Delta = 0$. At $\Delta = 0 (\Delta \neq 0)$, the ground-state density-density correlations g_2 (3.35) decay algebraically (exponentially). Using eqs. (3.33)&(3.34), we can derive that at $\Delta = 1$ and for $d > 1$, the correlations are $\langle c_r^\dagger c_{r+d}\rangle = 0$ and $\langle c_r^\dagger c_{r+d}^\dagger\rangle = 0$, and $g_2\left(r, r+d\right) = \frac{\delta_{d,0}}{4}$. This state we use as an initial state. Whereas $\Delta \gg 1$ models a strong z-field in the associated spin-model [53, 81], bridging the gap between Fermions and spins, we use $\Delta = 1$ as every build-up of correlations can be ascribed to the post-quench model.

6.3 Dense algebraic model

The dense algebraic model is described by $J_d = d^{-\alpha}$, already introduced in (3.36). Long-range algebraic coupling naturally arises in Rydberg systems, where the coupling decay is typically of $V(d) \sim \frac{1}{d^3}$ or $V(d) \sim \frac{1}{d^6}$. With high fidelity control in cold atom systems, this exponent can be tuned further, and using spatial shuffling operations strong-couplings can be engineered. The ground-state properties of the algebraic model with long-range hopping and pairing are investigated in [53], while the dynamics with local pairing is investigated in [81]. A general review for dense coupling models is given in [83]. A sketch of the model is seen in Fig. 3.1(a). Here, we describe some results already known, such as the rarefaction of the light-cone for $0 < \alpha < 2$ and the diverging group velocity [81]. We use the Kac normalization to extend the model to $\alpha < 1$, even into $\alpha < 0$. We particularly remark on the relevance of the boundary conditions in this case, contextualizing it with results discussed in [53]. We also use dynamics to investigate the tripartite mutual information buildup, where we are specifically interested in the strongly non-local regime $-1 < \alpha < 1$.

6.3.1 Spectrum and ground-state correlations

With $J_d = d^{-\alpha}$ and using (6.2) in (3.19) we find the critical exponents α_{crit} for which the spectral gap closes. Examining (3.57), the signs introduced by $\cos(\pi d)$ alternate, resulting in the alternating harmonic series of order α. For N even and $\alpha = 0$, the sums cancel out, with the unpaired term $S_{N/2} = (-1)^{N/2}$ as a remainder. For N odd and $\alpha = 0$, the boundary term does not exist, but also $\tilde{k} = \frac{N}{2}$ does not. We investigate the point $\alpha = -1$. The cosine in (3.57) oscillates between -1 and 1, whilst the coupling strength linearly increases with distance d

$$\mathscr{J}_{N/2} = 2\left\{\sum_{d=1}^{N/2} (-1)^d d\right\} - N/2. \tag{6.5}$$

The alternating series $(-1, 2, -3, 4, \cdots)$ has partial sums $(-1, 1, -2, 2, \cdots)$, cycling through all integers, which we can write as

$$\sum_{d=1}^{N/2} (-1)^d d = \begin{cases} \frac{N}{4} & \text{if } N/2 \text{ even} \\ -\frac{N+1}{4} & \text{if } N/2 \text{ odd.} \end{cases} \tag{6.6}$$

For $N/2$ even, substituting the partial sum into (6.5) exactly cancels with the unpaired term $S_{N/2} = N/2$ and the gap closes. This result and the derivations for diverging group velocity from section 3.6 are subsumed in Fig. 6.1. The Kac normalization, normalizing

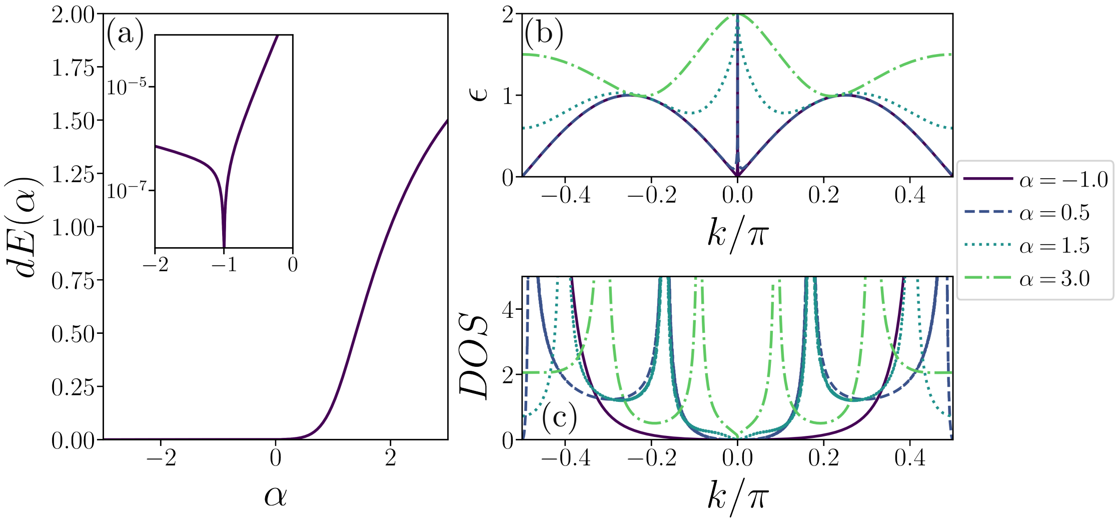

FIGURE 6.1: The dispersion-relation ϵ_k and information derived thereof for the long-range algebraic coupling on a ring of $N = 2^{12}$ sites. Kac normalization is used throughout, fixing $\mathscr{J}_0 = 2$. (a) The spectral gap for $\alpha \in [-3, 3]$ and $\Delta = 1$. As the wavenumber of the spectral gap is $k = N/2$ for all α, the value of Δ is irrelevant. The inset shows the gap fully closing at $\alpha = -1$, as derived in eqs. (6.5) and (6.6). (b) Dispersion-relation ϵ_k for different α-values at $\Delta = 0.5$. The Kac normalization prevents the divergence of ϵ_k for any α, but this does not extend to the group velocity, which can be inferred from the slope. In the local regime it is finite, diverging for $\alpha < 2$ at $k = 0$. (c) Density of states (DOS), obtained from the dispersion-relation via (3.48).

the local energy-density in the Hamiltonian, is employed throughout for these results. The closing gap at $\alpha = -1$ is shown in 6.1(a). The divergence of the group velocity for $\alpha < 2$ is visible from the slope of 6.1(b), similar to the results already observed in [81]. It might be argued that the precise dependence on even or odd N should vanish in the thermodynamic limit, and as such there is some doubt on the derivation of the critical $\alpha = -1$. However, for $\alpha < 0$ the coupling-strength $J_{N/2}$ is dominant, and by extension this is true for the unpaired term $S_{N/2}$. As such, the difference between periodic and open boundary conditions is amplified in the thermodynamic limit for $\alpha < 0$ and determined by $S_{N/2}$. Therefore, we can anticipate to implement open boundary conditions by omitting the unpaired term $S_{N/2}$. This term rebalances the contribution of the furthest coupling $J_{N/2}$ to $\mathscr{J}_k$, for which at even system-sizes exists only a single site, unlike all other distances on the ring-geometry. Stated more directly, the antipodal point to a site on a ring of even sites is unique. In contrast, all other points at a specified distance d come in pairs, either d sites clockwise or d sites anti-clockwise of the original site. Thus, omitting $S_{N/2}$ is equivalent to pretending that the site $N/2$ sites clockwise of our original site is *not* the same site as the one $N/2$ sites anti-clockwise of our original site. Implicitly, this is also done in the thermodynamic limit considered in [53], where the Fourier-transformation is given as block-diagonalizing the infinite size long-range Kitaev chain considered there.

The impact of omitting this boundary term is apparent from Fig. 6.2. In (a), the density-density correlations $g_2\,(r, r+d)$ are shown for the circular model, acknowledging the unpaired term. For slow enough algebraic decay (or rise), $-1 < \alpha < 1$, the correlations are long-range. For $\alpha < -1$, where long-range couplings are strongly dominant, the correlations with the antipodal site are dominant. Removing the unpaired term has massive results, as is seen in (b). For non-maximal distances and $\alpha > 0$, the correlations are unchanged, decaying exponentially for $\alpha > 2$ and algebraically for $\alpha < 2$ and becoming long-range for $0 < \alpha < 1$. For long-distances close to the antipodal sites(s) (as now we pretend two exist), the correlations are macroscopical for even positive $0 < \alpha < 1$. This macroscopic correlation becomes dominant and, more interestingly, correlations at intermediate distances decay exponentially. This mirrors the correlation structure associated with edge-modes, which due to the chain-like geometry do in fact exist. Edge modes of this kind were already numerically found in long-range Kitaev chains analyzed in [53]. As our analysis extends to non-decaying coupling $\alpha < 0$, the deviation from these results is relevant to point out. This highlights the care necessary when combining long-range coupling models in the non-local regime with the thermodynamic limit. As our analysis is semi-analytical, this is not due to approximations made with respect to some locality, but a feature of the changing structure of the models when varying α.

Equivalent results as in Fig. 6.2 but without the Kac normalization are shown in Fig. 6.3. This restricts the valid exponents to $\alpha > 1$ in the thermodynamic limit, but at finite size, the investigation is nonetheless insightful. Removing the Kac normalization is useful to highlight that for $\alpha > 1$, the locality of the dynamics prevail insofar as that the decay of correlations remains similar. Again however, the simple removal of the unpaired term $S_{N/2}$ has implications even for $\alpha = 1$, and moreso for slower decay. Most extreme it shows when contrasting the ring and the chain for $\alpha = -1$. Correlations remain long-ranged in the ring and are dominant at maximal distance. They fully decay in the ring and sharply peak at maximal distance.

6.3.2 Correlation spreading

Starting out from a state with local correlations, such as the one ground-state for the ring with $\Delta = 1$ described in 6.2, we quench to the long-range algebraic model with $\Delta = 0$ and varying α. We choose $\Delta = 0$ such that the correlation-spreading is due to the long-range hopping. The time-evolution of density-density correlations $g_2(r, r+d)$ of such a quench are shown for $\alpha > 0$ in Fig. 6.4. This is mostly a reiteration of results displayed in [81]. For strongly local models, 6.4(a), the lightcones for different thresholds are collapsed and form a definite “shockwave”. This shockwave is rarefied for $\alpha < 2$,

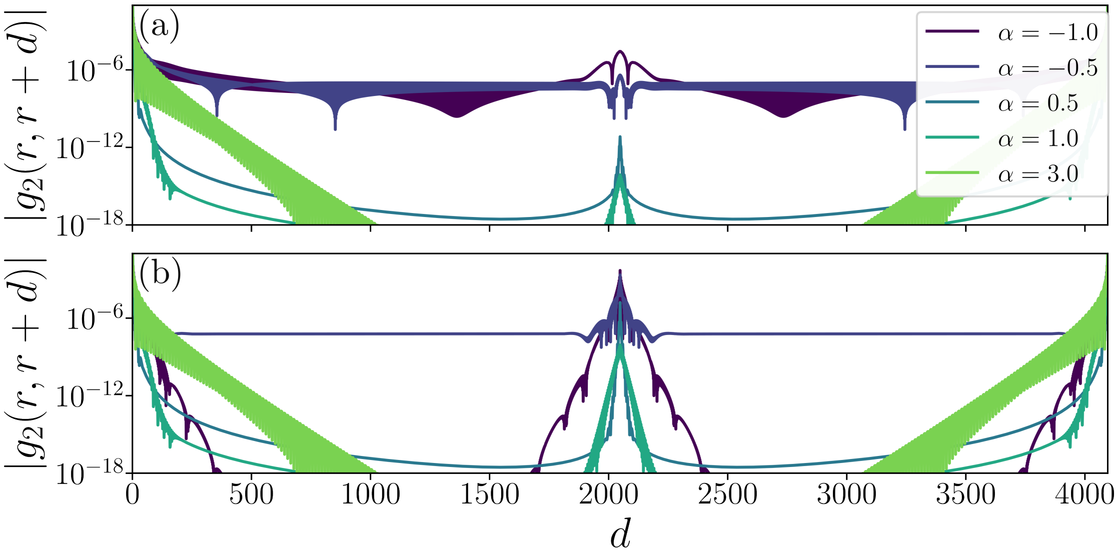

FIGURE 6.2: Correlations of the ground state of the dense long-range algebraic model, highlighted via the density-density correlations g_2. The pairing term Δ is chosen low to highlight the impact of different α, although the showed features persist for higher Δ. For $\Delta = 0$, the system is gapless and the correlations decay algebraically. The system size is $N = 2^{12}$, and the distances are $d \in [0, 2^{12}]$, such that the correlations are symmetric around $2^{11} = 2048$. (a) Using the unpaired term $S_{N/2}$, the correlations on the circle feature exponential decay in the local regime $\alpha = 3$, turning algebraic below $\alpha = 2$ and becoming constant for $\alpha < 0$. Correlations with the antipodal site become dominant below $\alpha = -1$. (b) Omitting the unpaired term $S_{N/2}$ changes the behaviour at large distances and $\alpha < 0$. Correlations with the antipodal site(s) are dominant for $\alpha < 1$, and are generally long-range for $-1 < \alpha < 0$. For $\alpha = -1$, correlations at intermediate distances decay exponentially, whilst being macroscopic for the antipodal site(s). This is akin to Majorana edge-modes in chain-like Fermionic models.

6.4(b)&(c), and weak correlations travel at much higher velocities through the system. This is consistent with the analytics found for the group velocity in section 3.6 and in Fig. 6.1. The impact of the Kac normalization becomes apparent for $\alpha < 1$, 6.4(d). In terms of correlations, the local dynamics get majorly impacted by the Kac normalization by slowing down. Light-cone rarefaction is still visible, but correlations spread through the system slower. Fitting the first occurrences of correlations of a certain strength occuring at different distances reveals that the Lieb-Robinson velocities for different thresholds $-\log_{10}(p)$ scale exponentially for $0 < \alpha < 2$ and noticeably being slower for the non-local regime $0 < \alpha < 1$.

6.3.3 Entropy dynamics

We investigate the entropy dynamics for the partition of the ring into two contiguous halves. From the $\alpha \to \infty$ connection with the Ising model via a Jordan-Wigner transformation [125], we cross-check the entropy scaling in the quench $(\alpha = \infty, \Delta = 1) \to$

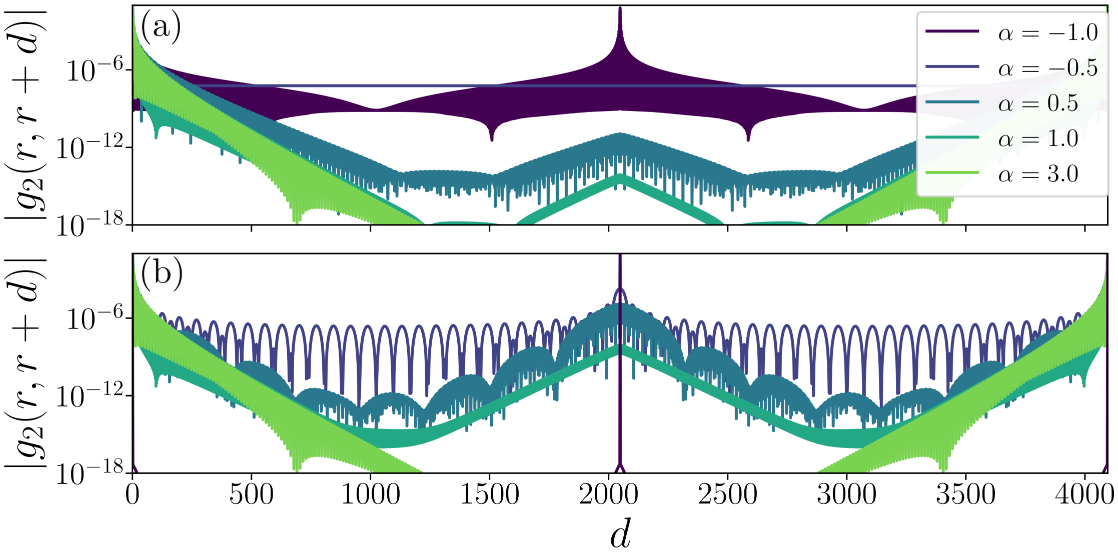

FIGURE 6.3: Results equivalent to those seen in Fig. 6.2, but without employing the Kac normalization. Correlations of the ground state of the dense long-range algebraic model, highlighted via the density-density correlations g_2. The pairing term Δ is chosen low to highlight the impact of different α, although the showed features persist for higher Δ. The system size is $N = 2^{12}$, and the distances are $d \in [0, 2^{12}]$, such that the correlations are symmetric around $2^{11} = 2048$. The analysis is similar to the one for Fig. 6.2, so here the differences are highlighted. The decay of correlations in the local regime $\alpha > 1$ has a uniform envelope, showing the preserved local structure of the model without the Kac normalization. Contrast this to Fig. 6.2, where even initial decay is vastly different for different $\alpha > 0$. The edge-mode features in the chain are massively accentuated without the Kac normalization, with correlations at intermediate distances being virtually absent.

$(\alpha = \infty, \Delta = 0)$. In Fig. 6.5(a), the half-ring entanglement entropy is shown as a function of time for rings of different sizes. The quench is $(\alpha = \infty, \Delta = 1) \to (\alpha = 3, \Delta = 0)$, so the long-range model mimicks the short-range ring. From Fig. 6.5(a), we see that the local dynamics for the half-ring entropy persist for larger rings. Rescaling both $(S_{vN}, t) \to (S_{vN}/\mu, t/\mu)$, where $\mu = N/2$ is the size of the equally large partitions of the ring, the thermodynamic limit shows the half-ring entropy scaling consistently. The initial growth of entanglement is present at different system sizes, and the saturation scales with the size $\mu = N/2$, as expected from the transverse field Ising model [126, 127]. The panels (b), (c) and (d) in Fig. 6.5 show the entropy evolution for quenches from the ring to different α for a ring of size $N = 2^7$. The evolution-time in the panels is different. Whilst for (b), the Kac normalization is fully employed and time scales with the local energy density, (c) foregoes this, and (d) scales the time with the largest coupling only. In (b) we see the lowering of α slowly changing the profile for the entropy, with strong slowing down occuring for $\alpha < 1$, where the Kac normalization becomes necessary. Without the Kac normalization, the local energy density grows fast and the dynamics for $\alpha < 1$ are accelerated, as can be seen in (c). To a lesser extent this is visible also in (d). Here we see that for large α, the dominant coupling-strength dictates

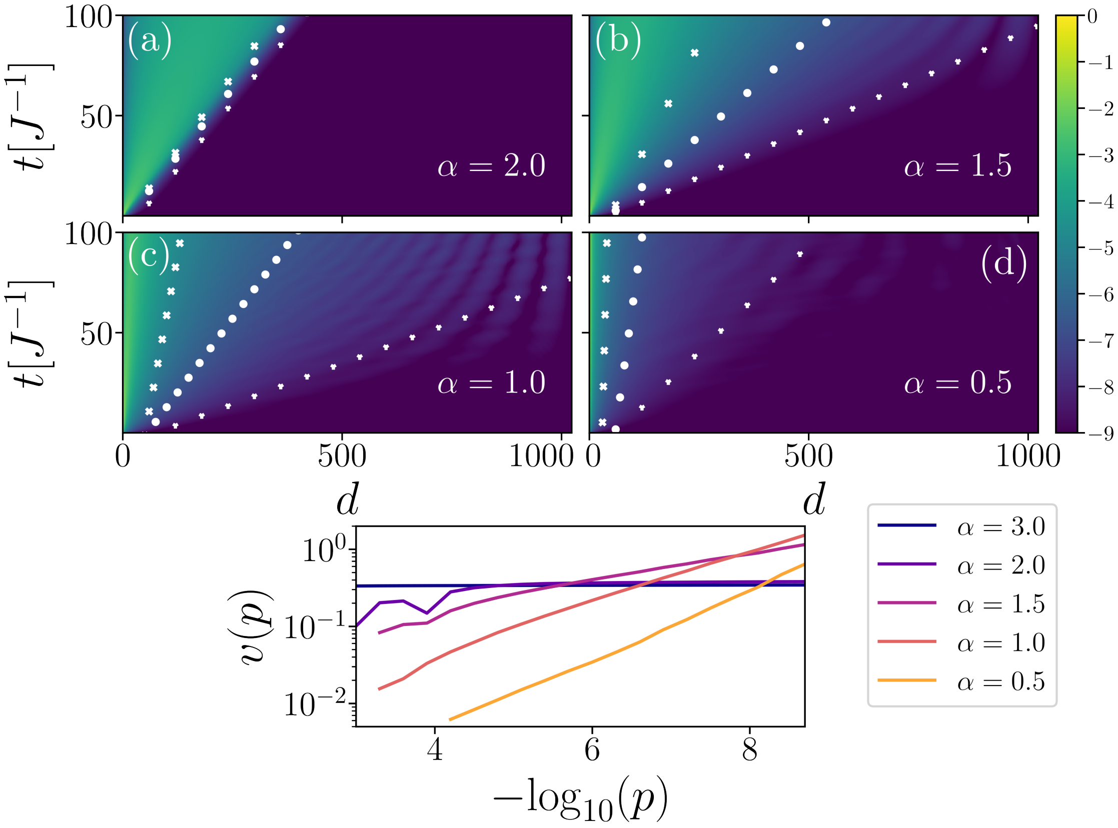

FIGURE 6.4: Time evolution of density-density correlations $\log_{10}|g_2(r, r+d)|$ shown for the ground-state quench $(\alpha_0 = \infty, \Delta_0 = 1) \rightarrow (\alpha, \Delta = 0)$. The initial state has $g_2(r, r+d) = \frac{\delta_{d,0}}{4}$. For three thresholds $\log_{10} p = [-4.8, 6.6, 8.4]$, denoted with white crosses, circles and triangles, respectively, the lightcones are shown. (a) For $\alpha = 2$ (and similarly for $\alpha > 2$), the lightcones collapse to form a definite wave-front, outside of which correlations decay exponentially. For $\alpha = 1.5$ (b), the rarefaction of the "shockwave" that is the unique lightcone is evident, and becomes stronger towards $\alpha = 1$ (c)&(d). For $\alpha < 1$, the Kac normalization slows down the local dynamics. The lightcones remain spread out for different thresholds, but overall traversal through the system is slower. Note that the Kac normalization is present for all panels, but the slowing down is only observed below $\alpha = 1$, which is the non-local regime. (e) The Lieb-Robinson velocities for different α and thresholds p are shown. For $\alpha \in \{2, 3\}$, the collapse of the lightcones is apparent since the speed is uniform for different thresholds. The rarefaction starts at $\alpha = 2$ and is most prominent for $0 < \alpha < 1$, where v_p scales exponentially in $-\log_{10} p$.

the envelope of the dynamics. For $\alpha \in \{3, 2, 1.5\}$, the entropy peaks at similar times. This behaviour vanishes around $\alpha = 1$ and is fully absent for the non-local regime. We conclude that in the thermodynamic limit the entropy dynamics slow down progressively for $\alpha < 1$.

6.3.4 Mutual Information

The slowing down of dynamics in the non-local regime is also visible from the tripartite mutual information (TMI) I_3, introduced in (3.4). However, additionally to this, the

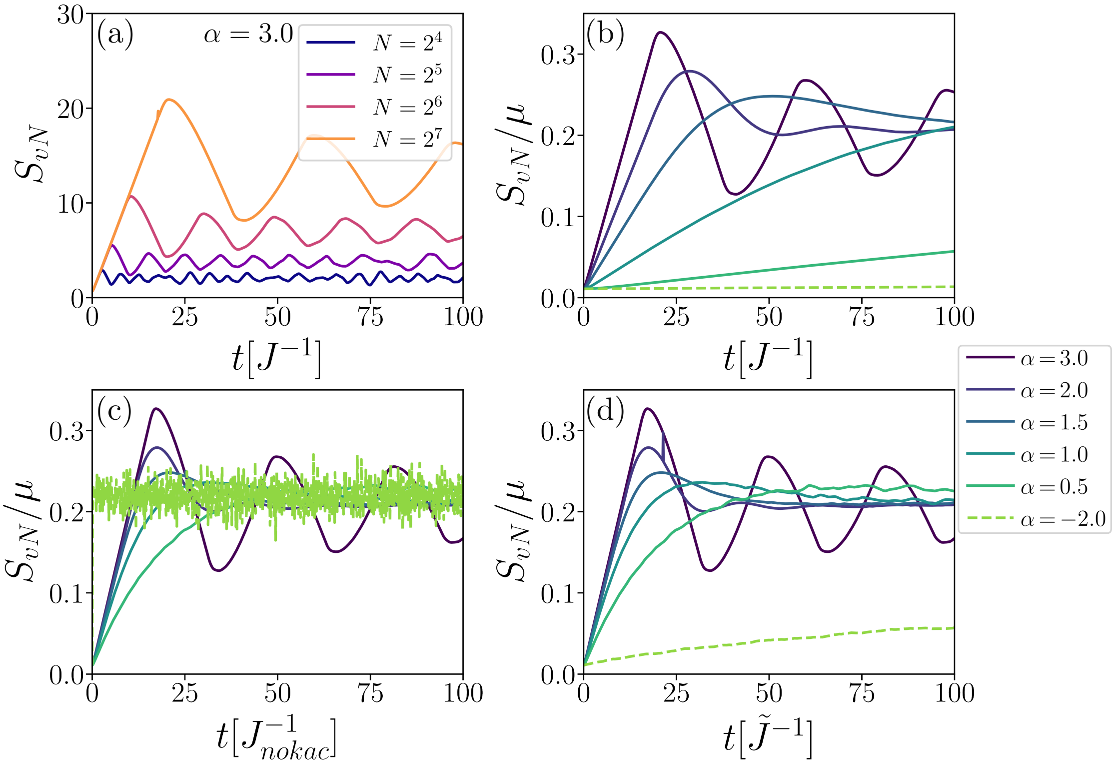

FIGURE 6.5: Entanglement entropy across a partition of the ring that cuts it in two chains of equal size μ. The quenches go from $(\alpha_0 = \infty, \Delta = 1)$ to various α and $\Delta = 0$. (a) $\alpha = 3$ and varying system sizes. The entropy dynamics follow the result known for the transverse field Ising model that is connected to the fermionic ring via a Jordan-Wigner transformation. The entropy rises linear in time to a value $\propto \mu$. (b) $\alpha \in \{3, 2, 1.5, 1, 0.5, -2\}$ and $N = 2^7$. The Kac normalization is used, and its impact becomes strong for $\alpha < 1$, slowing down the entropy dynamics. (c) similar to (b), but no Kac normalization is used. The model does not have a thermodynamic limit, and while for $\alpha > 1$ the dynamics are similar to (b), they depart strongly from it for $\alpha < 1$. (d) Different rescaling of couplings, such that the largest coupling is constant through α. The thermodynamic limit does not exist for $\alpha < 1$. For $\alpha > 1$, the local dynamics are dominated by this largest coupling, which can be seen from the entropy peaks occurring at roughly the same time.

thermodynamic limit also contributes to the slowing down, as can be seen from Fig. 6.6. The TMI is not rescaled for the different partition sizes, but the evolution-time is. For the different exponents α in the different panels of Fig. 6.6, we see the regime of area-law scaling expand in time, until the partition-size becomes important and the lines depart from one another.

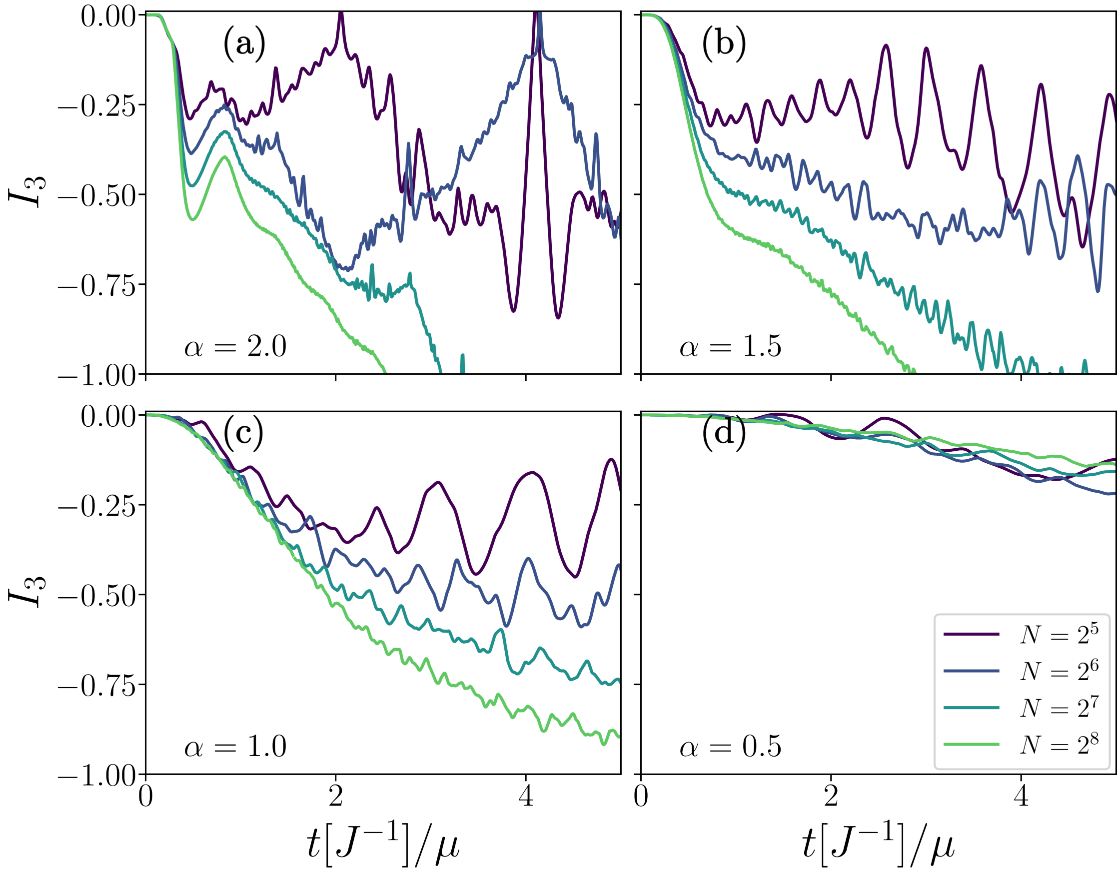

FIGURE 6.6: Tripartite mutual information (TMI) dynamics for a partition that quarters the ring. The different panels show different α and the scaling with ring-size. For different sizes N the time is rescaled differently by $\mu = N/2$. The Kac normalization is employed throughout. In rescaled time, the collapse of I_3 for early times indicates the slowing down of TMI buildup when approaching the thermodynamic limit. (a) $\alpha = 2$. Before unit time, I_3 shows no scaling with ring-size. This includes the zero-plateau and the first buildup of negative I_3. At unit time, the magnitude of I_3 starts scaling with N. (b) $\alpha = 1.5$. Similar to (a), the scaling of I_3 with N only appears at the second part of the dynamics. (c) $\alpha = 1$. Dynamics start to slow down, even in rescaled time. (d) $\alpha = 0.5$. Dynamics have slowed down markedly, consistent with the behaviour of the halfring entanglement entropy in Fig. 6.5.

6.4 Power p models

In this thesis, a Power p model (also called a PWRp model) is a model with periodic boundary conditions where sites at a distance d are coupled iff $\log_p d \in \mathbb{N}_0$. This means that connections are between sites whose distance is itself a power of p. The PWRp models are the models of consideration when looking at translationally invariant sparse coupling graphs. Examples of the PWR2 model at different system sizes are shown in Fig. 3.1(b)-(d). A big difference that has already been highlighted in [39, 40] is that, opposed to dense coupling, these models turn non-local only at $\alpha \leq 0$.

6.4.1 Spectrum and ground-state correlations

The investigation for PWRp models simplifies in comparison to the dense case. We rewrite the sum in (3.57) to be in powers of our prime base

$$\mathscr{J}_{N/2} = 2\left\{\sum_{q=0}^{Q} J_{p^q} \cos \pi p^q\right\} - S_{N/2}. \tag{6.7}$$

Using $p = 2$ is especially insightful, as for all $q \neq 0$ the cosine will be positive. Hence,

$$\begin{aligned}\mathscr{J}_{N/2} &= 2\left\{\sum_{q=1}^{Q} J_{2^q}\right\} - 2J_1 - S_{N/2} = 2\left\{\sum_{q=1}^{Q} 2^{-\alpha q}\right\} - 2 - S_{N/2},\\ &= 2\frac{2^{-\alpha} - 2^{-\alpha(Q+1)}}{1-2^{-\alpha}} - 2 - 2^{-\alpha Q},\\ &= \frac{1}{1-2^{-\alpha}}\left[2^{-\alpha+2} - 2 - 2^{-\alpha(Q+1)} - 2^{-\alpha Q}\right].\end{aligned} \tag{6.8}$$

For $\alpha > 0$, we can take the thermodynamic limit in N and Q without problems and eventually arrive at $\alpha_{crit} = 1 = \alpha^*_{\text{Hardy}}$, such that

$$\mathscr{J}_{N/2}(\alpha = 1) = 0. \tag{6.9}$$

We can also look at (6.8) and think about a functional relationship between α and Q. For the full PWR2 model, we require $Q = \log_2(N/2)$, having the boundary term $S_{N/2}$ present. For smaller Q (with N remaining large and decoupled from Q), we just get a truncated model, all the way to $Q = 1$ denoting the next-nearest neighbour model. We find the critical α_{crit} for any $1 \leq Q < \log_2(N/2)$ by imposing $\mathscr{J}_{N/2}(\alpha_{crit}) = 0$, leading to

$$2^{-\alpha(Q+1)} = 2^{-\alpha+1} - 1. \tag{6.10}$$

Q	0	1	2	∞
α_{crit}	gapped	0	$\frac{\log(1+\sqrt{5})}{\log(2)} - 1$	1

TABLE 6.1: Critical decay exponents α_{crit} at which the truncated PWR2 model is gapless. $Q = \infty$ denotes the non-truncated PWR2 model.

In table 6.1, we note some of the critical exponents for the models of different truncation order. The convergence to $\alpha_{crit} = 1$ of the full PWR2 model is very fast.

For $\alpha \to 0^+$, the unnormalized version (6.8) is not appropriate anymore. However, the use of the geometric series allows us to explicitly perform the Kac normalization, leaving us with the following formula (for $Q = \log_2(N/2)$, including the boundary term)

$$\frac{\mathscr{I}_{N/2}}{\mathscr{I}_0} = \frac{2^{-\alpha+2} - 2 - 2^{-\alpha(Q+1)} - 2^{-\alpha Q}}{2 - 2^{-\alpha(Q+1)} - 2^{-\alpha Q}}. \tag{6.11}$$

Using L'Hôpital, we can perform the limit $\alpha \to 0^+$ and obtain

$$\lim_{\alpha \to 0^+} \frac{\mathscr{I}_{N/2}}{\mathscr{I}_0} = \frac{2Q-3}{2Q+1}. \tag{6.12}$$

Thus, even in the thermodynamic limit, the PWR2 system is gapped at $\alpha = 0$. For the PWR3 model with $p = 3$, the situation is simpler. All cosine terms in (6.7) are negative, i.e.

$$\mathscr{I}_{N/2} = -2\left\{\sum_{q=0}^{Q} 3^{-\alpha q}\right\} - S_{N/2} = 2\frac{1-3^{-\alpha(Q+1)}}{3^{-\alpha}-1} - S_{N/2}. \tag{6.13}$$

We directly see that the gap of the PWR3 model never closes. This consideration holds true for all other primes, since we only required all powers to be odd (which is true for all primes except 2). As such, for any odd p, the PWRp model does not feature a closing gap.

On the other hand we can see that for even p, we can follow the PWR2 model in the derivation of α_{crit}. Specifically for p that themselves are powers of 2, we obtain α_{crit} trivially by substituting into the formulas via $p = 2^w$, arriving at $\alpha_{crit,2^w} = \alpha_{crit,2}/w$. In Fig. 6.7, the properties of the PWR2 model are investigated further. The ground-state gap is shown in 6.7(a). Above $\alpha^*_{\text{Hardy}} = 1$, for sufficiently large Δ the gap is independent of Δ and can thus only be at $k = \frac{N}{2}$. Interestingly, this is also the case for sufficiently negative α. As derived, the gap closes at $\alpha^*_{\text{Hardy}} = 1$ and does not close for $\alpha = 0$. For $\alpha < 0$, a region is present that shows erratic behaviour which scales with the magnitude of Δ, suggesting that the thermodynamic limit is not yet reached for the system size $N = 2^{19}$. Increasing the system size further dampens these fluctuations, as can be seen in Fig. 6.7(b). Around $\alpha = 0$, they decay exponentially in $\log_2(N)$, so linearly in the number of coupling terms, for $\alpha < 0$. The fluctuation region therefore seems to be

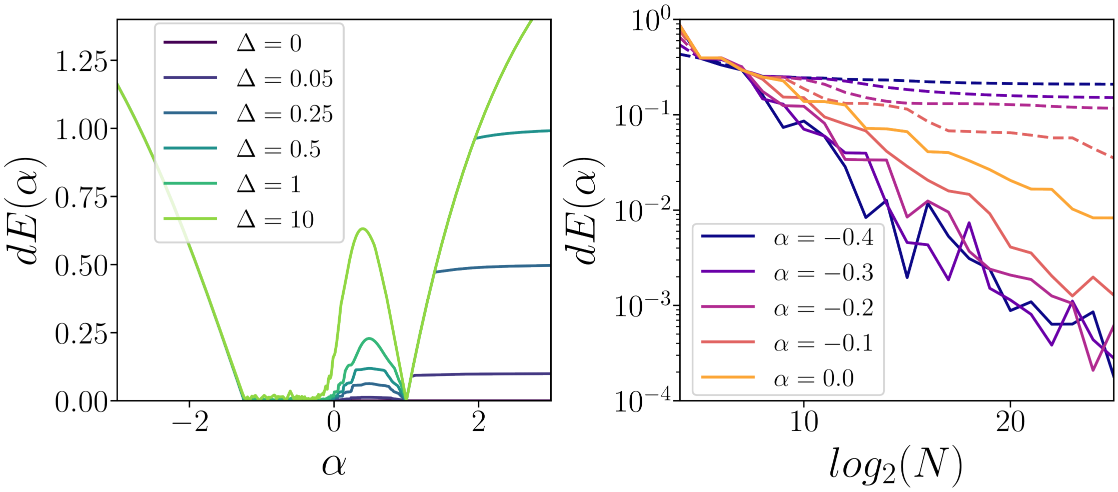

Figure 6.7: Spectral gap and coupling-function $\mathscr{J}_k$ of the PWR2 model for different parameters. (a) $N = 2^{19}$. The spectral gap closes at $\alpha = 1$ and does not close at $\alpha = 0$, which was found analytically above. The limiting regions of very positive and very negative α behave smoothly, whilst in-between the behaviour is less clear. For $0 < \alpha$ and $\alpha < -1.2$, the behaviour is well-converged in system size, whilst in-between an increase in system-size does attenuate the fluctuations of the gap. (b) Gap-scaling in the fluctuating region with system size. For every colour, dashed lines indicate $-\alpha$ for the value of the solid line. Algebraic decay in N is visible for the fluctuating region. On the other hand, the region between $\alpha = 0$ and $\alpha^*_{\text{Hardy}} = 1$ does not scale down and the model remains gapless.

gapless in the thermodynamic limit, whereas the gapped region between $\alpha = 0$ and $\alpha^*_{\text{Hardy}} = 1$ remains so.

Limits of this coupling-function are well behaved, as is shown in the remaining panels of Fig. 6.8. This presentation is chosen to facilitate the side-by-side comparison with Figure 2(b) in Bentsen et al. [40], where the same model for spins is studied. In the local regime, $\alpha = 2$ (6.8(a)), the coupling function is continuously differentiable, whereas at $\alpha = 0$ (6.8(b)) it is a Weierstrass-function. For $\alpha = -2$ (6.8(c)), the pathological behaviour has gone so far that the the function assumes values only in a few select bands, jumping between them. The second row shows the same coupling function reordered according to the Monna-mapped wavenumbers $\mathscr{M}(k)$, explained in section 3.6.2.3. For $\alpha > 0$ (6.8(d)&(e)), this transformation does not simplify anything. However, for $\alpha < 0$ (6.8(f)), the Monna map orders the coupling-function into more or less flat bands.

Here we investigate the ground-states of the PWR2 model in the limits $\alpha \to \{\infty, -\infty\}$. For the ring limit, the model is equivalent to the ring and correlations decay exponentially (algebraically) for $\Delta \neq 0 (\Delta = 0)$ in distance d. For the opposite limit, $\alpha \to -\infty$, the behaviour strongly depends on the system size. For $N = 2^p$ for any $p \in \mathbb{N}$, there is a single site at maximal coupled distance 2^{p-1}, and the model decouples into $N/2$ pairs of antipodal sites, $\{w, w + 2^{p-1}\}$. This can be seen in Fig. 3.1(c), where the light-yellow coupling connects antipodal sites. If instead we take $N = 2^p + 1$, see Fig. 3.1(d), there are

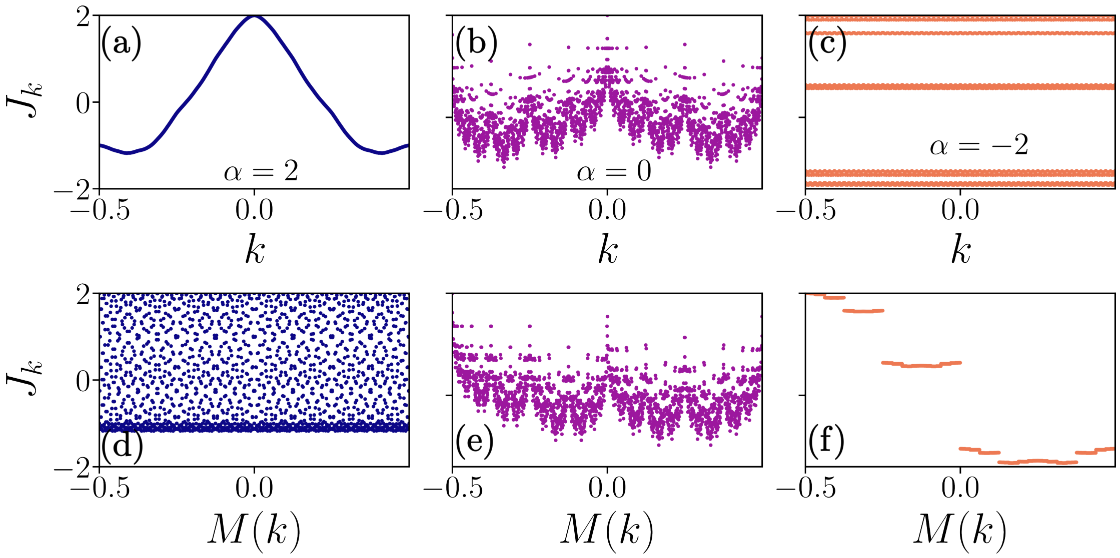

FIGURE 6.8: Locality in different geometries and crossover. (a)-(c) Coupling function for $\Delta = 0$ and $\alpha \in \{2, 0, -2\}$. At $\alpha = 0$, the Weierstrass-function is clearly visible, and for $\alpha = -2$ the oscillations are so fast that $\mathscr{J}_k$ only takes values in narrow bands. (d)-(f) The same coupling function, but arranged by Monna-mapped wavenumbers. The effect of the Monna map is opposite when comparing $\alpha = 2$ and $\alpha = -2$, the latter becoming organized by the transformation.

two sites q_1, q_2 at maximal coupled distance from site q, and they are adjacent. Thus, the sites that are ring-like adjacent to q are at maximal coupled distance to either q_1 or q_2, respectively. Following this construction along edges at maximal coupled distance, the whole graph is traversed with each site visited once. Thus, this geometry is equivalent to a ring. This construction is possible for any odd system size and boils down to the fact that multiples n of 2^{p-1} can only match a multiple q of the odd system size when $n = w \cdot q$ with $w \in \mathbb{N}$. Said differently, a closed cycle on the sparse coupling graph of size Q using only maximal coupled distances 2^{p-1} has length n if

$$\operatorname{mod}_Q\left(2^{p-1} \cdot n\right) = 0. \tag{6.14}$$

If Q is odd, the smallest n for which this is true is $n = Q$, and so the shortest closed cycle using only maximal coupled distances has size Q and thus covers the whole graph. For even system sizes that are not powers of 2, a related result can be derived. We decompose any even number N into its powers of 2 and the rest, using its unique prime factorization given by

$$N = 2^w \cdot U.$$

The relevant equation is again (6.14), and this time the smallest n for which it holds is $n = U$. For example, considering a graph of size $12 = 3 \cdot 2^2$ gives a cycle of size 3, as can be seen in Fig. 3.1(b). This example is especially interesting, as for a graph of size $3 \cdot 2^p$ with the cycle of size 3, we could expect frustration in e.g. an anti-ferromagnetic transverse-field Ising model. The stark difference in correlations this produces can be seen by comparing Figs. 6.9 and 6.10. For $\alpha = -2$ and $N = 2^{12}$ (Fig. 6.9), correlations to sites other than the singular antipodal one are strongly suppressed (with α) for $\Delta \neq 0$. More specifically, for sites at a distance d^* a power of 2, the correlations decay algebraically, whilst to other sites they decay exponentially. For $\Delta = 0$ all correlations vanish except the antipodal ones, which are macroscopic. Contrast this to $N = 2^{12} + 1$ (Fig. 6.10), where for $\alpha = -2$ and any Δ correlations decay algebraically for any distance and resemble the result for the ring. A similar distinction can be achieved for the dense algebraic coupling, even though the behaviour is not as clean for finite negative α. In the sparse model, the impact of the ring-local pairing term is intuitively seen from the other features of Figs. 6.9 and 6.10. Correlations locally peak at distances d^* which are a power of 2. Depending on the magnitude of Δ, the correlations decay differently from those distances. For large Δ, they decay slower (see 6.9(a)). At the most extreme $\Delta = 0$, correlations away from d^* instantly decay to a bulk-value (see 6.9(c) for $\alpha = 0$).

6.4.2 Correlation spreading

Starting out from a state with local correlations, such as the one ground-state for the ring with $\Delta = 1$ described in 6.2, we quench to the PWR2 model with $\Delta = 0$ and varying α. The sparse coupling leads to a very different spreading of correlations when compared to the dense model. Since the dispersion-relation is Lipschitz-continuous, even if it is not differentiable, it is not expected that Lieb-Robinson velocities speed up indefinitely. In Fig. 6.11, quenches into $\alpha \geq 0$ are shown. Even in the local regime the sparse connections inject correlations into far sites to which they are connected. At the same time, clear light-cones are visible within which correlations are strong. The biggest contrast to the dense model is the fact that the time-scales are not slowed down for strong long-range coupling, even if employing the Kac normalization. In 6.11(d), correlations are spread fast through the whole system, even if the local energy-density is the same as for different α. For $\alpha < 0$, the local structure of the model becomes apparent again by employing the Monna map. In Fig. 6.12, at $\alpha = -2$, the model is local in the dominant antipodal couplings. In the ring-geometry, correlations build up almost instantly across the sites, but stay somewhat local to those sites. However, employing the Monna map reveals that the correlations do spread ballistically in this new configuration, as seen in 6.12(b). Most notably, as seen in 6.12(a), the actual connections do not feature density-density correlations, but instead the immediate ring-like neighbours do. This is a remnant from the pre-quench initial state, for which $\Delta = 1$ and density-density correlations in neighbouring sites are suppressed. Once again contrasting odd and even ring-sizes, we see the stark differences resulting from this in Fig. 6.13. The bound-pairs

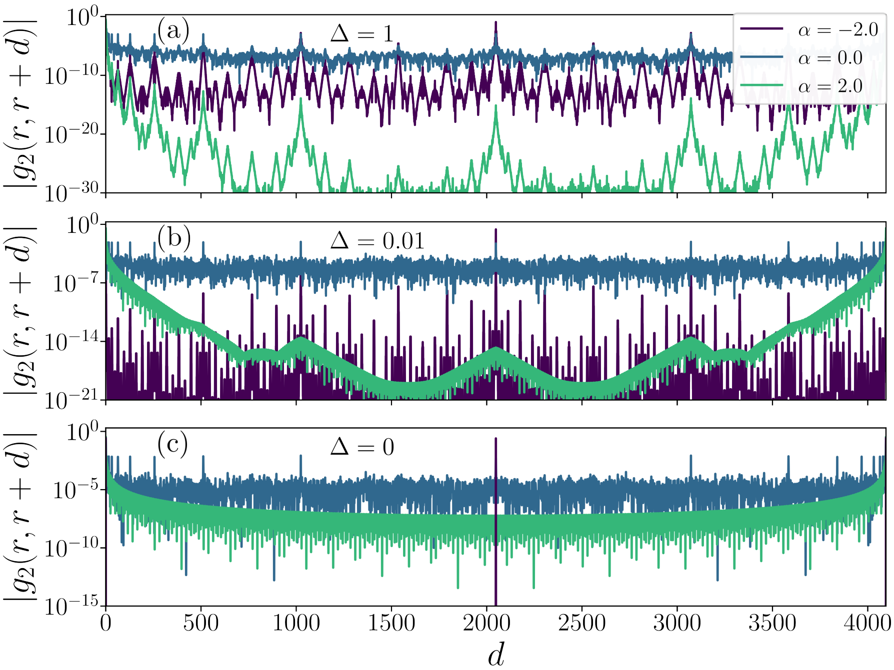

FIGURE 6.9: Correlations of the ground state of the PWR2 model, highlighted via the density-density correlations g_2. Different pairings Δ are used in different panels to show the competition between the local and the sparse geometry. In each panel, results show $\alpha \in \{2, 0, -2\}$. Note that the y-axis has different limits for the different panels. (a) $\Delta = 1$. The local peaks in correlation strengths at distances d^* of a power of 2 show local exponential decay surrounding them. The peaks are very weak for the ring-like case $\alpha = 2$. (b) $\Delta = 0.01$. In the ring-like case, the local exponential decay around the distances d^* is dominated by the global exponential decay. For $\alpha \in \{0, -2\}$, this local decay is so fast that only sharp peaks at exactly d^* appear. (c) $\Delta = 0$. The system is gapless, and the exponential decay of correlations turns algebraic. For $\alpha = -2$, correlations are absent except at $d^* = \frac{N}{2}$, peaking strongly. This general form is also what is found for the dense algebraic coupling at $\Delta = 0$. The tendency to see for decreasing Δ is that the local correlation-cones around strong peaks get successively narrower until the global behaviour dominates. For $\alpha < 0$, the global behaviour dictates correlations only between antipodal sites.

due to the singular dominant coupling in antipodal sites for $N = 2^p$ decay immediately for a single site difference, as explained before there now exists a full-graph orbit of dominant couplings. The light-cones return in ring-like fashion. The difference in light-cones between $N = 2^p \pm 1$ stems from the fact that for $N = 2^p - 1$ the number of total couplings per site is $2\,(p-1)$, the furthest and dominant being to a site of distance $d = 2^{p-2}$, while for $N = 2^p + 1$ it is $2p$, with the furthest coupling being double the distance to $d = 2^{p-1}$. For fixed α, the strongest couplings are, whilst employing the Kac normalization, different, as can be derived from (3.41). Due to this, the light-cones are different.

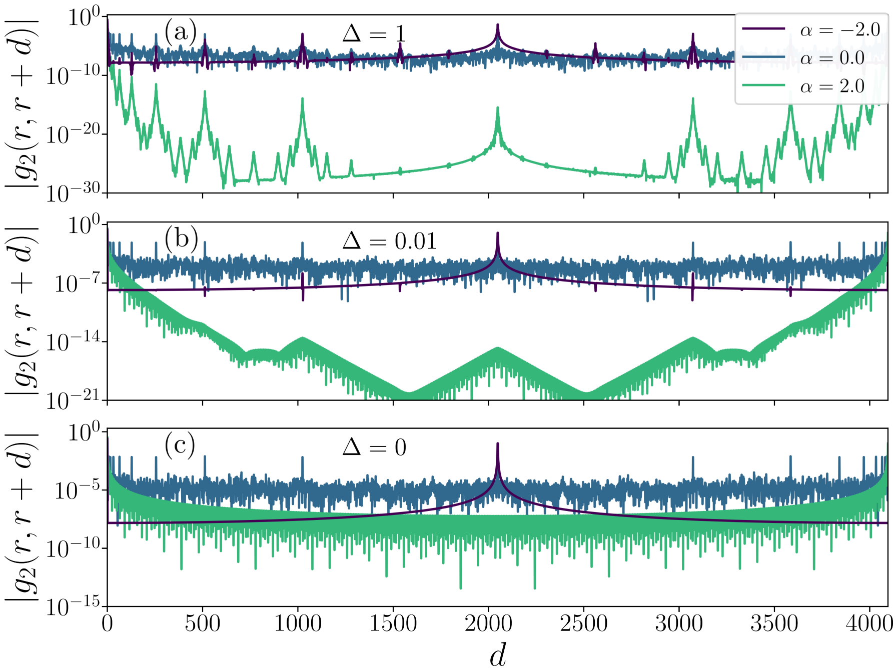

FIGURE 6.10: Density-density correlations of the ground state of the PWR2 model for odd $N = 2^{12} + 1$. The presentation mirrors that of Fig. 6.9. Short distances are completely unaffected by the addition of a single site. For large distances and $\alpha < 0$, the impact is dramatic. For odd N, the $\alpha \to \infty$ limit does not result in a graph of disconnected pairs, but in a ring. This manifests in the ground-state correlations for $\alpha = -2$, where we see not only the peak at maximal distance, but also a gradual algebraic decay away from the maximal distance.

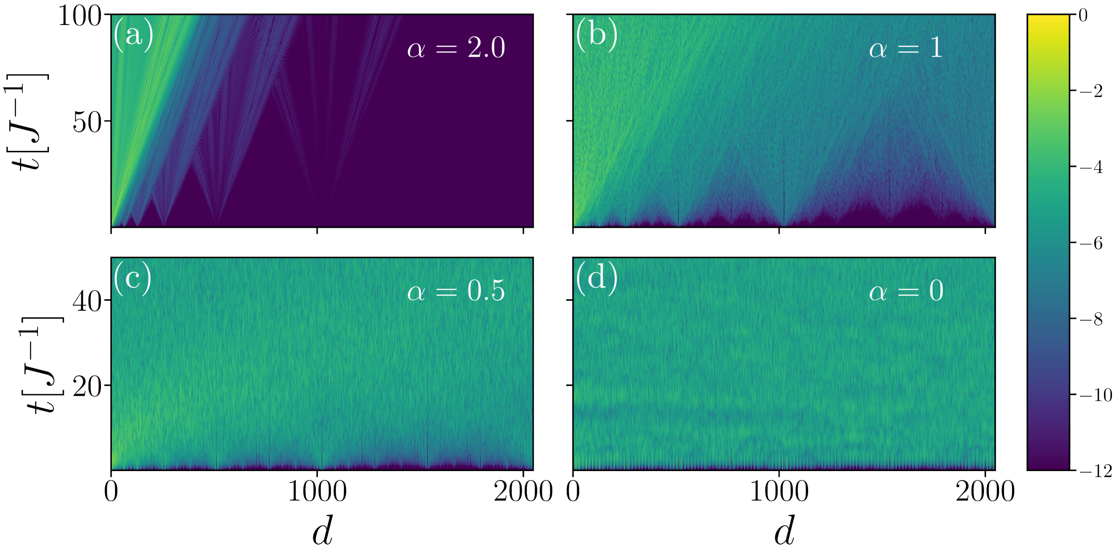

FIGURE 6.11: Density-density correlation-dynamics of quenches into the PWR2 model at different α. (a)&(b) Despite the non-trivial dynamics, there are clear light-cones visible, spreading out from different parts of the ring that are at a distance of a power of 2. This is consistent with the group velocity remaining finite. (c)&(d) Despite the group velocity not diverging, correlations cover the system extremely fast. Since the maximal graph-distance scales as $\log_2(N)$, no contradiction arises.

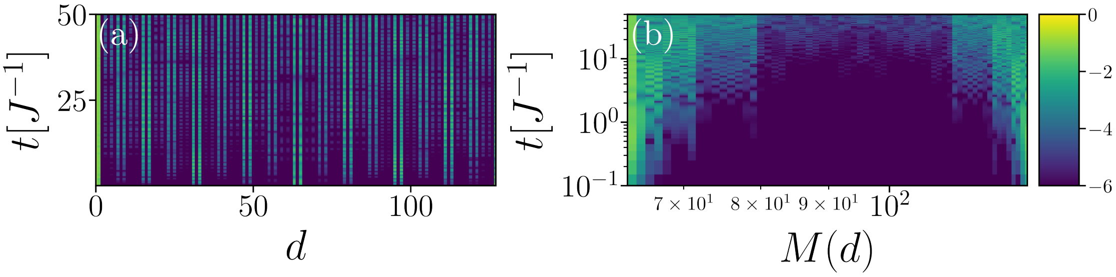

FIGURE 6.12: Correlation dynamics for a quench to $\alpha = -2$. (a) Distances are ring-like and correlations are localized around the distances of powers of 2. The actual correlations are strong on the immediate neighbours of the connected sites, which is due to the use of the density-density correlations and the initial state being the ground-state for $\Delta = 1$. (b) Using the Monna map on the distances and rearranging, we recover the light-cone structure, indicating that the model is in fact local. Instead of starting at the closest distance, the light-cone emerges from the intermediate distance $M(d) = 64$, whilst $M(d) < 64$ (not shown) are completely uncorrelated.

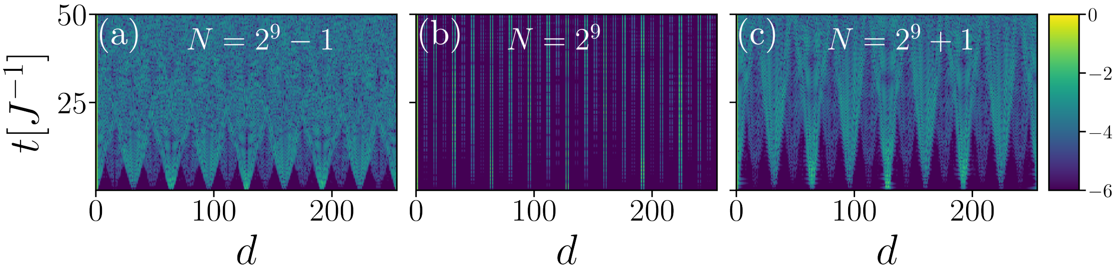

FIGURE 6.13: Correlation spreading for the quench to $\alpha = -2$ and different ring-sizes. (a)&(c) Despite being deep in the ultrametric regime, the correlations fan out in light-cones. The geometry in the ultrametric regime for odd N can be reshaped to a ring. (b) correlations stay localized to the vicinities of sites that are at distances of powers of 2. This is reformulated into a light-cone using the Monna-map, see Fig. 6.12.

6.4.3 Mutual Information

The initial state, which is the ground state of the ring at $\Delta = 1$ is not a product state in real space. Therefore, changing the partition changes the initial value of the tripartite mutual information (TMI) I_3. Different partitions such as the Monna-partition are nonetheless insightful and allow us to show the limiting behaviour at the extreme values of α. In Fig. 6.14(a)&(b), we show I_3 at particular early time-values for different α, both in the ring- and the Monna-partition (see Fig. 3.2 for the differences in these partitions). For $\alpha > 0 (< 0)$, the dynamics are suppressed in the ring-partition (Monna-partition), whereas they are nontrivial in the opposite regime. Since the same quench is shown respectively, we know the dynamics are non-trivial overall and the static behaviour is connected to the cut itself. This is also visible from Fig. 6.14(c)&(d), where the TMI dynamics are shown for select values of α. Whereas the ring-like $\alpha = 2$ shows no dynamics for the ring-partition, the same is true for the Monna-like $\alpha = -2$ for the Monna-partition. The oscillating behaviour of I_3 for $\alpha = -2$ that is seen in Fig. 6.14(a) is also visible in Fig. 6.14(c).

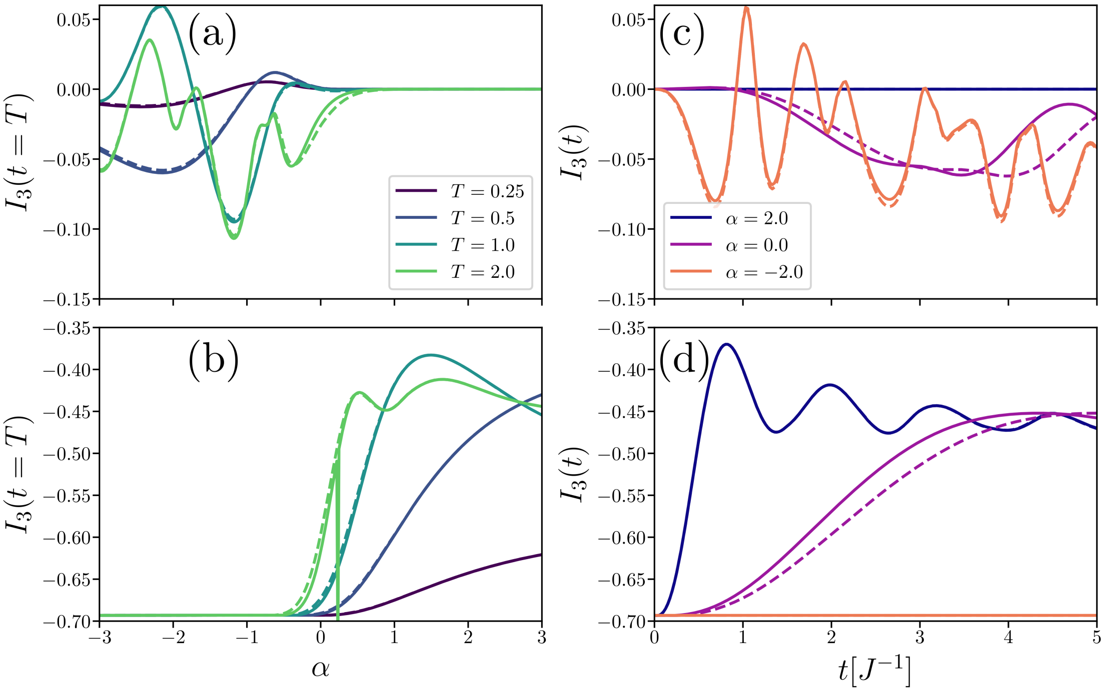

FIGURE 6.14: Tripartite mutual information for quenches from $(\alpha = \infty, \Delta = 1)$ to $\Delta = 0$, different α and different partitions. (a) The partition quarters the ring into 4 line-segments of equal size $N/4$. I_3 after fixed evolution time T is shown as a function of α and for $N = 2^8$ (solid) and $N = 2^9$ (dashed). Close to $\alpha = 0$, I_3 either directly turns negative or has a very small positive dip. For $\alpha \approx -1$, I_3 turns strongly negative. (b) Same as (a), but the partition is in Monna-mapped nearest distances. In this partition, I_3 of the initial state (the ground state of the $\Delta = 1$ chain) is strongly negative. For $\alpha < 0$, no dynamics are apparent. This mirrors the $\alpha > 0$ regime in (a). (c) Time evolution of I_3 for quenches to different α in the ring-partition. For $\alpha = -2$, the oscillation around 0 is exactly what is also observed in (a). (d) Same as (c), but the partition is in Monna-mapped nearest distances. The behaviour of $\alpha = -2$ here again mirrors $\alpha = 2$ in (c).

6.5 Conclusion

We have proven that the exponentially sparse PWR2 model's non-local nature is centered around the singular point $\alpha = 0$, around which either the euclidean or the ultrametric geometry of the Monna map localizes the model. In contrast, such a transformation is not obvious for the algebraic model and it seems like the transition from a local to a non-local model is accompanied with a freezing of the dynamics. This has been investigated recently under the name of cooperative shielding [128, 129]. The PWR2 model does not show this freezing. For $\alpha < 0$, we highlighted the impact of the system size which comes about from the dominant contributions of what otherwise would be boundary terms in euclidean local models. With this, we showed that frustration in sparse models can be engineered either by changing the sparse coupling pattern or simply by adjusting the system size. The typical system size that is in some way congruent with the coupling pattern seems to be an outlier result, even though other patterns have not been investigated as of yet.

6.6 Outlook

The sparsity patterns of PWRp coupling models we showed are only a single example of possible patterns. A pattern of considerable interest so far has been the hypercube [130]. Another possibility is the Fibonacci-like coupling that was briefly touched upon in section 3.6. One can also investigate sparse patterns that are not exponentially but algebraically sparse, such as the pattern of couplings that depend on perfect squares, mentioned at the end of section 3.6. This crucially enables to further specify the behaviour of the dense algebraic model as something that depends on the all-to-all nature or on the sparsity of the pattern. Even further, one can combine these patterns to interpolate between the dense and the sparse models by virtue of distance. Combining p-adic coupling patterns with $p = \{2, 3, 5, 6, 7\}$, makes the low-distance behaviour dense, while long-range behaviour is sparse. This might introduce length-scales on which different features dominate, which is especially interesting when considering the critical regimes when the models change their local energy density. Additionally, following one of our results, algebraically sparse couplings might possess similar nontriviality as the dense algebraic model. These could thus prove to be an interpolation point between dense and exponentially sparse coupling models, such as couplings reliant on perfect squares.

Zwischen einer Handlung und der nächsten muss der Bogenschütze sich an alles erinnern, das er getan hat, mit seinen Verbündeten sprechen, sich ausruhen und sich darüber freuen, dass er lebt.

Paulo Coelho, Der Weg des Bogens

7

Discussion and Outlook

In this thesis we have motivated and presented research revolving around the delocalization of quantum information in closed quantum systems. Chapters 2, 4 and 5 have focused on understanding the relocalization after delocalization, termed recurrence, in toy models that can be realised in AMO experiments. Starting from the intuition of ballistic transport in the single-particle setup, we have departed from the associated result of recurrence time scaling linearly with graph radius by means of a few different modifications to the model. Changing the local energy density with star-graphs and long-range coupling models, changing the coupling-strength along a model to induce slowing down of transport, and introducing disorder into the on-site energies. For these modifications, we have presented heuristics and calculations explaining the non-linear recurrence time. Via adding interaction to the model we moved to many-body physics in order to understand whether this addition can also produce superlinear recurrence time scaling, which indeed was the case. Additionally, the many-body setup introduced the possibility of measurement protocols to relocalize the information at will. This way the many-body setup guarantees very large times of delocalized information while at the same time providing a possibility of recapturing the information via a protocol. The XXZ model we explored in the many-body regime could be implemented in a cold atom setup using Rydberg arrays, where the relocalization protocols also would be applicable.

The setup of repeated local Bell pairs in the baths for the purposes of the teleportation protocol might prove problematic for larger setups due to limited coherence times.

The results from the random disordered single-particle case show that the (average) recurrence can scale exponentially both with system size and with effective dimension of the position local quantum state. However, the full random matrix theory result is not clear from our investigation, and it would be interesting to understand whether our results from a position local quantum state translate to an arbitrary quantum state, elevating the result to a statement about the Hamiltonian only. This would bridge the gap into general many-body interacting quantum systems by means of the level spacing statistics, which follow random matrix theory results.

Chapters 3 and 6 investigated the delocalization properties of long-range quadratic fermionic systems in the attempt to investigate the dynamical phase transition found in Kuriyattil et al. [1]. We presented new results for this dynamical phase transition in these models, although the results are not as decisive as in the gate-based model. A lot of understanding has been gained by analysing the sparse long-range coupling models, showing that their phase-diagram is decidedly dependent on the system size in the non-local regime. PWR3 coupling graphs in anti-ferromagnetic spin-systems are investigated to understand whether a dynamical transition takes place due to the emerging frustration in the long-range regime. The results in this thesis show that such a frustration does not innately require PWR3 coupling, but can be achieved with PWR2 coupling via minimally adjusting the system size. As next steps, it would be very interesting to understand whether the intermediate class of systems between the dense and the exponentially sparse long-range coupling systems can behave differently. Examples are the algebraically sparse long-range coupling systems such as one with couplings only on distances that are perfect squares. The exponentially sparse models feature the crossover between local and non-local behaviour only at non-decaying exponent α, whereas an algebraically sparse model shows this transition at non-trivial $\alpha^* \neq 0$.

Bibliography

[1] Sridevi Kuriyattil, Tomohiro Hashizume, Gregory Bentsen, and Andrew J. Daley. Onset of scrambling as a dynamical transition in tunable-range quantum circuits. *PRX Quantum*, 4:030325, Aug 2023. doi: 10.1103/PRXQuantum.4.030325.

[2] Henri Poincaré. Sur le problème des trois corps et les équations de la dynamique. *Acta Mathematica*, 13(1):A3–A270, 1890.

[3] Joseph Liouville. Note sur la théorie de la variation des constantes arbitraires. *Journal de mathématiques pures et appliquées*, 3:342–349, 1838.

[4] Joseph Loschmidt. *Chemische Studien*, volume 1. Gerold, 1861.

[5] Ludwig Boltzmann. On certain questions of the theory of gases. *Nature*, 51(1322), 1895. doi: 10.1038/051413b0.

[6] Josiah Willard Gibbs. *Elementary principles in statistical mechanics: developed with especial reference to the rational foundations of thermodynamics.* C. Scribner's sons, 1902. doi: 10.2307/2982426.

[7] Walther Nernst. Theorie der reaktionsgeschwindigkeit in heterogenen systemen. *Zeitschrift für physikalische Chemie*, 47(1):52–55, 1904. doi: 10.1515/zpch-1904-4704.

[8] Paul Ehrenfest and Tatiana Ehrenfest. *The conceptual foundations of the statistical approach in mechanics.* Courier Corporation, 1990.

[9] Stephen O Rice. Mathematical analysis of random noise. *The Bell System Technical Journal*, 23(3):282–332, 1944. doi: 10.1002/j.1538-7305.1945.tb00453.x.

[10] Pietro Bocchieri and Angelo Loinger. Quantum recurrence theorem. *Physical Review*, 107(2):337, 1957. doi: 10.1103/PhysRev.107.337.

[11] P Chr Hemmer, LC Maximon, and H Wergeland. Recurrence time of a dynamical system. *Physical Review*, 111(3):689, 1958. doi: 10.3934/dcds.2011.30.1.

[12] M Kac. Remark on recurrence times. *Physical Review*, 115(1):1, 1959. doi: 10.1103/PhysRev.115.1.

[13] Marko Žnidarič, Tomaž Prosen, and Peter Prelovšek. Many-body localization in the heisenberg xxz magnet in a random field. *Physical Review B—Condensed Matter and Materials Physics*, 77(6):064426, 2008. doi: 10.1103/PhysRevB.77.064426.

[14] NC Murphy, R Wortis, and WA Atkinson. Generalized inverse participation ratio as a possible measure of localization for interacting systems. *Physical Review B—Condensed Matter and Materials Physics*, 83(18):184206, 2011. doi: 10.1103/PhysRevB.83.184206.

[15] Grégoire Misguich, Vincent Pasquier, and Jean-Marc Luck. Inverse participation ratios in the xxz spin chain. *Physical Review B*, 94(15):155110, 2016. doi: 10.1103/PhysRevB.94.155110.

[16] Antonio Štrkalj, Elmer VH Doggen, Igor V Gornyi, and Oded Zilberberg. Many-body localization in the interpolating aubry-andré-fibonacci model. *Physical Review Research*, 3(3):033257, 2021. doi: 10.1103/PhysRevResearch.3.033257.

[17] Peter W Shor. Algorithms for quantum computation: discrete logarithms and factoring. In *Proceedings 35th annual symposium on foundations of computer science*, pages 124–134. Ieee, 1994. doi: 10.1109/SFCS.1994.365700.

[18] Michael A Nielsen and Isaac L Chuang. *Quantum computation and quantum information*. Cambridge university press, 2010. doi: 10.1017/CBO9780511976667.

[19] Josh M Deutsch. Quantum statistical mechanics in a closed system. *Physical Review A*, 43(4):2046, 1991. doi: 10.1103/PhysRevA.43.2046.

[20] Heinz-Peter Breuer and Francesco Petruccione. *The theory of open quantum systems*. Oxford University Press, USA, 2002. doi: 10.1093/acprof:oso/9780199213900.001.0001.

[21] Wojciech Hubert Zurek. Decoherence, einselection, and the quantum origins of the classical. *Rev. Mod. Phys.*, 75:715–775, May 2003. doi: 10.1103/RevModPhys.75.715.

[22] Sandu Popescu, Anthony J Short, and Andreas Winter. Entanglement and the foundations of statistical mechanics. *Nature Physics*, 2(11):754–758, 2006. doi: 10.1038/nphys444.

[23] Noah Linden, Sandu Popescu, Anthony J Short, and Andreas Winter. Quantum mechanical evolution towards thermal equilibrium. *Physical Review E*, 79(6): 061103, 2009. doi: 10.1103/PhysRevE.79.061103.

[24] Anthony J Short. Equilibration of quantum systems and subsystems. *New Journal of Physics*, 13(5):053009, 2011. doi: 10.1088/1367-2630/13/5/053009.

[25] Anthony J Short and Terence C Farrelly. Quantum equilibration in finite time. *New Journal of Physics*, 14(1):013063, 2012. doi: 10.1088/1367-2630/14/1/013063.

[26] Dieter Jaksch, Juan Ignacio Cirac, Peter Zoller, Steve L Rolston, Robin Côté, and Mikhail D Lukin. Fast quantum gates for neutral atoms. *Physical Review Letters*, 85(10):2208, 2000. doi: 10.1103/PhysRevLett.85.2208.

[27] C. Monroe, W. C. Campbell, L.-M. Duan, Z.-X. Gong, A. V. Gorshkov, P. W. Hess, R. Islam, K. Kim, N. M. Linke, G. Pagano, P. Richerme, C. Senko, and N. Y. Yao. Programmable quantum simulations of spin systems with trapped ions. *Rev. Mod. Phys.*, 93:025001, Apr 2021. doi: 10.1103/RevModPhys.93.025001.

[28] Andreu Riera-Campeny, Anna Sanpera, and Philipp Strasberg. Quantum systems correlated with a finite bath: Nonequilibrium dynamics and thermodynamics. *PRX Quantum*, 2:010340, Mar 2021. doi: 10.1103/PRXQuantum.2.010340.

[29] Antoine Browaeys and Thierry Lahaye. Many-body physics with individually controlled rydberg atoms. *Nature Physics*, 16(2):132–142, 2020. doi: 10.1038/s41567-019-0733-z.

[30] Christian Gross and Immanuel Bloch. Quantum simulations with ultracold atoms in optical lattices. *Science*, 357(6355):995–1001, 2017. doi: 10.1126/science.aal3837.

[31] Dolev Bluvstein, Harry Levine, Giulia Semeghini, Tout T Wang, Sepehr Ebadi, Marcin Kalinowski, Alexander Keesling, Nishad Maskara, Hannes Pichler, Markus Greiner, et al. A quantum processor based on coherent transport of entangled atom arrays. *Nature*, 604(7906):451–456, 2022. doi: 10.1038/s41586-022-04592-6.

[32] Hannes Bernien, Sylvain Schwartz, Alexander Keesling, Harry Levine, Ahmed Omran, Hannes Pichler, Soonwon Choi, Alexander S Zibrov, Manuel Endres, Markus Greiner, et al. Probing many-body dynamics on a 51-atom quantum simulator. *Nature*, 551(7682):579–584, 2017. doi: 10.1038/nature24622.

[33] Ernst Ising. *Beitrag zur theorie des ferro-und paramagnetismus.* PhD thesis, Grefe & Tiedemann Hamburg, Germany, 1924.

[34] Lars Onsager. Crystal statistics. i. a two-dimensional model with an order-disorder transition. *Physical Review*, 65(3-4):117, 1944. doi: 10.1103/PhysRev.65.117.

[35] Leo P Kadanoff. Scaling laws for ising models near t c. *Physics Physique Fizika*, 2(6):263, 1966. doi: 10.1103/PhysicsPhysiqueFizika.2.263.

[36] Markus Heyl, Anatoli Polkovnikov, and Stefan Kehrein. Dynamical quantum phase transitions in the transverse-field ising model. *Physical Review Letters*, 110(13): 135704, 2013. doi: 10.1103/PhysRevLett.110.135704.

[37] Anatoli Polkovnikov Luca D'Alessio, Yariv Kafri and Marcos Rigol. From quantum chaos and eigenstate thermalization to statistical mechanics and thermodynamics. *Advances in Physics*, 65(3):239–362, 2016. doi: 10.1080/00018732.2016.1198134.

[38] Silvia Pappalardi, Angelo Russomanno, Bojan Žunkovič, Fernando Iemini, Alessandro Silva, and Rosario Fazio. Scrambling and entanglement spreading in long-range spin chains. *Physical Review B*, 98(13):134303, 2018. doi: 10.1103/PhysRevB.98.134303.

[39] Steven S Gubser, Christian Jepsen, Ziming Ji, and Brian Trundy. Continuum limits of sparse coupling patterns. *Physical Review D*, 98(4):045009, 2018. doi: 10.1103/PhysRevD.98.045009.

[40] Gregory Bentsen, Tomohiro Hashizume, Anton S Buyskikh, Emily J Davis, Andrew J Daley, Steven S Gubser, and Monika Schleier-Smith. Treelike interactions and fast scrambling with cold atoms. *Physical Review Letters*, 123(13):130601, 2019. doi: 10.1103/PhysRevLett.123.130601.

[41] Shenglong Xu, Leonard Susskind, Yuan Su, and Brian Swingle. A sparse model of quantum holography. *arXiv preprint arXiv:2008.02303*, 2020.

[42] Tomaž Prosen, Thomas H Seligman, and Marko Žnidarič. Theory of quantum loschmidt echoes. *Progress of Theoretical Physics Supplement*, 150:200–228, 2003. doi: 10.1143/PTPS.150.200.

[43] Thomas Gorin, Tomaž Prosen, Thomas H Seligman, and Marko Žnidarič. Dynamics of loschmidt echoes and fidelity decay. *Physics Reports*, 435(2-5):33–156, 2006. doi: 10.1016/j.physrep.2006.09.003.

[44] Heinz-Peter Breuer, Elsi-Mari Laine, and Jyrki Piilo. Measure for the degree of non-markovian behavior of quantum processes in open systems. *Physical Review Letters*, 103(21):210401, 2009. doi: 10.1103/PhysRevLett.103.210401.

[45] Ingemar Bengtsson and Karol Życzkowski. *Geometry of quantum states: an introduction to quantum entanglement.* Cambridge university press, 2017. doi: 10.1017/CBO9780511535048.

[46] Moritz F Richter and Heinz-Peter Breuer. Phase-space measures of information flow in open systems: A quantum and classical perspective of non-markovianity. *Physical Review A*, 110(6):062401, 2024. doi: 10.1103/PhysRevA.110.062401.

[47] P Ben Dixon, Gregory A Howland, James Schneeloch, and John C Howell. Quantum mutual information capacity for high-dimensional entangled states. *Physical review letters*, 108(14):143603, 2012. doi: 10.1103/PhysRevLett.108.143603.

[48] Akram Touil and Sebastian Deffner. Quantum scrambling and the growth of mutual information. *Quantum Science and Technology*, 5(3):035005, 2020. doi: 10.1088/2058-9565/ab8ebb.

[49] Zi-Jian Zhang, Thi Ha Kyaw, Jakob S Kottmann, Matthias Degroote, and Alán Aspuru-Guzik. Mutual information-assisted adaptive variational quantum eigensolver. *Quantum Science and technology*, 6(3):035001, 2021. doi: 10.1088/2058-9565/abdca4.

[50] Nicolo Defenu, Tobias Donner, Tommaso Macrì, Guido Pagano, Stefano Ruffo, and Andrea Trombettoni. Long-range interacting quantum systems. *Reviews of Modern Physics*, 95(3):035002, 2023. doi: 10.1103/RevModPhys.95.035002.

[51] Beni Yoshida and Alexei Kitaev. Efficient decoding for the hayden-preskill protocol. *arXiv preprint arXiv:1710.03363*, 2017.

[52] Beni Yoshida and Norman Y Yao. Disentangling scrambling and decoherence via quantum teleportation. *Physical Review X*, 9(1):011006, 2019. doi: 10.1103/PhysRevX.9.011006.

[53] Davide Vodola, Luca Lepori, Elisa Ercolessi, and Guido Pupillo. Long-range ising and kitaev models: phases, correlations and edge modes. *New Journal of Physics*, 18(1):015001, 2015. doi: 10.1088/1367-2630/18/1/015001.

[54] Marco Thiel, M Carmen Romano, Jürgen Kurths, Riccardo Meucci, Enrico Allaria, and F Tito Arecchi. Influence of observational noise on the recurrence quantification analysis. *Physica D: Nonlinear Phenomena*, 171(3):138–152, 2002. doi: 10.1016/S0167-2789(02)00586-9.

[55] Eduardo G Altmann and Holger Kantz. Recurrence time analysis, long-term correlations, and extreme events. *Physical Review E*, 71(5):056106, 2005. doi: 10.1103/PhysRevE.71.056106.

[56] Charles L Webber Jr and Joseph P Zbilut. Recurrence quantification analysis of nonlinear dynamical systems. *Tutorials in contemporary nonlinear methods for the behavioral sciences*, 94(2005):26–94, 2005. doi: 10.1063/5.0006537.

[57] Norbert Marwan, M Carmen Romano, Marco Thiel, and Jürgen Kurths. Recurrence plots for the analysis of complex systems. *Physics Reports*, 438(5-6):237–329, 2007. doi: 10.1016/j.physrep.2006.11.001.

[58] EJ Ngamga, DV Senthilkumar, A Prasad, P Parmananda, Norbert Marwan, and Jürgen Kurths. Distinguishing dynamics using recurrence-time statistics. *Physical Review E—Statistical, Nonlinear, and Soft Matter Physics*, 85(2):026217, 2012. doi: 10.1103/PhysRevE.85.026217.

[59] Charles L Webber and Norbert Marwan. Recurrence quantification analysis. *Theory and best practices*, 426, 2015. doi: 10.1007/978-3-319-07155-8.

[60] Emmy Noether. Invariant variation problems. *Transport Theory and Statistical Physics*, 1(3):186–207, 1971. doi: 10.1080/00411457108231446.

[61] NS Krylov and VA Fock. About two interpretations of the uncertainty relations for the energy and time. *Zhurnal Eksperimentalnoi i Teoreticheskoi Fiziki*, 17:193, 1947.

[62] Saverio Pascazio, Hiromichi Nakazato, and Mikio Namiki. Temporal behavior of quantum systems and quantum zeno effect. *Symmetries in Science X*, pages 337–344, 1998.

[63] Francesco Cosco, Massimo Borrelli, Juan José Mendoza-Arenas, Francesco Plastina, Dieter Jaksch, and Sabrina Maniscalco. Bose-hubbard lattice as a controllable environment for open quantum systems. *Phys. Rev. A*, 97:040101, Apr 2018. doi: 10.1103/PhysRevA.97.040101.

[64] Lorenzo Campos Venuti. The recurrence time in quantum mechanics. *arXiv preprint arXiv:1509.04352*, 2015. doi: https://arxiv.org/pdf/1509.04352.

[65] Mary Beth Ruskai. Beyond strong subadditivity? improved bounds on the contraction of generalized relative entropy. *Reviews in Mathematical Physics*, 6(05a): 1147–1161, 1994. doi: 10.1142/S0129055X94000407.

[66] JB Gao. Recurrence time statistics for chaotic systems and their applications. *Physical Review Letters*, 83(16):3178, 1999. doi: 10.1103/PHYSREVLETT.83.3178.

[67] Arseni Goussev, Rodolfo A Jalabert, Horacio M Pastawski, and Diego Wisniacki. Loschmidt echo. *arXiv preprint arXiv:1206.6348*, 2012. doi: https://arxiv.org/pdf/1206.6348.

[68] EJ Torres-Herrera, Manan Vyas, and Lea F Santos. General features of the relaxation dynamics of interacting quantum systems. *New Journal of Physics*, 16(6): 063010, 2014. doi: 10.1088/1367-2630/16/6/063010.

[69] Takashi Mori, Tatsuhiko N Ikeda, Eriko Kaminishi, and Masahito Ueda. Thermalization and prethermalization in isolated quantum systems: a theoretical overview. *Journal of Physics B: Atomic, Molecular and Optical Physics*, 51(11):112001, 2018. doi: 10.1088/1361-6455/aabcdf.

[70] Don N Page. Average entropy of a subsystem. *Physical Review Letters*, 71(9): 1291, 1993. doi: 10.1103/PHYSREVLETT.72.1148.

[71] DA Lidar, A Shabani, and Robert Alicki. Conditions for strictly purity-decreasing quantum markovian dynamics. *Chemical Physics*, 322(1-2):82–86, 2006. doi: 10.1016/j.chemphys.2005.06.038.

[72] Jerzy Dajka, Bartłomiej Gardas, and Jerzy Łuczka. Relation between purity of an open qubit dynamics and its initial correlation with an environment. *International Journal of Theoretical Physics*, 52:1148–1159, 2013. doi: 10.1007/s10773-012-1430-1.

[73] Shenglong Xu and Brian Swingle. Scrambling dynamics and out-of-time-ordered correlators in quantum many-body systems. *PRX Quantum*, 5(1):010201, 2024. doi: 10.1103/PRXQuantum.5.010201.

[74] Paul M Chaikin, Tom C Lubensky, and Thomas A Witten. *Principles of condensed matter physics*, volume 10. Cambridge university press Cambridge, 1995. doi: 10.1088/0143-0807/22/2/702.

[75] Andrea Pelissetto and Ettore Vicari. Critical phenomena and renormalization-group theory. *Physics Reports*, 368(6):549–727, 2002. doi: 10.1103/RevModPhys.55.583.

[76] Martin Bordemann and Stefan Waldmann. Formal gns construction and states in deformation quantization. *Communications in Mathematical Physics*, 195:549–583, 1998. doi: 10.1007/s002200050402.

[77] Glen Evenbly and Guifré Vidal. Tensor network states and geometry. *Journal of Statistical Physics*, 145:891–918, 2011. doi: 10.1007/s10955-011-0237-4.

[78] Alessandro Campa, Thierry Dauxois, Duccio Fanelli, and Stefano Ruffo. *Physics of long-range interacting systems*. OUP Oxford, 2014. doi: 10.1093/acprof:oso/9780199581931.002.0005.

[79] Guifre Vidal, José Ignacio Latorre, Enrique Rico, and Alexei Kitaev. Entanglement in quantum critical phenomena. *Physical Review Letters*, 90(22):227902, 2003. doi: 10.1103/PhysRevLett.90.227902.

[80] Lev Vidmar and Marcos Rigol. Generalized gibbs ensemble in integrable lattice models. *Journal of Statistical Mechanics: Theory and Experiment*, 2016(6):064007, 2016. doi: 10.1088/1742-5468/2016/06/064007.

[81] Anton S Buyskikh, Maurizio Fagotti, Johannes Schachenmayer, Fabian Essler, and Andrew J Daley. Entanglement growth and correlation spreading with variable-range interactions in spin and fermionic tunneling models. *Physical Review A*, 93 (5):053620, 2016. doi: 10.1103/PhysRevA.93.053620.

[82] Brian Neyenhuis, Jiehang Zhang, Paul W Hess, Jacob Smith, Aaron C Lee, Phil Richerme, Zhe-Xuan Gong, Alexey V Gorshkov, and Christopher Monroe. Observation of prethermalization in long-range interacting spin chains. *Science Advances*, 3(8):e1700672, 2017. doi: 10.1126/sciadv.1700672.

[83] Nicolò Defenu, Alessio Lerose, and Silvia Pappalardi. Out-of-equilibrium dynamics of quantum many-body systems with long-range interactions. *Physics Reports*, 1074:1–92, 2024. doi: 10.1016/j.physrep.2024.04.005.

[84] N Henkel, R Nath, and T Pohl. Three-dimensional roton excitations and supersolid formation¡? format?¿ in rydberg-excited bose-einstein condensates. *Physical Review Letters*, 104(19):195302, 2010. doi: 10.1103/PhysRevLett.104.195302.

[85] A. G. de Oliveira, E. Diamond-Hitchcock, D. M. Walker, M. T. Wells-Pestell, G. Pelegrí, C. J. Picken, G. P. A. Malcolm, A. J. Daley, J. Bass, and J. D. Pritchard. Demonstration of weighted-graph optimization on a rydberg-atom array using local light shifts. *PRX Quantum*, 6:010301, Jan 2025. doi: 10.1103/PRXQuantum.6.010301.

[86] Tomohiro Hashizume, Gregory S Bentsen, Sebastian Weber, and Andrew J Daley. Deterministic fast scrambling with neutral atom arrays. *Physical Review Letters*, 126(20):200603, 2021. doi: 10.1103/PhysRevLett.126.200603.

[87] Minh C Tran, Andrew Y Guo, Christopher L Baldwin, Adam Ehrenberg, Alexey V Gorshkov, and Andrew Lucas. Lieb-robinson light cone for power-law interactions. *Physical Review Letters*, 127(16):160401, 2021. doi: 10.1103/PhysRevLett.127.160401.

[88] Michael Foss-Feig, Zhe-Xuan Gong, Charles W Clark, and Alexey V Gorshkov. Nearly linear light cones in long-range interacting quantum systems. *Physical Review Letters*, 114(15):157201, 2015. doi: 10.1103/PhysRevLett.114.157201.

[89] Sarang Gopalakrishnan, David A Huse, Vedika Khemani, and Romain Vasseur. Hydrodynamics of operator spreading and quasiparticle diffusion in interacting integrable systems. *Physical Review B*, 98(22):220303, 2018. doi: 10.1103/PhysRevB.98.220303.

[90] Benjamin Doyon, Sarang Gopalakrishnan, Frederik Møller, Jörg Schmiedmayer, and Romain Vasseur. Generalized hydrodynamics: a perspective. *Physical Review X*, 15(1):010501, 2025. doi: 10.1103/PhysRevX.15.010501.

[91] Subir Sachdev and Jinwu Ye. Gapless spin-fluid ground state in a random quantum heisenberg magnet. *Physical Review Letters*, 70(21):3339, 1993. doi: 10.1103/PhysRevLett.70.3339.

[92] Aaron Chew, Andrew Essin, and Jason Alicea. Approximating the sachdev-ye-kitaev model with majorana wires. *Physical Review B*, 96(12):121119, 2017. doi: 10.1103/PhysRevB.96.121119.

[93] Chenan Wei and Tigran A Sedrakyan. Optical lattice platform for the sachdev-ye-kitaev model. *Physical Review A*, 103(1):013323, 2021. doi: 10.1103/PhysRevA.103.013323.

[94] Aydin Deger and Tzu-Chieh Wei. Geometric entanglement and quantum phase transition in generalized cluster-xy models. *Quantum Information Processing*, 18: 1–41, 2019. doi: 10.1007/s11128-019-2439-7.

[95] Eytan Barouch and Barry M McCoy. Statistical mechanics of the x y model. ii. spin-correlation functions. *Physical Review A*, 3(2):786, 1971. doi: 10.1103/PhysRevA.3.786.

[96] Antonella De Pasquale and Paolo Facchi. Xy model on the circle: Diagonalization, spectrum, and forerunners of the quantum phase transition. *Physical Review A—Atomic, Molecular, and Optical Physics*, 80(3):032102, 2009. doi: 10.1103/PhysRevA.80.032102.

[97] Jacopo Surace and Luca Tagliacozzo. Fermionic gaussian states: an introduction to numerical approaches. *SciPost Physics Lecture Notes*, page 054, 2022. doi: 10.21468/SciPostPhysLectNotes.54.

[98] Ingo Peschel. Calculation of reduced density matrices from correlation functions. *Journal of Physics A: Mathematical and General*, 36(14):L205, 2003. doi: 10.1088/0305-4470/36/14/101.

[99] Ingo Peschel and Viktor Eisler. Reduced density matrices and entanglement entropy in free lattice models. *Journal of Physics A: Mathematical and Theoretical*, 42(50):504003, 2009. doi: 10.1088/1751-8113/42/50/504003.

[100] Marcello Dalmonte, Benoît Vermersch, and Peter Zoller. Quantum simulation and spectroscopy of entanglement hamiltonians. *Nature Physics*, 14(8):827–831, 2018. doi: 10.1038/s41567-018-0151-7.

[101] Pasquale Calabrese. Entanglement entropy, the reduced density matrices of free fermions, and beyond. *Journal of Physics A: Mathematical and Theoretical*, 49 (42):421001, 2016. doi: 10.1088/1751-8113/49/42/421001.

[102] Harold A Gersch and Gilbert C Knollman. Quantum cell model for bosons. *Physical Review*, 129(2):959, 1963. doi: 10.1103/PhysRevA.111.022223.

[103] Wu-Pei Su, John Robert Schrieffer, and Alan J Heeger. Solitons in polyacetylene. *Physical Review Letters*, 42(25):1698, 1979. doi: 10.1103/PhysRevLett.42.1698.

[104] Robert H Dicke. Coherence in spontaneous radiation processes. *Physical Review*, 93(1):99, 1954. doi: 10.1103/PhysRev.93.99.

[105] Edwin T Jaynes and Frederick W Cummings. Comparison of quantum and semi-classical radiation theories with application to the beam maser. *Proceedings of the IEEE*, 51(1):89–109, 1963. doi: 10.1109/PROC.1963.1664.

[106] Jonathan D Pritchard, D Maxwell, Alexandre Gauguet, Kevin J Weatherill, MPA Jones, and Charles S Adams. Cooperative atom-light interaction in a blockaded rydberg ensemble. *Physical Review Letters*, 105(19):193603, 2010. doi: 10.1103/PhysRevLett.105.193603.

[107] Charles S Adams, Jonathan D Pritchard, and James P Shaffer. Rydberg atom quantum technologies. *Journal of Physics B: Atomic, Molecular and Optical Physics*, 53(1):012002, 2019. doi: 10.1088/1361-6455/ab52ef.

[108] Anouar Moustaj, Julius Krebbekx, and Cristiane Morais Smith. Anomalous polarization in one-dimensional aperiodic insulators. *Condensed Matter*, 10(1):3, 2025. doi: 10.3390/condmat10010003.

[109] Godefroy Harold Hardy. Weierstrass's non-differentiable function. *Trans. Amer. Math. Soc*, 17(3):301–325, 1916. doi: 10.2307/1989005.

[110] Manuel Endres, Hannes Bernien, Alexander Keesling, Harry Levine, Eric R Anschuetz, Alexandre Krajenbrink, Crystal Senko, Vladan Vuletic, Markus Greiner, and Mikhail D Lukin. Atom-by-atom assembly of defect-free one-dimensional cold atom arrays. *Science*, 354(6315):1024–1027, 2016. doi: 10.1126/science.aah3752.

[111] Viv Kendon. Quantum walks on general graphs. *International Journal of Quantum Information*, 4(05):791–805, 2006. doi: 10.1142/S0219749906002195.

[112] Oliver Mülken, Volker Pernice, and Alexander Blumen. Universal behavior of quantum walks with long-range steps. *Physical Review E*, 77(2):021117, 2008. doi: 10.1103/PhysRevE.77.021117.

[113] Oliver Mülken and Alexander Blumen. Continuous-time quantum walks: Models for coherent transport on complex networks. *Physics Reports*, 502(2-3):37–87, 2011. doi: 10.1016/j.physrep.2011.01.002.

[114] Harold Scott Macdonald Coxeter. *Regular polytopes.* Courier Corporation, 1973. doi: 10.1017/S0008439500024413.

[115] Lorenzo Cevolani, Giuseppe Carleo, and Laurent Sanchez-Palencia. Spreading of correlations in exactly solvable quantum models with long-range interactions in arbitrary dimensions. *New Journal of Physics*, 18(9):093002, 2016. doi: 10.1088/1367-2630/18/9/093002.

[116] David J Luitz, François Huveneers, and Wojciech De Roeck. How a small quantum bath can thermalize long localized chains. *Physical Review Letters*, 119(15):150602, 2017. doi: 10.1103/PhysRevLett.119.150602.

[117] Patrick Hayden and John Preskill. Black holes as mirrors: quantum information in random subsystems. *Journal of High Energy Physics*, 2007(09):120, 2007.

[118] Aviva Gubin and Lea F Santos. Quantum chaos: An introduction via chains of interacting spins 1/2. *American Journal of Physics*, 80(3):246–251, 2012. doi: 10.1119/1.3671068.

[119] Elliott H Lieb and Derek W Robinson. The finite group velocity of quantum spin systems. *Communications in Mathematical Physics*, 28(3):251–257, 1972. doi: 10.1007/BF01645779.

[120] Bruno Nachtergaele and Robert Sims. Lieb-robinson bounds and the exponential clustering theorem. *Communications in Mathematical Physics*, 265:119–130, 2006. doi: 10.1007/s00220-006-1556-1.

[121] Alioscia Hamma, Fotini Markopoulou, Isabeau Prémont-Schwarz, and Simone Severini. Lieb-robinson bounds and the speed of light from topological order. *Physical Review Letters*, 102(1):017204, 2009. doi: 10.1103/PhysRevLett.102.017204.

[122] Daniel A Roberts and Brian Swingle. Lieb-robinson bound and the butterfly effect in quantum field theories. *Physical Review Letters*, 117(9):091602, 2016. doi: 10.1103/PhysRevLett.117.091602.

[123] Brian Swingle, Gregory Bentsen, Monika Schleier-Smith, and Patrick Hayden. Measuring the scrambling of quantum information. *Phys. Rev. A*, 94:040302, Oct 2016. doi: 10.1103/PhysRevA.94.040302.

[124] Bin Yan, Lukasz Cincio, and Wojciech H Zurek. Information scrambling and loschmidt echo. *Physical Review Letters*, 124(16):160603, 2020. doi: 10.1103/PhysRevLett.124.160603.

[125] Michael A Nielsen et al. The fermionic canonical commutation relations and the jordan-wigner transform. *School of Physical Sciences The University of Queensland*, 59:75, 2005.

[126] Pasquale Calabrese and John Cardy. Evolution of entanglement entropy in one-dimensional systems. *Journal of Statistical Mechanics: Theory and Experiment*, 2005(04):P04010, 2005. doi: 10.1088/1742-5468/2005/04/P04010.

[127] Maurizio Fagotti and Pasquale Calabrese. Evolution of entanglement entropy following a quantum quench: Analytic results for the xy chain in a transverse magnetic field. *Physical Review A—Atomic, Molecular, and Optical Physics*, 78 (1):010306, 2008. doi: 10.1103/PhysRevA.78.010306.

[128] Lea F Santos, Fausto Borgonovi, and Giuseppe Luca Celardo. Cooperative shielding in many-body systems with long-range interaction. *Physical Review Letters*, 116(25):250402, 2016. doi: 10.1103/PhysRevLett.116.250402.

[129] GL Celardo, R Kaiser, and Fausto Borgonovi. Shielding and localization in the presence of long-range hopping. *Physical Review B*, 94(14):144206, 2016. doi: 10.1103/PhysRevB.94.144206.

[130] Gregory S Bentsen, Andrew J Daley, and Johannes Schachenmayer. Entanglement dynamics in spin chains with structured long-range interactions. In *Entanglement in Spin Chains: From Theory to Quantum Technology Applications*, pages 285–319. Springer, 2022. doi: 10.1007/978-3-031-03998-0_11.